INAUGURAL - DISSERTATION

ZUR

ERLANGUNG DER DOKTORWÜRDE

DER

NATURWISSENSCHAFTLICH – MATHEMATISCHEN GESAMTFAKULTÄT

DER

RUPRECHT - KARLS - UNIVERSITÄT

HEIDELBERG

vorgelegt von

Dipl.-Chem. Sebastian Weber

aus Düsseldorf

Tag der mündlichen Prüfung: 25.07.2018

Manufacturing of Gold Nanoelectrode-Ensembles for Intracellular Recording on Living Cells

Referees:

Prof. Dr. Joachim P. Spatz	**Prof. Dr. Rainer Dahint**
Institut für Physikalische Chemie **Universität Heidelberg** **Max-Planck-Institut für medizinische Forschung, Heidelberg**	**Institut für Physikalische Chemie** **Universität Heidelberg**

Meinen Eltern

& Marion

Abstract

The investigation of electric phenomena occurring in biological cells is the subject of electrophysiological research. The discovery of ionic currents as the origin of membrane resting- and action-potentials led to a comprehensive understanding of various essential biological processes, e.g. trans-membrane transport, signal transduction in the nervous system and muscle contraction. Throughout the 20th century numerous experimental methods for observation of these phenomena have been developed and continuously improved. Precise measurements of intracellular potentials using current- and voltage-clamp based methods have become standard laboratory practice. Despite their huge success, these methods suffer from their invasive nature and inherent workload. Therefore, new methods have been sought, leading to the development of flat microelectrodes, allowing long-term stable electrical measurements with live cells and tissue samples. Arrays of flat electrodes have enabled multi-site and multi-cell measurements, but with the drawback of poor signal amplitude and signal-to-noise ratio. The continuous improvement of nanofabrication methods has enabled the fabrication of vertical nanowires. Such structures have been intensively studied in the past two decades, aiming at the design novel platforms with highly improved electrical properties for intracellular measurements.

In this work, fabrication methods for gold nanoelectrode-ensembles are studied in detail. Each step of the manufacturing process for the ensembles is reviewed in detail, resulting in more efficient manufacturing of electrodes with variable diameter and length as well as significantly improving the quality of the obtained samples. The manufactured structures were tested with electrochemical impedance spectroscopy and cyclic voltammetry to evaluate their performance for intracellular recording in *in-vitro* experiments with live cells.

Zusammenfassung

Die Untersuchung elektrischer Phänomene in Zusammenhang mit biologischen Zellen ist Gegenstand der Elektrophysiologie. Die Entdeckung von Ionenströmen als Ursprung von Ruhe- und Aktionspotentialen ebnete den Weg für ein umfassendes Verständnis verschiedener elementarer biologischer Prozesse wie z.B. dem Transmembrantransport, der Singnalleitung in Nervenzellen und der Muskelkontraktion. Im Laufe des 20. Jahrhunderts wurden zahlreiche experimentelle Methoden zur Aufklärung dieser Prozesse entwickelt und kontinuierlich verbessert. Die präzise Messung intrazellulärer Potentiale mit Voltage- und Current-Clamp-basierten Messmethoden hat sich als gängige Laborpraxis etabliert. Trotz ihres hohen Erfolgs besitzt diese Methode jedoch einige immanente Nachteile. Sie erfordert einen sehr hohen Arbeitsaufwand und ist durch ihre invasive Natur begrenzt in der zeitlichen Ausdehnung der Messungen. Als Alternative wurde die Messung elektrischer Signale von Zellen und Gewebeproben mit flachen Mikroelektroden entwickelt. In Arrays angeordnete Mikroelektroden erlauben langzeitstabile Messungen mit hoher zeitlicher und räumlicher Auflösung, allerdings mit dem Nachteil deutlich geringerer Signalamplituden und eines erhöhten Signal-Rausch-Verhältnisses. Die kontinuierliche Verbesserung von Methoden zur Herstellung von Nanostrukturen ermöglichte die Produktion von vertikalen, freistehenden Nanodrähten. Derartig strukturierte Oberflächen kommen aufgrund ihrer deutlich verbesserten elektrischen Eigenschaften und der Möglichkeit zur Herstellung eines intrazellulären elektrischen Kontakts als Alternative zu den bisher verwendeten flachen Mikroelektroden-Arrays in Betracht.

In dieser Arbeit werden Herstellungsmethoden für Nanoelektroden-Ensembles aus Gold im Detail untersucht. Alle erforderlichen Prozessschritte wurden einer eingehenden Untersuchung unterzogen, wodurch eine höhere Effizienz bei er Herstellung von Nanoelektroden mit variablem Durchmesser und Höhe bei deutlich gesteigerter Qualität. Diese Elektroden wurden in verschiedenen auf Ihre Eignung für die Messung von Spannungen und Strömen von lebenden Zellen untersucht.

CONTENT

1 Introduction

1.1 Scope of the Project

The transmembrane potential is omnipresent in virtually all biological cells and is of crucial importance for cell viability, transmembrane transport, conduction of nervous impulses, wound healing and many other processes. Electrophysiological measurements on acute tissue samples and single cells have become standard laboratory practice since the ionic origin of the resting- and action-potentials and the meanings of ion channels for these phenomena were discovered [1-3]. Electrophysiological research requires electrodes of adequate dimensions and electrical equipment capable of recording low amplitude signals in noisy environments at high time resolution. Therefore progress in this field was always coupled to availability and development of new technologies fulfilling these requirements.

Numerous variations of voltage-, current- and patch-clamp experiments were developed in the past two centuries, continuously pushing the boundaries of achievable accuracy in measurements and thus extending the knowledge of electric phenomena in biology. Yet there is still room for improvement, as most techniques used until today (e.g. patch-clamp) require the experimenter to monitor and conduct the measurement of each single cell, which makes these techniques time consuming and prone to error. Even fully automated patch-clamp units are somewhat limited in throughput and only allow experiments with cells in suspension. Another restriction of microelectrode-based experiments is the limitation to single cell measurement within a certain time window, as the cells viability is impaired by the sheer size of the microelectrodes used for these experiments and mixing of the cytosol with the electrolyte. Furthermore the interrogation of cellular networks, which is of special interest in current research (e.g. in neurobiology) on tissue samples investigating the behaviour of entire networks of cells is not possible with such methods [4].

Although first attempts for multisite recordings on tissue samples were already undertaken in the 1970s, these were limited by the size of the electrodes available at the time, a huge workload inherent to the approach and problems with handling the large amounts of data generated by such network recordings. With microfabrication techniques becoming available to scientific laboratories, flat microelectrodes were first introduced to cell research. Flat microelectrodes allowed for the interrogation of individual cells or even small groups and offered beneficial electrochemical properties owing to their small dimensions. In addition they could be brought to contact with cells by simple incubation of the cells on top of the electrodes dismissing the requirement of labour-intensive manufacturing of glass microelectrodes and their positioning with micromanipulators. Flat microelectrodes proved to be very useful and their application was soon extended from individual electrodes to arrays, enabling research with numerous cells (or sites within a sheet of cells or tissue) simultaneously. Ultra-microarrays eventually even allowed measurements at different sites within a single cell. While on the one hand being very successful, the use of flat electrodes is still limited in sensitivity as it can only establish extracellular contact. Although the measurement of intracellular potentials was realized by means of analytical data processing, the signal-to-noise-ratio of such systems is not ideal. To overcome such limitations the use of vertically free standing electrodes of nanometre dimensions was sought.

The emergence of nanofabrication methods for vertically free standing nanoelectrodes enabled fabrication of such three-dimensional structures for intracellular contacting of large cell numbers via spontaneous internalization of the nanoelectrodes by the cells or through

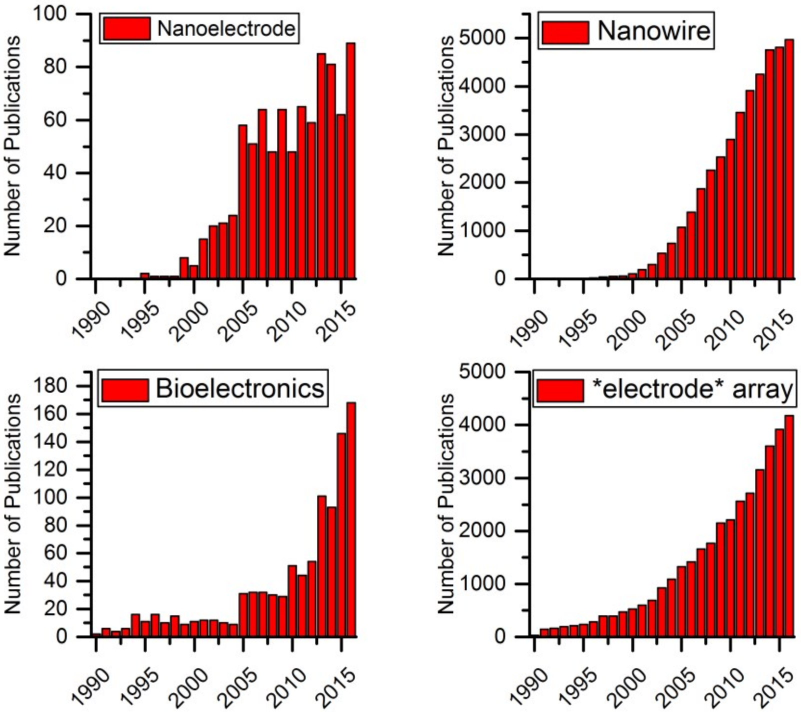

Figure 1.1 Number of publications on relevant topics Each figure displays the number of publications for the respective search phrase in the time between 1990-2016. The increasing number of citations for each search phrases illustrates the contemporary interest in research on nanoelectrodes and arrays. Results were obtained using search phrases as stated in the graphs' legends for search of the category topic in the "Web of Science Core Collection" (Sept. 2, 2017).

rupturing of the membrane with electroporation pulses [5]. Spontaneous intracellular access depends on various properties such as electrode height, diameter, density and material. As illustrated in Figure 1.1, interest in and efforts towards manufacturing of nanoelectrodes (often phrased as nanowires), arrays of micro-, ultramicro- and nanoelectrodes and in the emerging field of bioelectricity have been vastly increasing over the past 15 years. The term 'nanowire' addresses a larger field of applications than 'nanoelectrode', as it includes a wider range of materials used for non-electrical application, e.g. suspended particles [6]. Bioelectricity refers to systems which employ sophisticated materials for manipulation, measurement or energy harvesting from electric phenomena occurring in biological systems such as bacteria, cells or entire organisms. Electrode arrays or ensembles consist of numerous electrodes distributed over a surface. Spacial distribution of the electrodes over the surface can be ordered or random depending on the manufacturing process. For better understanding, a nanoelectrode array (NEA) is defined to have an organized distribution of the individual electrodes across the surface, while nanoelectrode ensembles (NEEs) show random distribution of the electrodes [7]. The phrase multielectrode array (MEA) is also commonly used. This definition has not won general recognition and many publications dealing with random ensembles actually refer to them as arrays. Yet it shall be valid throughout this text.

The aim of this work was the continued development of a functional nanoelectrode ensemble for the measurement of electrical signals of living cells *in vitro*. These efforts included optimisation of the manufacturing processes, development of novel experimental chambers for better integration of the prepared NEEs in the measurement environment and establishing processes for electrochemical characterization and electric measurements with live cells incubated on the NEEs. The concept for interfacing the NEEs with living cells is illustrated in Figure 1.2.

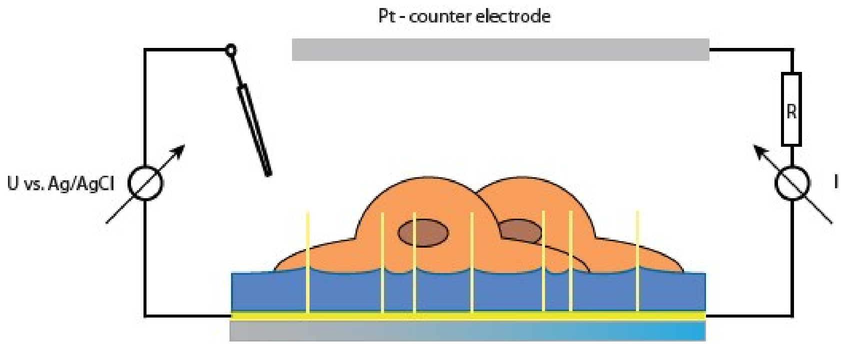

Figure 1.2 Concept for integration of the NEE surface with cells Free standing vertical nanoelectrodes protruding over the insulating polycarbonate layer establish electrical contact to the cells incubated on top. All electrodes are interconnected through the conducting gold film at the bottom which connects thr NNE is with the platinum counter-electrode and Ag/AgCl reference electrode.

1.2 Brief history of electrophysiology

First descriptions of electric phenomena in biology date back date back to ancient Egypt. Although there was no understanding for the actual concept of electricity, knowledge about electric discharges from catfish in the Nile River and rays in the Mediterranean Sea is documented in historic sources [8]. Therapeutic applications of *Torpedo torpedo* were described by SCRIBONIUS LARGUS at the time of the Roman empire (Figure 1.3 left), which used electric impulses of these fish to treat various diseases [9]. The emergence of optical microscopes in 16th century allowed scientists to examine the structure of biological tissue. ROBERT HOOKE first described the cell as building block of plant and animal tissue in 1667. In the 18th century surveys of the electric organ of fish showed their composition of stacks of cells, soon after their origin from muscle cells was discovered by JOHN HUNTER [10]. In 1776 JOHN WALSH was able to prove the electric nature of the observed phenomena by demonstrating light flashes emitted from the electric organ.

LUIGI GALVANI and ALESSANDRO VOLTA broadened this concept to muscle and nerve cells. In their experiments with frog muscles they observed contractions triggered by contact with pieces of metal (Figure 1.3) [11]. While GALVANI believed these contractions resulted from discharges of electric energy stored inside the muscle cells, VOLTA assigned this effect to a potential difference between two pieces of metal resulting in energy storage inside the tissue. His approach of constructing a model of the electric organ ultimately led to his discovery of voltaic cell in 1800 [12]. Since the first discovery of electric signals in live organisms by GALVANI in 1791, continuous efforts have been taken to understand the role of electrical signalling in physiological processes of plants and animals.

Throughout the 19th century the concept of a semipermeable membrane separating a cells interior from its environment was developed. Although cells were recognized in both plant and

Figure 1.3 Historic documents on electric phenomena in biology (left) *Torpedo torpedo* captioned in a mosaic at Pompeii (in red circle), (right) illustration by Galvani about preparation of frog-muscles for experiments. Adapted from reference [8]

animal tissue, only for plant cells the cell membrane was recognized with microscopes available at this time. The semipermeable nature of the cell membrane was first recognized by Moritz Traube, predicting permeability of the membrane for certain ions [13]. The lipid nature of the cell membrane was first proposed by Georg Hermann Quincke who observed formation of oil droplets in water and assumed a similar mechanism for the cell membrane [14].

Around 1840 Matteo Matteucci was able to show the existence of the resting membrane potential by connecting a cut nerve to a galvanometer. The first discovery of an action-potential was achieved by Emil Du Bois-Reymond, who measured the current response during an electrically induced muscle-contraction [1]. His student Julius Bernstein invented the first device allowing time-resolved measurements of fast current-transients, called the differential rheotome [15]. Bernstein later developed a theory published in 1912, of the cell membrane being permeable to potassium ions and action potentials being the result of fluctuation in this permeability [16]. Bernstein's theory was confirmed by the findings of Cole and Curtis who measured a change in resistance of the cellular membrane during an action potential [17]. The development of the voltage-clamp method by Kenneth Stewart Cole and George Marmont in 1947 allowed the measurement of electrical signals on a cellular level and marks a breakthrough in this research field [18]. Limited by the size of available electrodes at their time, they performed basic research on the electric response of giant squid axons to electrical stimuli. Based on their work, Alan Lloyd Hodgkin and Andrew Huxley developed a model that relates ionic currents in cells to electrical action potentials. The model named after the inventors was honoured with the Nobel Prize in Medicine in 1963 and remains valid until today.

Electrophysiological research with glass microelectrodes small enough to penetrate a single cells was the dominant method for almost three decades, until technical progress allowed for continuous miniaturization of electrodes and their precise positioning with micromanipulators, which led to the development of the patch-clamp method by Bert Sakmann and Erwin Neher in 1970s [19]. After their initial discovery they developed numerous variants continuously improving the concept, most importantly the “giga-seal”-method, which massively improved the signal-to-noise ratio in the performed experiments [20]. Patch-clamp experiments allowed precise measurement of currents on single ion channels within the cellular membrane and the inventors were recognized with the Nobel Prize in Medicine in 1991. Although enabling far-reaching scientific progress, until today these methods remain very time consuming and are limited to single-cell investigation, because each cell has to be located and contacted individually by the experimenter. Also the invasive nature of the experiment limits the timespan for such experiments to only a few hours. This deficit is nowadays compensated by the use of micro- and nanostructures in electrophysiological research.

1.3 Flat Microelectrodes and 3D-Nanostructures for Electrophysiological Research

Although experiments using micro-electrodes were extremely successful, new methods were developed to overcome the limitations of cell damage resulting from perforation with micro-electrodes and mixing of the cytosol with the filling solution of the electrode, while at the same time reducing the workload. Therefore the concept of interfacing cells with flat micro-electrodes was developed. Cells are brought into contact with such electrodes by simple incubation. Depending on the electrode's dimensions, signals from entire groups of cells (or tissue samples), single cells or multiple sites within a single cell can be measured. Experiments with such systems can be performed over a time-course of up to several weeks *in vitro*, as long as cells are provided sufficient nutrition and are not subject to contamination.

The choice of materials for such platforms is governed by the planned fabrication pathway, desired electrical properties and biocompatibility. Noble Metals like gold or platinum are commonly used for these reasons, but many other materials, e.g. carbon nanotubes, have been successfully tested as well. To ensure an adequate environment for cell adhesion, the electrodes and surrounding contact area for cells are often treated with a variety of compounds facilitating the adhesion of cells, e.g. poly-L- or poly-D-lysin, fibronectin, vitronectin, laminin, collagen and others.

With photolithographic pattering methods becoming available to scientific laboratories in the 1970s, flat electrodes of micrometre-dimensions could be fabricated. Precise patterning in small dimensions allowed the development of first arrays of multiple flat electrodes. Their capability to record extracellular field potential from cells incubated on top of these electrodes was successfully demonstrated by THOMAS et al. (Figure 1.4) [21]. Numerous variations of such devices have been successfully deployed in research laboratories and are nowadays available as commercialized ready-to-use-systems by companies like 3Brain or MultiChannel Systems.

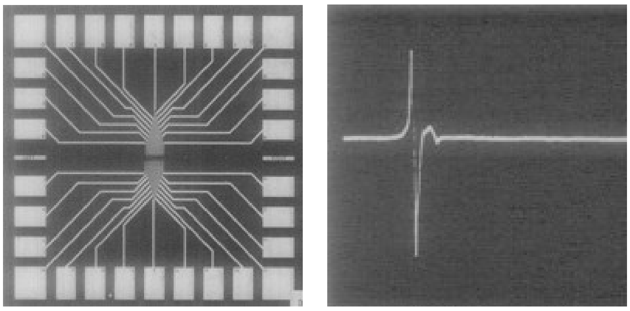

Figure 1.4 First microelectrode array developed by Thomas et al. (left) MEA with 30 electrodes; (right) biphasic action potential recorded from chicken heart cells. Adapted from reference [21]

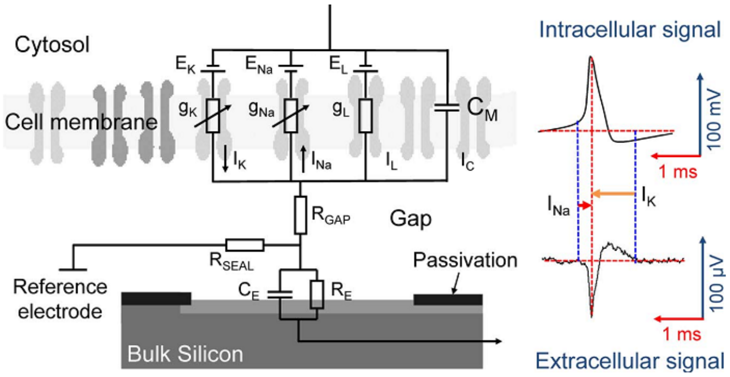

Figure 1.5 Circuit model of the interface between flat electrodes and cells (left) Extracellular field potentials are picked up by a flat electrode underneath a an adherent cell. The electrode resistance R_E and capacitance C_E together with the gap resistance R_{GAP} and seal resistance R_{SEAL} govern the shape of the recorded signal. Recorded signals are induced by ionic currents through leakage channels in the membrane altering the electrochemical potential in the cleft; (right) Comparison of intracellular recording via a patch pipette and the extracellular signal recorded at a metal pad electrode. The extracellular signal is inverted and attenuated by three orders of magnitude with considerable amount of noise resulting from the small amplitude. Adapted from reference [5].

The interface between a cell and an underlying flat electrode is schematically depicted in Figure 1.5. Between the electrode pad and the junctional membrane exists a cleft which is filled by cell culture medium. In case of HEK293-cells on a fibronectin coated silicon chip this gap is approximately 70 nm wide, resulting in a sheet resistance of approximately 10 MΩ [22]. This cleft governs the electric coupling of the cell to the electrode and limits achievable signal amplitudes detected at the electrode. This issue was addressed by FROMHERZ, who developed a field effect transistor (FET) based array with ion-specific sensitivity instead of bulk metal microelectrodes [23]. This method was soon improved by reducing electrode sizes and constructing arrays of individually addressable electrodes which added special resolution within sheets of cultured cells to the measurements. With the emergence of CMOS technology arrays of individually addressable electrodes were developed, which allowed measurements on individual cells within a sheet of cultured cells (*vide infra*) [24].

A different concept called electrical cell-substrate impedance sensing (ECIS) was introduced by GIAEVER and KEESE in the 1980s (Figure 1.6). Mammalian cells were grown on planar gold-microelectrodes while an AC-potential was applied [25-27]. Measurements were performed at a fixed frequency and changes in magnitude and phase shift allowed for the study of cellular responses to environmental changes, drugs etc. as frequency and phase shift varied. This system was not designed to measure electrical fields from cells, but to probe the barrier function of

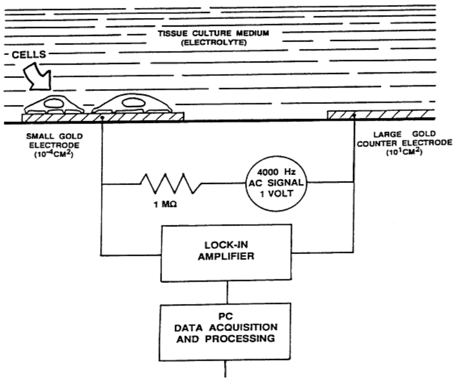

Figure 1.6 Experimental setup for ECIS by Giaver and Keese A Signal generator and lock-in amplifier are connected working- and counter electrode. Cells are incubated on the working electrode while the resulting amplitude and phase shift at the selected frequency is continuously monitored. Adapted from reference [26].

entire sheets of cells. It was successfully deployed to probe various aspects of intercellular interactions in confluent layers of cells and cell proliferation [28].

Although flat microelectrodes were successfully introduced to electrophysiological research, they suffer from a number of disadvantages inherent to the approach. Most importantly the signal-to-noise ratio is poor for two reasons: (i) flat electrodes cannot access the interior of a cell, hence the measured signal results from changes in the electric field and of ion concentrations in the cleft between call and electrode (as mentioned above) and (ii) the increasing impedance arising from miniaturization of the electrodes [24].

With the emergence of free-standing vertical nanowires, a new approach of interfacing cells

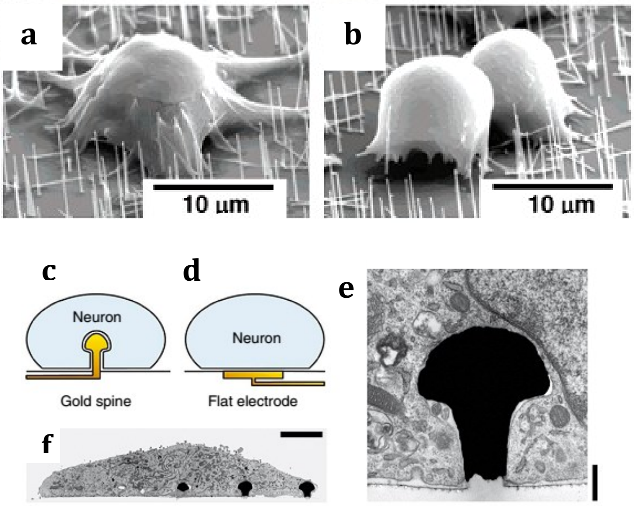

Figure 1.7 Penetration of Si-nanowires into living cells (a,b) HEK293 cells on Si-nanowires Adapted from [29]; (c,d) conparison of flat and mushroom-electrode contact to a cell; (e,f) FIB-SEM images of one and several gµEs internalized by a neuron; Adapted from [30]

with electronic circuity has been developed. Vertical nanowires of high aspect ratio with diameters between 50-400 nm and several micrometres in height were expected to spontaneously gain intracellular access by penetrating through the cellular membrane upon incubation of cells on a substrate bearing such wires. One of the first demonstrations of successful insertion of vertical silicon nanowires into HEK 293T cells was published by YANG et al. in 2005 (Figure 1.7) [29].

Another early demonstration of electrical measurements on cells was published by HAI et al. in 2009 [30-32]. The cell-electrode coupling was significantly improved by using mushroom shaped electrodes made of gold to establish cell contact. Cells would readily engulf these µGMEs thereby significantly improving the seal resistance and hence the recorded signal amplitude (Figure 1.7).

1.4 Latest developments in (CMOS-based) NEAs

The development of strategies for manufacturing and applications of vertical nanostructures for intracellular electrical recording has been subject to extensive research over the past decade. Several comprehensive reviews cover the numerous variations, that have been published on this subject in recent years [4, 6, 7, 33-40]. The recent trend in the development of nanowire-cell interfaces is the combination of functional nanowires with CMOS (Composite Metal Oxide Semiconductor) based ASICs (Application Specific Integrated Circuits). The application of CMOS technology is advantageous for several reasons:

(i) Long conduction leads for connection to external electronics are not required when each electrode (or patch of electrodes in parallel operation) is equipped with its own amplifier circuit in its very proximity. This eliminates problems of parasitic electronic effects, noise pick-up and attenuation in the leads and allows much higher numbers of electrodes in an array, which is otherwise limited by spacial requirements of the conducting leads.

(ii) On-site acquisition (or generation) of measurement and stimulation signals allows maximum flexibility with respect to experimental design and much higher sampling frequencies than could be achieved with external electronics.

(iii) Large chip numbers can be manufactured on a single wafer, making the process cost-effective and ensuring high-quality and homogeneity of the manufactured chips.

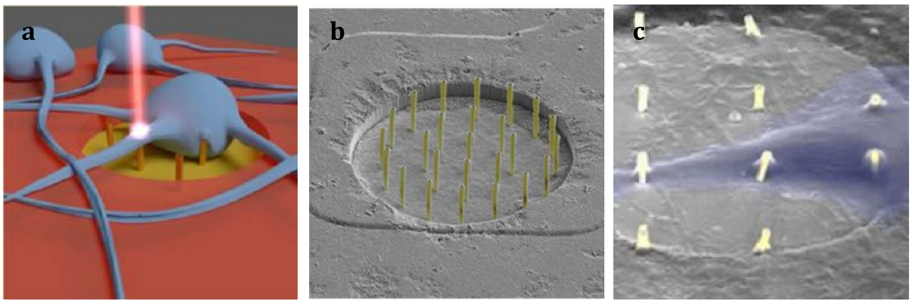

Figure 1.8 Nanoelectrode ensemble patch devolped by Dipalo et al. (a) Schematic representation of a laser beam striking the tip of an electrode; (b) electrode patch after fabrication; (c) trains of action potentials recorded after optoporation; (d) HL-1 cell sitting on top an ensemble of 12 electrodes. Adapted from [41]

CMOS based processes for the manufacturing of semiconductor electronics usually employ a sequence of material deposition and etching steps, which are performed on fully automated machines. Material is deposited by sputter coating, atomic layer deposition or spin coating in semi- or fully automated production lines. If required, the geometrical structures are defined prior to deposition using photolithography and etching techniques. The biggest disadvantage of this approach is the very high cost for the machines and time to establish the processes. Once a process is established on a manufacturing line, very high numbers of samples can be produced at rather low cost. Several research groups have recently demonstrated the capabilities of such devices.

A non CMOS-based platform was developed by Dipalo et al. featuring several parallel electrodes closely spaced on one patch (Figure 1.8) [41, 42]. The electrodes were manufactured by irradiation of an optical resist with Ga-ions in a FIB-chamber, making the irradiated resist insoluble. This allows for great flexibility in number of electrodes per patch (1-20) and pitch (2-5 µm). Electrode diameter and height were 1,8 µm at 150 nm respectively. After removal of the resist, free standing electrodes were obtained, and then a conductive layer of Ti/Au was sputtered. Key feature of this example the realization of intracellular recording by plasmonic optoporation. The cellular membrane is ruptured by mechanical waves, created from local heating as a result of near infrared laser pulses (1064 nm) focused at the electrode tips under a microscope. This method is beneficial as it allows continuous electrical recording and does not interfere with the cells inherent electrical activity like electroporation pulses. HL-1 cardiac derived cells and primary neurons were incubated on these surfaces for more than 20 DIV. Upon optoporation significant increase in signal amplitude and signal-to-noise ratio could be observed. The recorded overall signal represents a mixture of intra- and extracellular components depending on the number of optoporated electrodes and was successfully confirmed by modelling and simulation of the cell-electrode interface.

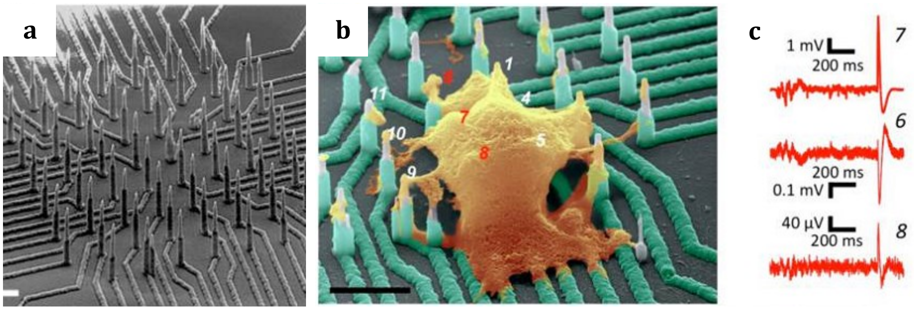

Figure 1.9 Electrode array developed by Liu et al. (left) entire array of vertical electrodes and insulated conducting leads for connection to external circuitry; (middle) human induced pluripotent stem cell incubated on the array (in false colors); (right) action potentials measured simultaneously at different electrode sites Adapted from reference [43].

Liu et al. followed an approach providing an 8 x 8 array of 60 individually addressable electrodes (one missing at each corner) with an interelectrode distance of 4 µm in the demonstrated device, which can be reduced to submicrometer scale [43]. The electrodes manufactured from a NiSi alloy and have a height of 8-10 µm and a diameter of 100-200 nm, SiO_2 was used for passivation purposes. Electrophysiological recordings from mouse and rat cortical neurons as well as human induced pluripotent stem cells wells were successfully performed for up to 14 DIV (Figure 1.9). In this example CMOS processing technologies are mostly used to provide a versatile method for manufacturing of the electrode array. It does not include on-chip read-out and data processing, but instead features conduction leads for connection to external electronics. This limitation becomes obvious by the absence of the corner electrodes in favour of conducting leads for connection of inner electrodes. Although the array provides individually addressable electrodes for simultaneous recording of several cells, their number will be limited due to spacial restrictions. Also the aspect ratio of the electrodes is rather high, therefore the cells rather sit on top of a number of electrodes than on a flat cell culture flask like surface which may influence cell viability and behaviour.

Abbott et al. have developed a chip that exploits all the above mentioned advantages of CMOS production [44]. Their chip features a 1024 pixel array allowing simultaneous recording and stimulation at a sampling rate of 9,75 kHz. The 32 x 32 electrode patches each patch consist of nine electrodes in parallel configuration for better signal-to-noise ratio. The electrodes consist of a SiO_2 core coated with 5 nm Ti and 20 nm Pt and are ~1,5 µm high and 150 nm diameter. Successful experiments measuring potential fluctuations of neonatal rat ventricular cardiomyocytes were performed, although the initial amplitude was rather weak at only 250 µV – 1,5 mV compared to ~120 mV obtained with a conventional patch pipette. After application of an electroporation pulse sequence the amplitude was raised to 5 mV with significantly decreased noise (Figure 1.10). Signal propagation throughout a sheet of cells incubated on the

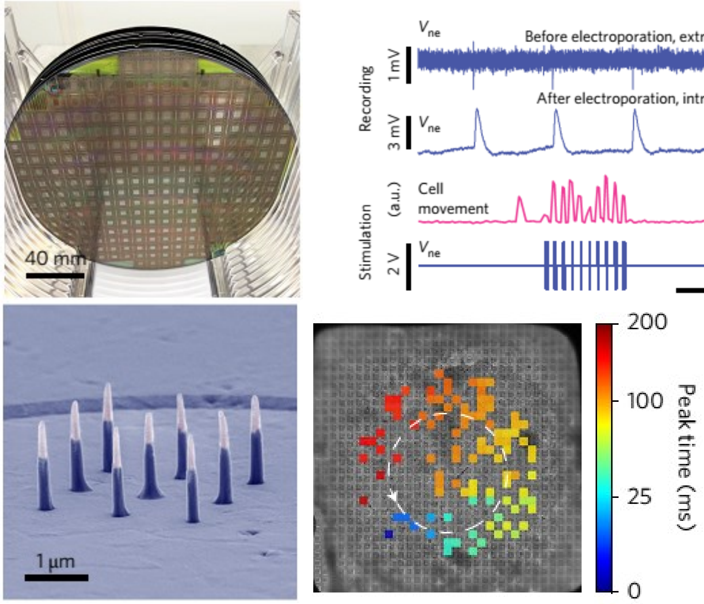

Figure 1.10 CMOS-nanowire-chip developed by Abbott et al. (top left) 8 inch wafer with 256 chips after processing; (bottom left) electrode patch of 3 x 3 electrodes in false colors: grey - uncovered Pt-electrode tips, blue - SiO2 passivation; (top right) measurement signal before and after electroporation pulses and response to stimulation; (bottom right) pixel map of the whole chip indicating circular propagation of action potentials (white arrow) measured from neonatal rat ventricular cardiomyocyte cultures incubated on the chip. Adapted from reference [44].

chip could be demonstrated and the effect of various drug on the dynamics of the observed action potentials were documented. Cells could be kept viable on the chips for experimental periods as long as 14 days, proving this chip to be a suitable platform for in vitro studies of networks of electrogenic cells.

1.5 Bioelectricity and Biosensing

Nanotechnology has paved the way for new era in biological research. Nanostructures offer unique optical, electronical and chemical properties which result from their small dimensions. Since the emergence of fabrication methods for nanoparticles (in suspension) and nanostructured surfaces, numerous applications in biological research (and other fields) have been implemented. Extensive review articles are dealing with the countless variations of manufacturing strategies, materials, functionalization and applications that have already been explored on this behalf [45, 46]. Within the context of this work, two sub-branches of nano-biotechnology are most relevant: biosensing and bioelectricity. Both fields are not entirely restricted to nanotechnology, but huge progress has been made with the emergence of nano-scale research [33, 36, 47-49].

Biofuel cells generate electricity from biochemical reactions catalysed by enzymes or microorganisms immobilized to the surface of electrodes. Electrons are shuttled from the reaction site to the electrode either directly or via a redox mediator. Realization of this electron transfer is the pinhole of the concept, often very difficult to realize and inefficient as the distance between the reaction site and the electrode is rather big, which made such cells rather inefficient in the past. The size of enzymes or organisms used for this purpose governs the minimum achievable distance from the reaction site to the electrode and the density of reaction sites per surface area, therefore the efficiency of electron transfer and achievable current densities are limited [50]. Given these limitations, the term biofuel cell can be somewhat intriguing, as such systems do not provide a suitable alternative for green energy production on a large scale. Nanotechnology allowed improvements of this aspect and enabled development of successful examples for such devices. Biofuel cells can be used *in vitro* for study purposes or in

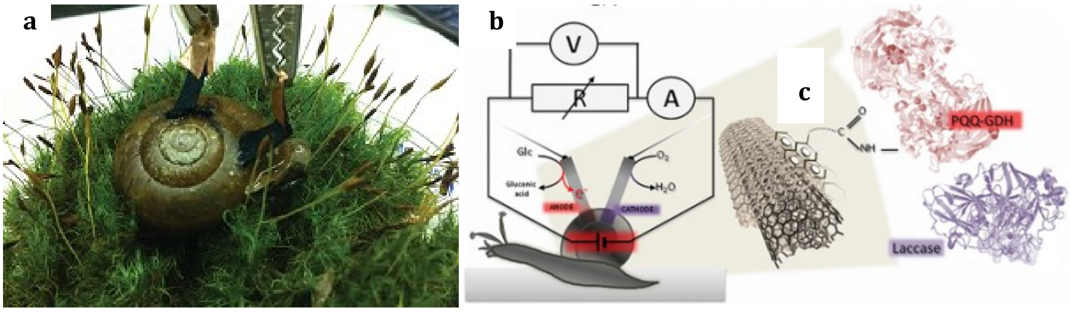

Figure 1.11 Biofuel cell inside a living snail with functionalized carbon nanotube electrodes (a) snail in experimental setup with implanted electrodes; (b) Schematic of circuitry inside the snail; (c) Glucose dehydrogenase (PQQ-GDH) and laccase enzymes immobilized to a pair of CNTs generate electricity inside the haemolymph of a snail. Figures adapted from reference [50].

biosensing applications, e.g. monitoring of certain species in wastewater treatment. Recently *in vivo* applications have been successfully demonstrated as well [51]. Demonstrated examples include operational biofuel cells inside snails [52] (Figure 1.11), clams [53], lobsters [54], rats [55], and cockroaches [56].

A different concept for harvesting of bioelectricity *in vivo* was successfully demonstrated was by Mercier et al. [57, 58]. Instead of using electrodes functionalized with enzymes or bacteria, a pair of glass microelectrodes was inserted into the perilymph and endolymph compartments inside the cochlea of a living guinea pig, which are at different electrochemical potential (Figure 1.12). The physiological function of the cochlea is the mechanotransduction of (mechanical) sound-waves into nervous impulses. The electrodes were connected to a customized microelectronic chip with integrated charge collectors and amplifiers, that were shown to be capable of powering a wireless transmitter that provided information of the electrochemical potential gradient present at the electrode tips. Wireless transmission was maintained over several hours, while neurological studies suggested that the hearing-capabilities of the guinea pig were not significantly impaired.

The above mentioned example is of special interest within the context of this work, as nanoelectrode ensembles developed in this work could possibly be employed in a similar concept. The transmembrane potential of living cells potentially provides a source of electrical current. If large numbers of cells could be electrically contacted simultaneously using a NEE-surface, an electric current generated from these cells may be used to drive low power electronics, e.g. in sensory implants.

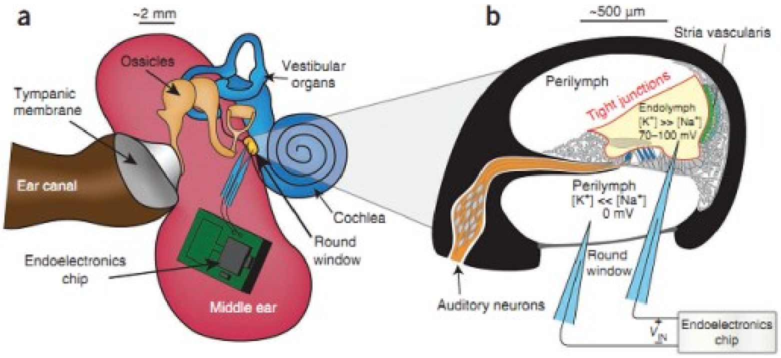

Figure 1.12 Energy harvesting from the endocochlea-potential (EP) Endolymph and perilymph, two separated compartments of different electrochemical potential in the cochlea of a live guinea pig were accessed by insertion of glass microelectrodes. From this gradient a total power of 1,1 nW was drawn and used to power a specifically designed circuit, allowing wireless transmission of measurements of the endocochlear potential. Neurophysiological experiments indicated no significant impairing of the animals hearing capacities. Adapted from reference [58].

2 Theory

2.1 Membrane Potentials

2.1.1 The Cellular Membrane

Eukaryotic cells are building blocks of all mammalian tissue. Although there are hundreds of cell types in organs and tissue serving various purposes, all cells share certain features such as nucleus, ribosome, mitochondria, endoplasmic reticulum, golgi body and most importantly (in this work) the plasma membrane. It fulfils a barrier-function separating the intracellular space from its environment and regulating the exchange of ions and molecules between the cell and its environment. It participates in a variety of processes in intercellular- and cell-matrix-contacts like cell-adhesion, cell-migration, signalling and metabolism.

Main constituents of the cellular membrane are phospho- and glycolipids which due to their amphiphilic properties form the lipid-bilayer of approximately 5 nm width (Figure 2.1) [59]. Phospholipids consist of a hydrophilic head group which orientates towards the outside of the bilayer and a lipophilic tail with inward orientation. Two types of phospholipids are present in

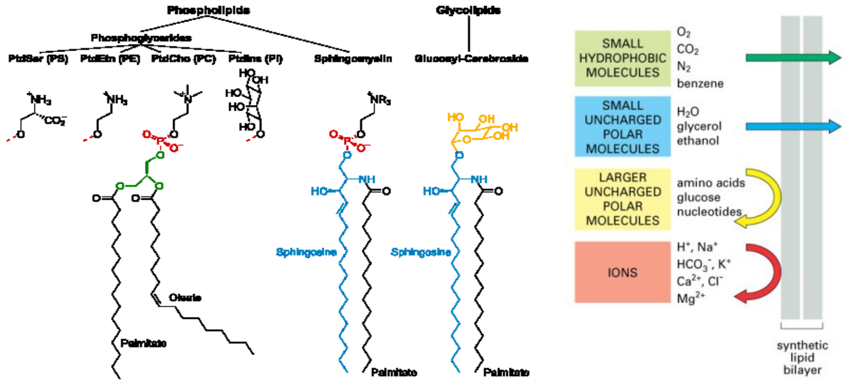

Figure 2.1 Constituents an permeability of the cellular membrane (left) Chemical structure of most important phosholipids within the membrane. Adapted from reference [59]; (right) Scheme of the membranes permeability towards certain ionic and molecular species. Small uncharged molecules with hydrophobic or polar properties like diatomic gases, (unsaturated) carbohydrates, alcohols and water can diffuse throught he membrane. To large polar molecules like sugars and amino acids and charged ions the membrane is impermeable. Adapted from reference [4].

biological membranes, distinguished by their chemical structure: *glycerophospholipids* (glycerol connecting head and tail) and *sphingolipids* (sphingosine (and its derivatives) as backbone structure with a wide variety of head groups). The membranes structure was initially described by the fluid-mosaic-model introduced by SINGER and NICOLSON which predicts lateral freedom of movement for the constituents within the lipid bilayer [60]. Recent findings challenge this theory, documenting a certain degree of organization within the membrane termed lipid rafts [61]. According to this model certain short-range ordered structures exist within the membrane. Interactions with and intra- and extracellular structures like the actin-cytosceleton and the extracellular matrix contribute to this localization of certain membrane proteins.

Within the plasma membrane numerous types of *membrane proteins* are embedded, serving a variety of functions such as signalling, metabolism, adhesion and sensing of the extracellular environment (Figure 2.2) [62]. *Peripheral membrane proteins* only temporarily attach to the membrane as opposed to *integral membrane proteins*, which are embedded in the lipid bilayer permanently. Two subgroups of integral membrane proteins are distinguished: *integral monoptic proteins* only attach to one side of the membrane while *transmembrane proteins* span the entire width of the lipid bilayer. *Membrane transport proteins* belong to the latter category, allowing and regulating the transport of ions and molecules across the membrane. Besides fulfilment of the above mentioned functions, continuous transport of ions is crucial for regulation of the membrane potential.

Channel proteins form pores, selectively allowing diffusion of certain ions along a concentration gradient. Channels can be permanently open (*leakage channels*), or allow flow only upon certain trigger events (*gated channels*). This does not consume metabolic energy and is also considered as passive transport. Classification of *gated ion channels* relates to their primary triggering cues,

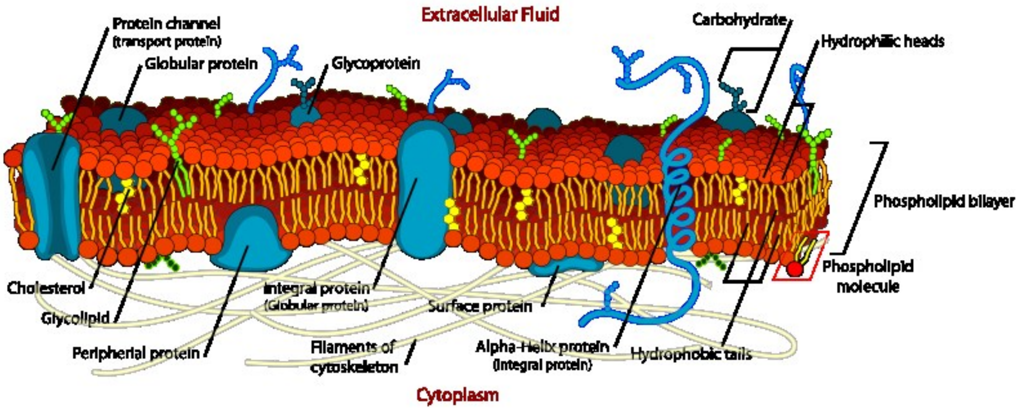

Figure 2.2 Scheme of the plasma membrane with different types of membrane proteins
Phospholipids with hydrophilic heads (red spheres) and lipophilic tails (yellow) constitute the lipid bilayer in which various types of membrane proteins are embedded. Adapted from reference [62].

e.g. voltage-, ligand-, temperature- and light-gated or mechanosensitive ion channels. Transport through ion channels is relatively fast, therefore among many other functions, they play a key role in conduction of nervous impulses and muscle contraction.

Active transport against chemical gradients is crucial to provide cells with nutrients and to balance the perturbations caused by ion fluxes through channel proteins and thus restoring the resting potential of the cell (see below). This is achieved by a conformational change in the transporter protein after the molecule to be transported has been bound. Primary active transport consumes metabolic energy from cellular energy carriers, e.g. ATP or NADH to power the conformational change in the transporter protein. Secondary active transport by sym- or anti-porters uses a chemical gradient of Na^+ or K^+ to shuttle molecules in or against the direction of a chemical gradient. Other paths of transmembrane transport (exo- and endocytosis) are of great importance as well, but shall not be discussed here.

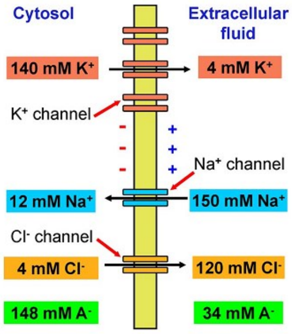

Figure 2.3 Typical intra- and extracellular ion concentrations of a cell Arrows indicate ion flux in direction of the respective concentration gradients. The symbol A^- represents all anions other than chloride. Adapted from reference [5]

2.1.2 The Membrane Resting Potential

The resting membrane potential is a key attribute and of vital importance for any cell's viability. It arises from diffusion of different ionic species, mainly Na^+, K^+, Ca^{2+}, and Cl^- between in- and outside of a cell. Without ion channels allowing constant flow of ions through the membrane, the resting potential would not exist. Inside a cell an excess of K^+ is present, the concentrations of

Table 2.1 Ion concentrations in- and outside of different cell types Adapted from reference [8]

	Squid Axon		**Frog muscle**		**Mammalian muscle**		**Ratio**
	Outside	**Inside**	**Outside**	**Inside**	**Outside**	**Inside**	$\frac{\textbf{Outside}}{\textbf{Inside}}$
Na^+	460	50	120	9,2	145	12	~10
K^+	10	400	2,5	140	4	155	$\sim40^{-1}$
Ca^{2+}	11	$3x10^{-4}$	1,8	$3x10^{-4}$	1,5	$<10^{-4}$	$\sim10^{-4}$
Cl^-	540	40-100	120	3-4	123	4,2	variable
E_R	-60		-90		-90		

Na^+, Ca^{2+}, and Cl^- and larger on the outside (Figure 2.3). Absolute concentrations of different ions vary between cells types and organisms and so does the value of the membrane potential; some examples are listed in Table 2.1. Negative charges to fulfil the requirement of electro-neutrality are mostly provided by chloride-ions on the outside of the cell, while inside the cell the negative charges are predominantly located on proteins.

Concentration differences are actively maintained by ion-transporting membrane proteins, constantly compensating the ion stream through open pores. The presence of leakage channels is a unchallengeable requirement for the establishment of the transmembrane potential. Active and passive transport at the plasma membrane maintain a dynamic equilibrium state which gives rise to the transmembrane potential. For electrically quiescent cells or electrically active cells in their unperturbed state it is also referred to as membrane resting potential. Potentials arising from differences in ion concentrations can be described by the Nernst equation:

$$E_m = \frac{\mathrm{R}\,T}{z\,\mathrm{F}} \ln\left(\frac{c_{out}}{c_{in}}\right) \tag{2.1}$$

In this equation the is the membrane resting potential E_M depends on the absolute temperature T, the number of charges transferred z and the ionic concentration $c_\mathrm{in/out}$. Constants in this equation are the universal gas constant R and the Faraday constant F. For higher accuracy instead of concentrations the activities of the ionic species can be used:

$$a_x = \gamma_x \cdot c_x \tag{2.2}$$

The specific activity coefficient γ compensates for interionic interactions. However at physiological concentration levels, the activities of the contemptable ions are close to one, therefore calculations are often performed using concentrations. Different expressions of the Nernst equation may be derived depending on the problem at hand. The straightforward calculation of the potential using the Nernst-equation and summation of the values for individual ion species does not provide an accurate result. The result would only be valid if all ions would permeate the cell membrane equally which is not true. Instead an expression taking into account the contributions of all relevant ionic species introduced by GOLDMAN, HODGKIN and KATZ provides a more accurate result:

$$E_m = \frac{RT}{F} \ln\left(\frac{P_{\mathrm{Na}^+}[\mathrm{Na}^+]_{out} + P_{\mathrm{K}^+}[\mathrm{K}^+]_{out} + P_{\mathrm{Cl}^-}[\mathrm{Cl}^-]_{in}}{P_{\mathrm{Na}^+}[\mathrm{Na}^+]_{in} + P_{\mathrm{K}^+}[\mathrm{K}^+]_{in} + P_{\mathrm{Cl}^-}[\mathrm{Cl}^-]_{out}}\right) \tag{2.3}$$

With:

$$P_X = \frac{D_x}{a} \tag{2.4}$$

This equation features the respective permeability of the plasma membrane P_x representing for each ionic species. D_x is the diffusion coefficient of ionic species x and a is the width of the membrane. Although the equation shows a certain similarity to the Nernst equation, it is derived following a different approach, assuming an equilibrium state for the flow of ions across the membrane. When the cell membrane is in a steady state, the sum of all in- and outflowing currents must be equal to zero:

$$I_{\mathrm{Na}^+} + I_{\mathrm{K}^+} + I_{\mathrm{Cl}^-} = 0 \tag{2.5}$$

Assuming only these three ionic species contribute to the membrane potential. The flow of an ionic species is determined by two competing gradients: the concentration gradient *dc/dx* and the electrical field gradient *dE/dx*. Both contributions sum up to the electrochemical potential μ which is defined by:

$$\frac{d\mu}{dx} = \frac{d}{dx}\left(\mu^0 + RT\ln c\right) + zF\frac{dE}{dx} \tag{2.6}$$

In this equation μ^0 is chemical potential at standard conditions. The current for an ionic species can be defined using chemical potential in the Nernst-Planck-equation:

$$I_x = \frac{z\,F\,D_x}{R\,T}\,\mathrm{c}\,\frac{\mathrm{d}\mu}{\mathrm{dx}} \tag{2.7}$$

Which can also be stated as:

$$I_x = -z\,F\,D_x\left(\frac{\mathrm{dc}}{\mathrm{dx}} + \frac{z\,F\,c_x}{R\,T}\frac{dE}{dx}\right) \tag{2.8}$$

The diffusion coefficient D_x for a certain species of ions and is defined by

$$D_x = \frac{RT}{F}\cdot u \tag{2.9}$$

The diffusion coefficient depends on the ionic mobility u. Since the Nernst equation describes a state of thermodynamic equilibrium, it cannot be directly applied to the context of a cell which has rather to be perceived as dynamic equilibrium. Integration of equation 2.6 for I = 0 with the boundaries $E_0 = E_{out} = 0$ and $E_a = E_{in} = -E$ directly leads to the Nernst equation 2.1.

$$I_x = \frac{-z\,F\,D_x}{e^{\frac{zFE}{RT}}}\,\frac{d\left(c_x e^{\frac{zFE}{RT}}\right)}{dx} = -zF\,\frac{c_{in}e^{\frac{zFE}{RT}} - c_{out}}{\int_0^a \frac{e^{\frac{zFE}{RT}}}{D_x}\,dx} \tag{2.10}$$

For the integration of this equation three assuptions have to be made:

(i) Independent ion movement

(ii) Constant diffusion across the membrane

(iii) Constant electric field across the membrane

If these conditions are not fulfilled, more complex theoretical descriptions would be required. From equation 2.10 the Goldman-Hodgkin-Katz flux equation may be obtained:

$$I_x = (zF)^2 \frac{E}{RT} \frac{D_x}{a} \frac{c_{in}\, e^{\frac{zFE}{RT}} - c_{out}}{e^{\frac{zFE}{RT}} - 1} \tag{2.11}$$

A very important procedure in electrophysiological research is the determination of voltage-current-relationships. According to Ohm’s law this relationship is linear, but this is not true for the transmembrane potential and the corresponding ionic currents. This would only be the case for equal concentrations in- and outside of the cell which is not the case in biological cells. Instead non-linear behaviour as depicted in Figure 2.4 is observed in corresponding experiments, confirming the predictions made by the GHK-equations, despite the rather restrictive assumptions made in its theoretical derivation.

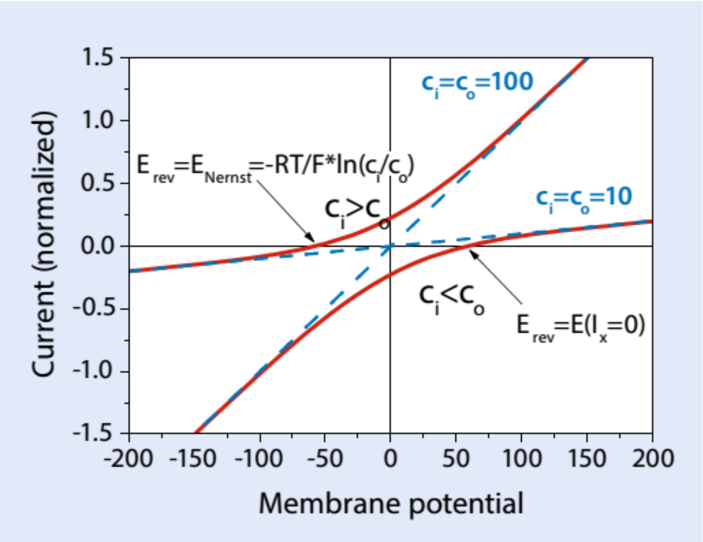

Figure 2.4 Current-Voltage-relationship Red lines indicate real behaviour, blue dashed lines ideal Ohmic behaviour. The inflection of the curves depends on whether the concentration in- or outside of the cell is bigger. In both cases the trace crosses the x-axis at the Nernst-potential when the current is zero. Adapted from reference [8].

2.1.3 Action Potentials

Electrically excitable cells, e.g. neurons and muscle cells can undergo rapid fluctuations of their membrane potentials which are called action potentials (APs). The firing of neuronal APs lasts only few milliseconds, in muscle cells APs may last tens of milliseconds. These fluctuations are the underlying physicochemical process responsible for neuronal signalling and muscle contractions.

The physical origin of APs is an increased ionic flow through gated channels in the cellular membrane. Usually sodium and potassium are the main protagonists in such events, but APs originating from calcium and chloride fluctuations are known as well, e.g. e in (cardiac) muscle cells. APs are triggered by external stimuli causing the opening of gated channels, thereby leading to an initial perturbation of the cells membrane potential. Upon crossing of a certain threshold value, a positive feedback mechanism causes rapid opening of inward voltage-gated sodium channels leading to a rise of the membrane potential which can eventually even become positive. This change triggers outward-bound voltage-gated potassium channels. The outward flow of potassium balances the excess of positive charge inside the cell and returns the potential back to its initial value, eventually causing some overshooting. This overshoot is compensated during the refractory period by ion transporters such as the Na-K-Antiporter, returning the cell to its initial state. The discovery of this mechanism by Hodgkin and Huxley in the 1950s marks a major breakthrough in history of biophysics. It should be noted, that the overall flux of ions during an action potential is does not cause relevant changes in overall concentration level of involved ion species in- or outside the cell.

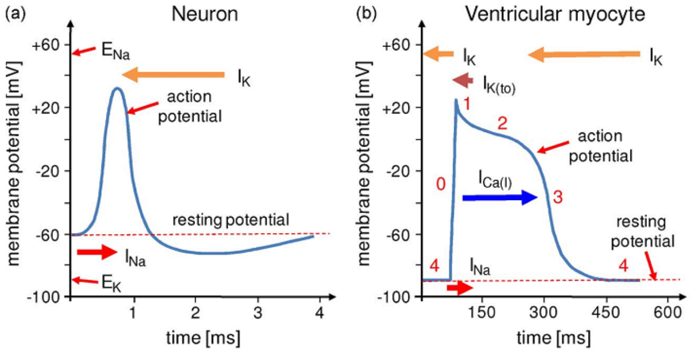

Figure 2.5 Development of action potentials in different cell types (a) In a neuron the opening of inward Na^+-channels leads to depolarization of the cell which is compensated by the opening of voltage-gated K^+-channels. The influx of K^+ restores the resting potential eventually causing some overshooting which is balanced within a few milliseconds; (b) Action potential of a cardiac muscle cell with participation of Ca^{2+}-ions. Adapted from reference [4].

2.1.4 Measurement of Membrane Potentials

A brief history of the discovery of electric phenomena in biological context was already given in the introduction. This section will focus in more detail on current experimental techniques used to measure cellular potentials. Figure 2.7 summarizes various methods currently used in scientific laboratories for interfacing cells for electrophysiological measurements.

Electrophysiological measurements are usually performed based on the concepts of either current- or voltage-clamp methods, in which the “clamped” quantity is controlled while the complementary voltage or current is being measured. Depending on the problem at hand many variations such experiments have been developed to address numerous questions in electrophysiology [63]. The classic approach using glass microelectrodes inserted into cells or in contact with the cellular membrane benefit from the high precision achievable with such recording techniques (Figure 2.7a). Such microelectrodes are filled with an electrolyte solution in which a metallic wire is immersed. Electrical contact is established via the opening at the tip of the microelectrode of only few micrometres in diameter, where the filling electrolyte comes into contact with the intracellular space or a patch of the cell membrane. This method provides highly localized electrical contact with very low impedance. At the same time this also poses the biggest drawback of this method, as diffusion of the electrode’s filling solution into the cell contaminates the cytosol limiting the cells viability with respect to time (Figure 2.7b). Additional limiting factors are the requirements for extensive equipment such as microscopes and micromanipulators which need to be operated by trained personnel (Figure 2.6) [64].

To overcome these disadvantages, microelectrode array platforms have been developed in numerous variants. Conventional MEAs feature flat microelectrodes on which interfacing with single cells or clusters of cells are established by simple incubation of the cells on top of the electrodes (Figure 2.7 c). Such devices do not inflict mechanical damage to the cell and allow long-term experiments with cells kept viable up to several weeks. Electrodes can be arranged in arrays of many thousands of electrodes, allowing measurements with spacial resolution.

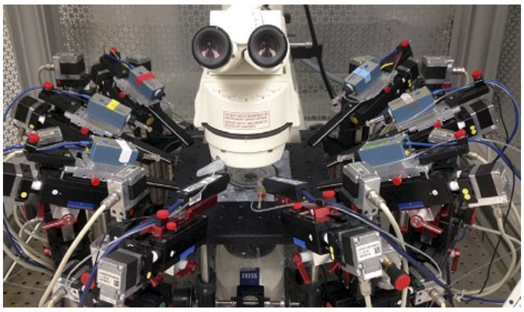

Figure 2.6 Various patch-clamp units assembled to a single microscope The spacial requirements of micromanipulators limit their simultaneous use in multi-cell interrogating experiments. Adapted from reference [64].

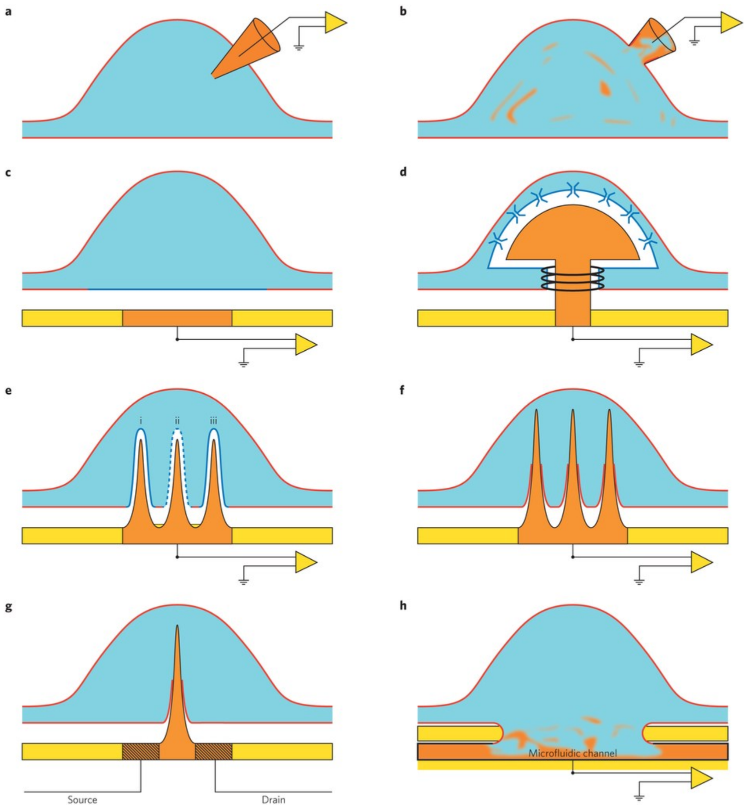

Figure 2.7 Various modes of interfacing cells for electrical measurements Schematic representation various cell-electrode configurations: (a) intracellular microelectrode; (b) patch electrode, orange blurs indicating mixing of the electrolyte with the cytosol; (c) flat electrode for extracellular measurement; (d) mushroom-shaped electrode with indicated actin rings strengthening cell bonding to the electrode; (e) vertical electrodes in (i) initial state with membrane protrusion around the electrode, (ii) with ruptured membrane after electroporation pulse and (iii) with reassembled membrane; (f) ensemble of vertical electrodes with intracellular access; (g) intracellular FET electrode (source and drain brown color); (h) microfluidic electrode. Coloring scheme: cell membrane – red, cytosol - light blue, working electrodes - orange, supporting structures- yellow. Adapted from reference [34].

Nevertheless these systems suffer from poor signal-to-noise ratio and low amplitude as the flat electrodes do not measure the transmembrane potential directly, because the dielectric properties of the cellular membrane do not allow a direct measurement of the membrane potential with flat electrodes. Instead the extracellular field potential (FP) resulting from fluctuations of ion concentrations as the cell undergoes an action potential is detected. The recorded FPs usually only have an amplitude of few microvolts (Figure 1.5). Other platforms detect change of the electrical field as a result of changes of ion concentrations inside the cell were detected using arrays of field-effect transistors (FETs) as realized by Fromherz et al. in the early 1990s [23]. A comparison of cellular recording with intra- and extracellular electrodes is provided in Figure 2.8.

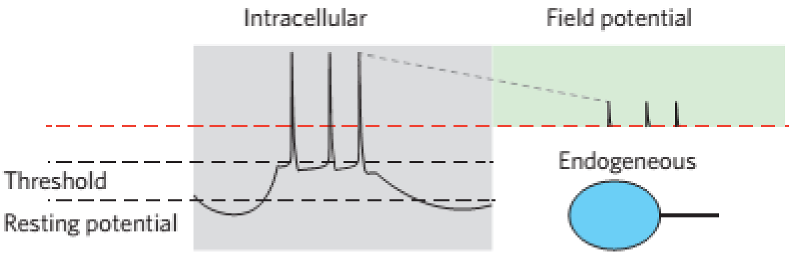

Figure 2.8 Extracellular field potential picked up by an external micro-electrode On the left side an intracellular spike-train as measured with a conventional microelectrode is seen, (right) signal recorded with an extracellular electrode. Information contained in sub-threshold potential fluctuations cannot be detected using flat microelectrodes. Adapted from reference [34].

The emergence of vertical nanostructures has led to paradigm shift in intracellular recording. The use of vertical structures protruding from a surface on which cells are incubated as electrodes for measurement of cellular potentials allowed an impressive increase of the cell-electrode coupling coefficient. Such structures have advantageous properties in terms of diffusion and charge transfer in electrochemical experiments as their size approaches the dimension of the diffusion layer governing electrode processes [65, 66]. One of the first examples demonstrating such coupling were mushroom-shaped electrodes developed by Spira and Hai [30-32]. Numerous other publications introduced variants of this concept using different electrode geometries, materials and concepts for interfacing (Figure 2.7 d-g). Various aspects of intracellular measurements with such structures shall be discussed in the section below. Electrical contacting of cells through microfluidic channels as displayed in Figure 2.7 f is a rather exotic approach, used e.g. in automated patch-clamp or other microfluidic devices.

2.1.5 Intracellular Access of Nanoelectrodes

The penetration of vertical nanostructures through the cellular membrane is of critical importance for successful intracellular recording with such devices. Numerous studies covering individual examples or attempting to develop a generalized theory of nanowire penetration through the cellular membrane have been published. Despite these efforts there is still a controversial debate on this question. Numerous factors are influencing the process of internalization, among which are electrode height and diameter, geometry, material, interelectrode distance (pitch), surface structure and cell type used in the experiment. Therefore the question whether a vertical nanostructure does actually penetrate a cell still needs to be addressed for each individual case and con not be assumed a given condition.

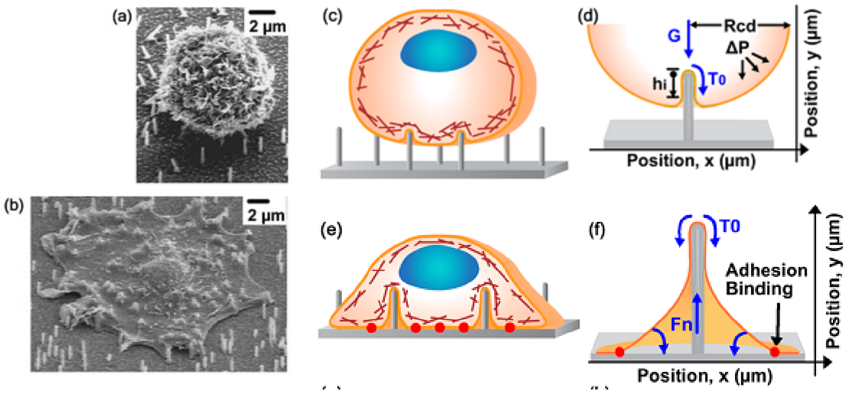

Figure 2.9 Theoretical model of nanowire penetration CHO cell on an SiNW-surface (a) before and (b) after spreading; (c) scheme of a cell settling on top vertical nanowires by sedimentation; (d) forces occuring from indentation of the ell membrane during sedimentation; (e) cell adhered to a nanowire substrate; (f) forces occurring during during the formation of focal adhesions (red points). Adapted from reference [67].

A theoretical study on the penetration of nanowires through the cellular membrane was published by MELOSH et al. dealing with the most common case of interfacing cells with cylindrical nanowires by simple incubation on the surface (Figure 2.9) [67]. Parameters studied in this publication are the aspect ratio of the wire (height/diameter) and the stiffness of the cell membrane. When cells are seeded on nanowires, the first interaction with the nanowires occurs when the suspended cells sediment onto the surface driven by gravitation. The force occurring at the tip of the nanowire indenting the cell upon this event is in the range of nN and hence at least an order of magnitude weaker than required. After sedimentation cells adhere and spread to the surface and thereby additional tension forces may occur as the membrane is stretched over the nanowire in a tent-like structure. This mechanism is more likely to lead to penetration. In both cases penetration smaller tip diameters and stiffer cells are more likely to penetrate.

Determination of nanowire penetration is problematic as the width of the membrane of only 5 nm is rather small. Often FIB-SEM or TEM images are provided to illustrate the penetration of nanostructures into cells, but such images cannot provide final proof whether or not the membrane is ruptured [68, 69]. During the process of fixation and drying of samples in preparation for FIB, artefacts may occur falsifying the actual situation. In addition the membrane is difficult to distinguish from other components of the cell given limited contrast of such organic samples, even when contrast enhancing compounds like OsO_4 are used. Imaging of the cell-nanowire interface with optical or fluorescence microscopy is also problematic as the resolution is not sufficient. Fluorescence labelling membranes can lead to false conclusions as the metallic electrodes in the vicinity of fluorophores may act as quencher and thereby the absence of fluorescence may be misinterpreted as false penetration.

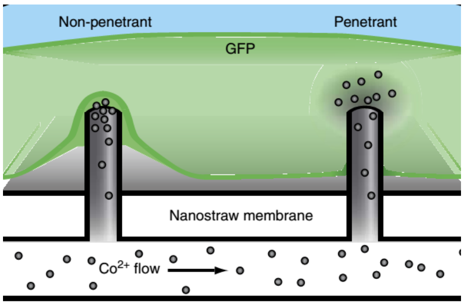

Figure 2.11 Perfusion of cells via intracellular nanostraws Hollow nanowires, also referred to as nanostraws, are connected via an underlying micrufluidic perfusion channel. Co^{2+}-ions perfused through this channel quench the fluorescens of GFP inside the cell in case of succesful penetration of a nanostraw through the cell membrane. Adapted from reference [70].

One approach to quantify the penetration of nanowires into cells was performed with hollow nanostraws allowing microfluidic access to the cytosol (Figure 2.11) [70]. The nanostraws were 100 nm in diameter and 1-2 µm in height and thereby of similar dimensions as the nanowires used in this work [71]. Cells expressing GFP were incubated on such nanostraws while a solution of Co^{2+} was perfused through microfluidic channels underneath. In the case of intracellular access, Co^{2+} injected into the cells would quench the fluorescence of GFP locally and thereby indicate intracellular access. It was shown that at average only 7,1 % of the straws gained access to the intracellular space. Observations over time revealed an adhesion-dependent penetration mechanism accompanied by the formation of focal adhesions as predicted in the theoretical study mentioned above.

Another important parameter is the density of the nanowires on the surface (Figure 2.10). When only few nanowires are present at the surface, cells will readily adhere to the surrounding surface and form a protrusion of their membrane around the wires, unless a penetration event

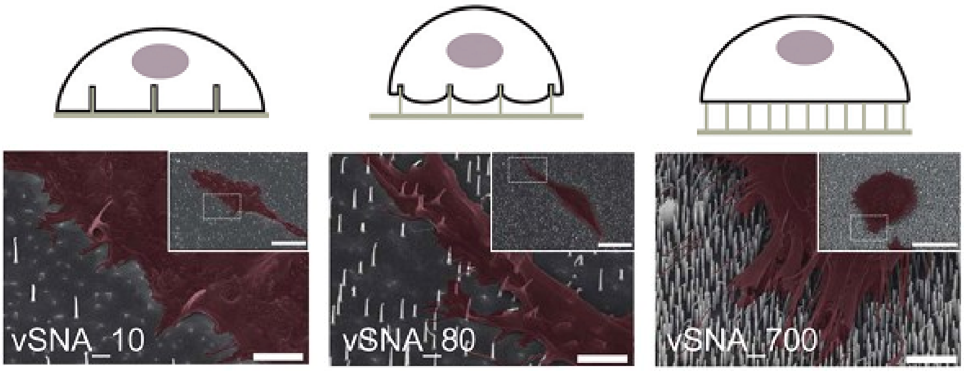

Figure 2.10 Cells on nanowire ensembles of different densities Cells on low-density NW-surfaces will adhere to the underlying surface. Medium density NWs cells reside on top of few NWs, resulting in large forces indenting the membrane. High density NWs distrubute the occuring forces evenly so adhesion is similar to rough surface with defined adhesioin sites. Adapted from reference [72].

occurs as discussed above. If the density of the nanowires becomes higher, cells will rather reside on top of the nanowires than on the substrate surface underneath where several nanowires are in close proximity to other. At very high densities the entire cell will sit on top of the wires forming adhesion structures on many of them [72].

2.2 Deposition of Metallic Thin Films

Homogeneous thin films of metals can be created via physical vapour deposition (PVD) methods. Applications of PVD are manufacturing of coatings for optical, electrical or mechanical purposes, e.g. in semi-conductor manufacturing, packaging materials and electrodes. The most common PVD methods are evaporation and sputtering. Both feature material transfer to the sample under vacuum conditions. Typical pressure ranges are between $10^{-1} - 10^{-6}$ mbar, whereas evaporation devices operate at lower pressures because they require longer mean free path for ballistic travel of evaporated particles towards the substrate.

2.2.1 Evaporation Techniques

Inherently this method is characterized by the thermal evaporation of the material which shall be coated. The material is heated close to or beyond its melting point, allowing a phase transition from solid or liquid to the gas phase. Therefore this method is limited to the processing of materials, which are not subject to decomposition upon thermal stress. This requirement is met by pure metals, certain alloys and inorganic salts e.g. halides, oxides or sulphides. Examples for evaporation methods are:

- Thermal Evaporation
- Electron beam evaporation
- Laser beam evaporation
- Light arc evaporation

As atoms or clusters are evaporated from the bulk material, they either travel along a ballistic path or are guided by an electric field or a negative bias voltage before deposition on the specimen and the chamber walls [73]. The low pressure inside the process chamber of 10^{-4} - 10^{-6} mbar ensures free travel of the particles, avoiding deflection by collision with gas molecules. At the same time it avoids the formation of oxides or nitrides, as the ejected metals may undergo chemical reactions resulting in undesired composition of the deposited film.

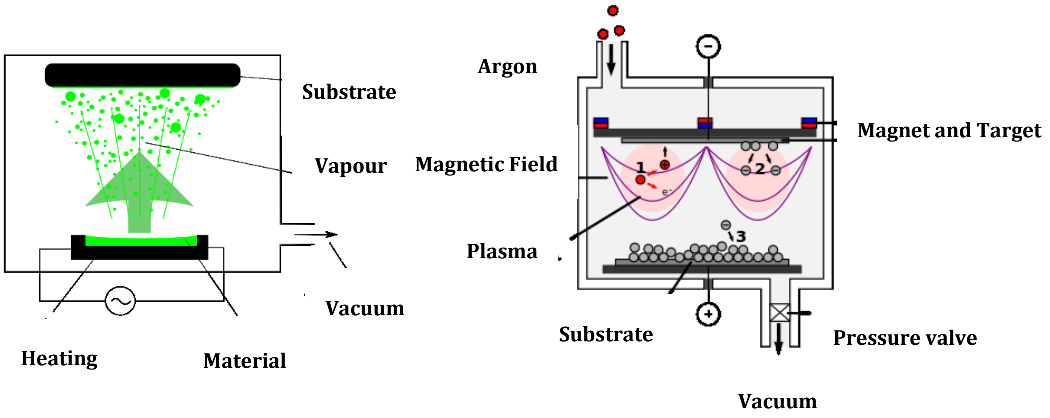

Figure 2.12 Schematic description of physical vapor deposition and sputtering (a) Inside a vacuum chamber the material to be deposited is evaporated, usually by an electrical heater. The prevalent vacuum inside the chamber allows free ballistic travel of metal atoms leaving the surface of the molten metal. Adapted from reference [73]. (b) In a magnetron sputter argon is ionized at the cathode. The resulting plasma is confined by permanent magnets above the electrode. Ionized atoms are attracted towards the cathode by the bias voltage and eject atoms from the target upon impact. Adapted from reference [74].

Although in certain processes these reactions may be desired to deposit oxide or nitride compounds and therefore a low pressure atmosphere of a reactive gas may be allowed inside the process chamber. Depending on the incident angle of the particle stream, inhomogenities in film thickness of the deposited material and shading effects may occur, since the evaporated particles move along a straight trajectory. Shading is avoided or reduced by out-of-centre rotation of the sample holder varying the incident angle and/or heating of the substrate holder, allowing the deposited material to travel on the substrate surface before condensation.

2.2.2 Sputter deposition

Sputtering (or cathodic deposition) ejects atoms or clusters from a metal target by accelerating ions towards the target. Upon impact material is ejected from the target and deposited on the substrate. Therefore materials with high melting points can be processed, which are problematic in evaporation processes due to the thermal integrity of the chamber components. For the same reason the processing of substrates sensitive to thermal stresses is possible with sputtering processes [74]. As for evaporation, numerous types of sputtering devices exist. Conventional sputtering processes are carried out in a low pressure vacuum chamber. A constant pressure inert gas atmosphere (usually argon, but other gases are possible) is created inside the chamber by controlled flow of gas into the chamber. The inert gas is ionized by glow discharge between the target cathode and the substrate holder serving as anode by a DC or High

Frequency-AC (HF) potential. Due to the higher pressure inside the process chamber, the ejected particles move rather in a diffusive manner. To avoid excessive heating of the target a water cooling is usually implemented which becomes increasingly necessary when sputtering of thick films over long periods of time is performed. The structure of the obtained film is governed by argon pressure, target-substrate distance, sputtering current, stationary or rotating sputtering and of course the material itself. Although there are theoretical models describing the sputtering process, these parameters usually have to be established empirically and require constant verification as aging and wearing of the target may alter the obtained results.

2.3 Cyclic Voltammetry

Cyclic Voltammetry (CV) is an analytical method providing a versatile tool for the analysis of electrochemistry in liquid phases. Depending on the design of the experiment, processes at the electrodes or within the liquid such as diffusion, redox properties of certain molecules and kinetics of chemical reactions can be investigated. Either a set of electrodes with known characteristics can be used to determine properties of dissolved molecules, or a solution of a redox-active species with known properties is used to probe the behaviour of an electrode. The latter is the case in this work. Voltammetry experiments observe the current i while a change of potential E is imposed on the observed system within certain time t. The most important factors governing the current response of the experiment are reaction kinetics and mass transport to and from the electrode. To avoid oxidation or reduction of the solvent in use, the potential of the vertex points should be within the solvents electrochemical window. The electrochemical window defines the potential range in which no oxidation or reduction of the solvent occurs. Counter electrodes are usually made of inert noble metals e.g. gold or platinum.

2.3.1 Voltammetry Basics

Voltammetry experiments are usually performed with a three electrode setup allowing for independent measurement of potential and current (Figure 2.13a). Simultaneous measurement of current and potential in a two-electrode configuration is not possible because the counter electrode would be subject to polarization as a current passes through it. Only for very small currents in the range of nA or pA the use of a two-electrode configuration may be possible, although such experiments are prone to error resulting from experimental difficulties when

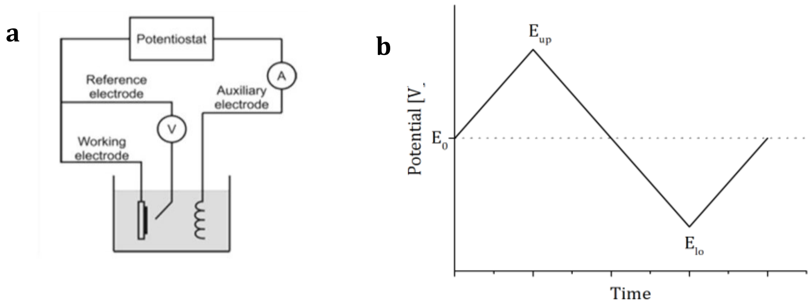

Figure 2.13 Cyclic voltammetry basics (a) scheme of a three electrode setup. (b), Starting at E_0 the potential is sweep to an upper vertex point E_{up}, then down to the lower vertex point E_{low} and then back to E_0.

measuring currents of such low magnitude. The potential is measured between working and reference electrode (RE), usually saturated calomel or Ag/AgCl.

In simple experiments like linear sweep voltammetry (LSV) the electric potential at the working electrode (WE) changed from a starting to end-potential while the resulting current between working and counter electrode (CE) is measured (Figure 2.14). The name of the method points out that LSV is basically an incomplete CV scan without the backward potential sweep [75].

At the beginning of the sweep no current is detected, until the potential closes in on the equilibrium species of the system where the current reaches its maximum value before asymptotically closing in to a constant value (Figure 2.14 left). The current peak is reached at equilibrium potential independently of the scan speeds unless reaction kinetics is slow. In this case the current peak potential will shift towards higher values (Figure 2.14 right). In CV experiments the sweep does not stop when the upper limit is reached, but instead changes direction and moves towards the lower vertex point (Figure 2.13). From there the potential returns back to its starting potential, completing the cycle. Experiments may end after completion of one cycle, although often several cycles in direct succession are performed to proof reproducibility or for investigation of reaction kinetics. This cycle may be repeated if the

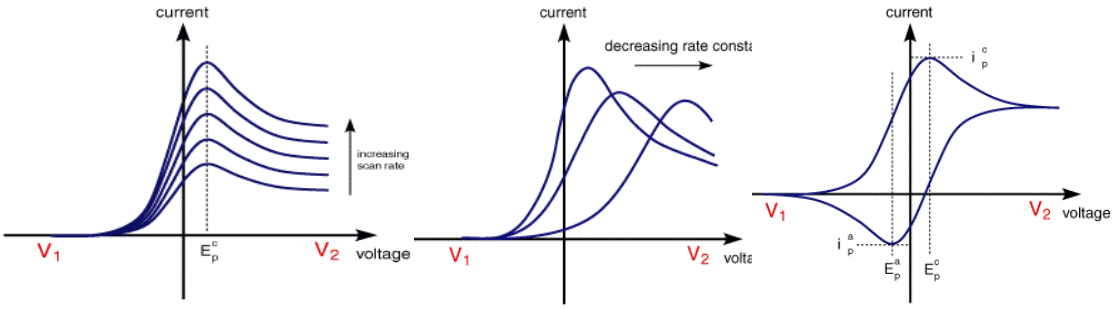

Figure 2.14 Linear sweep voltammetry Linear sweeps performed at different rates and resulting currents measured during such sweeps. Adapted from reference [75].

recorded voltammogram is not stable or if changes of the system over time shall be investigated. For an ideal system of full reversibility without adverse kinetic effects, the current response forms a closed loop displaying two symmetric peaks (Figure 2.13). From the position of anodic and cathodic peak potentials and the magnitude of the peak currents quantitative information about the system can be derived. The parameters governing the outcome of such experiments are:

Start Potential	E_0 / V
Upper vertex point	E_{up} / V
Lower vertex point	E_{lo} / V
Voltage sweep rate	ν / V s^{-1}
Temperature	T / °C
Solvent, Supporting Electrolyte	

The shape of a voltammogram is different to the logarithmic decay observed after a current step, as the steady increase of the potential beyond the equilibrium potential E_p induces an electrical field increasing discussion towards the electrode and thereby compensating for decreasing concentration of the analyte near the electrode surface. The the RANDLES-SEVCIK-equation describes the peak potential expected for a certain electrode:

$$I_p = 0{,}4463 \cdot z \cdot F \cdot A \cdot c_i^* \cdot \sqrt{\frac{z \cdot F \cdot v \cdot D}{RT}} \qquad (2.12)$$

This expression is often used to verify the reversibility of an electrode reaction. When the electrode surface area and the diffusion rate of the redox-active probe are known, the peak current I_p only depends on the potential sweep rate v. From a series of measurements at different sweep rates the peak current for each sweep rate is determined. If the plot of IP vs. v. provides a straight line, the reaction is reversible.

2.3.2 Diffusion Aspects

Diffusion towards the electrode is the governing factor in cyclic voltammetry. Depending on the size and geometry of an electrode, different theoretical models are required for an accurate description of the resulting currents. Mass transport to an electrode is governed by three factors:

- Migration
- Convection
- Diffusion

Migration and convection are both very difficult quantities in terms of theoretical handling; therefore their influence is usually reduced by appropriate design of the experiment. Migration is a result of forces exerted onto charged particles by an electric field. This effect is minimized by addition of a supporting electrolyte to the used solution with significantly higher concentration than the molecule of interest. The excess of supporting electrolyte dissipates the strength of the electric field reducing its effect on the species under investigation. Effects of convection are minimized by avoiding any mechanical perturbations which could induce forced convection inside the probe solution. Influences of natural convection present in any liquid can only be avoided by reducing the time of the experiment.

In the ideal CV experiment mass transport is solemnly governed by diffusion which can be comprehensively described theoretically by the general Nernst-Planck-Equation:

$$J_i = -D_i \nabla c_i - \frac{z_i F D_i c_i}{RT} \nabla \phi + \upsilon c_i \tag{2.13}$$

with

- J_i - total flux / mol s^{-1} cm^{-2}
- D_i - Diffusion coefficient of species I / cm^2 s^{-1}
- c_i – concentration of species I / mol
- z_i – number of charges carried by i
- ν – *velocity* / cm s^{-1}

The total current is related to the flux by:

$$J_i = \frac{I}{zFA} \tag{2.14}$$

- I – electrical current / A
- A - Area

Diffusion processes are described by Fick's first (eqn. 2.15) and second (eqn. 2.16) law, which in their general formulation are stated as:

$$J_i = -D_i \nabla c_i \tag{2.15}$$

$$\frac{\partial c_i}{\partial t} = -D_i \nabla^2 c_i \tag{2.16}$$

Equation 2.15 describes the magnitude of the flux J against a constant concentration gradient defined by ∇c_i. The negative prefix indicates, that in accordance with thermodynamics the flux will opposed to the concentration gradient. The second law (eqn. 2.16) also accounts for time-dependent gradients. These general forms of Fick's laws can be simplified for electrodes of specific geometries taking into account the geometrical boundary conditions for the case at hand. Most important cases are listed in Table 2.2.

Table 2.2 Diffusion equations for various electrode geometries

Electrode geometry	Diffusion equation	
Planar	$\frac{\partial c}{\partial t} = D\left(\frac{\partial^2 c}{\partial x^2}\right)$	(2.17)
Hemisphere	$\frac{\partial c}{\partial t} = D\left(\frac{\partial^2 c}{\partial r^2} + \frac{2}{r}\frac{\partial c}{\partial r}\right)$	(2.18)
Cylinder	$\frac{\partial c}{\partial t} = D\left(\frac{\partial^2 c}{\partial r^2} + \frac{1}{r}\frac{\partial c}{\partial r}\right)$	(2.19)
Microdisk	$\frac{\partial c}{\partial t} = D\left(\frac{\partial^2 c}{\partial r^2} + \frac{1}{r}\frac{\partial c}{\partial r} + \frac{\partial^2 c}{\partial z^2}\right)$	(2.20)

These equations can be solved by Laplace-transformation making appropriate choices for boundary conditions. Under the assumption of strict diffusion control of the reaction at the electrode surface, the COTTRELL-equation for planar electrodes of macroscopic dimensions can be obtained:

$$I_t = \frac{zFAc_i^*\sqrt{D}}{\sqrt{\pi t}} \tag{2.21}$$

According to this equation the concentration of species i is inversely proportional to $\sqrt{t}$, therefore a rapid decrease of the concentration of i takes place as a potential step is applied. This equation is valid as long as only linear diffusion to a macroscopic surface occurs. For electrodes of micrometre-dimensions edge-effect gain significance as the dimensions of the electrode approach the thickness of the diffusion layer. If the diffusion equations are solved for a spherical electrode the following equation containing two terms is obtained:

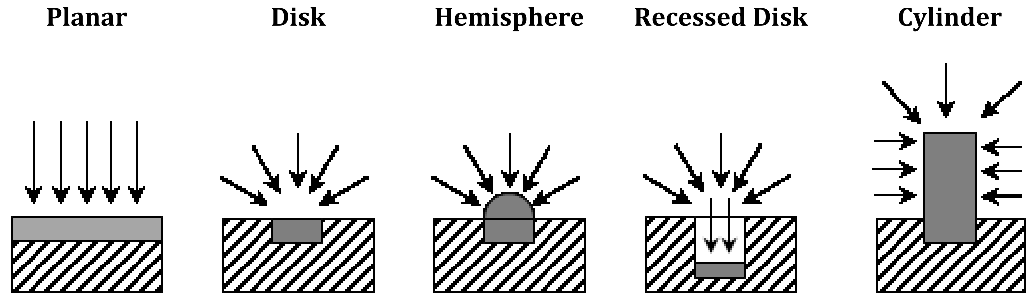

$$I_t = \frac{zFAc_i^*\sqrt{D}}{\sqrt{\pi t}}$$

Cottrell-Eq.

$$I = 4\pi FDca$$

$$I = 2\pi FDcr$$

$$I = \frac{4\pi FDca}{4L + \pi r}$$

$$I = \frac{2nFADc}{r\ln(\frac{4Dt}{r^2})}$$

Figure 2.15 Limiting current for different microelectrode geometries

$$I_t = \frac{znFAc_i^*\sqrt{D}}{\sqrt{\pi t}} + \frac{znFAc_i^*D}{r} \tag{2.22}$$

Only one of the terms on this equation is time-dependent, therefore the first term approaches a constant value as t→0 and the second term becomes negligible. At long times the second term becomes dominant and the system reaches a steady state. For this reason electrodes of appropriate dimensions and geometries may exhibit superior performance in electrochemical experiments.

2.4 Electrochemical Impedance Spectroscopy

Electrochemical impedance spectroscopy (EIS) is used to obtain information about electric properties of electrodes. Resulting current and phase shift of a sinusoidal ac-potential applied to a system are measured over a frequency range covering several decades. It provides a versatile, non-destructive measurement tool as it only requires potentials of very low amplitude. The obtained data is analysed by equivalent circuit modelling: Based on the physical composition of the electrode-cell-electrolyte interface, a circuit model composed of various elements, each representing a physical element the current is passing through, is constructed and its validity verified by fitting the model on the measured data. If the model is in accordance with the measured data, quantitative information about circuit element properties can be obtained.

The simplest description of an electrical circuit is presented by Ohm's law, which states that the potential U is proportional to the product of current I and resistance R:

$$R = \frac{U}{I} \tag{2.23}$$

The validity of this equation is limited to the ideal circuit elements which fulfil the requirement of linearity, which is in general not true for real electric systems. While linear behaviour can be assumed for electric circuits of macroscopic dimensions at moderate dc-potentials and currents, very high or low currents or solid-liquid interfaces require a more complex description. To ensure linear behaviour of the investigated system EIS is performed at low signal amplitudes, usually 1-10 mV, in order to fulfil the requirement of pseudo-linearity (Figure 2.16).

Using the relation $\omega = 2\,\pi\,f$ with the radial frequency ω in rad^{-1} and the frequency f in Hz, the description of a sinusoidal ac-potential as a function of time can be written as

$$U_t = U_0 \, \sin(\omega t) = U_0 \, e^{i\omega t} \tag{2.24}$$

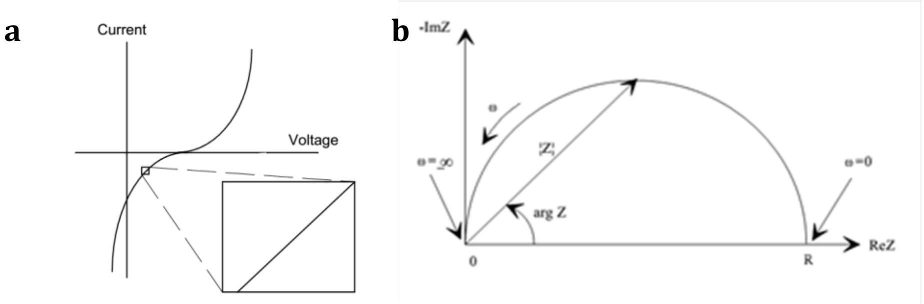

Figure 2.16 Complex Impedance in the Gaussian number plane (a) Plot of non-linear U-I-relation, inset illustrates pseudo-linear behaviour at small amplitudes; (b) representation of impedance in the complex number plane.

where $U_0$is the amplitude of the signal and U_t the potential at time t. The current can be expressed accordingly taking into account the phase shift occurring at real circuit elements:

$$I_t = I_0 \sin(\omega t + \phi) = I_0 \, e^{i\omega t - i\phi} \tag{2.25}$$

Capacities and inductivities present in the circuit induce a phase shift ϕ of the current relative to the excitation potential signal as shown in Figure 2.17. With these expressions inserted to Ohm's law, an expression for the impedance Z is obtained:

$$Z = \frac{U_t}{I_t} = \frac{U_0 \sin(\omega t)}{I_0 \sin(\omega t + \phi)} = Z_0 \frac{\sin(\omega t)}{\sin(\omega t + \phi)} \tag{2.26}$$

Using EULER's relation a the frequency dependent expression for the impedance:

$$Z(\omega) = \frac{U_t}{I_t} = \frac{U_0 \, e^{i\omega t}}{I_0 \, e^{i\omega t - i\phi}} = |Z| \cos\phi + j \sin\phi = |Z| \, e^{i\phi} \tag{2.27}$$

Complex impedance can be displayed in the Gaussian number plane and formulated as the sum of real and imaginary components:

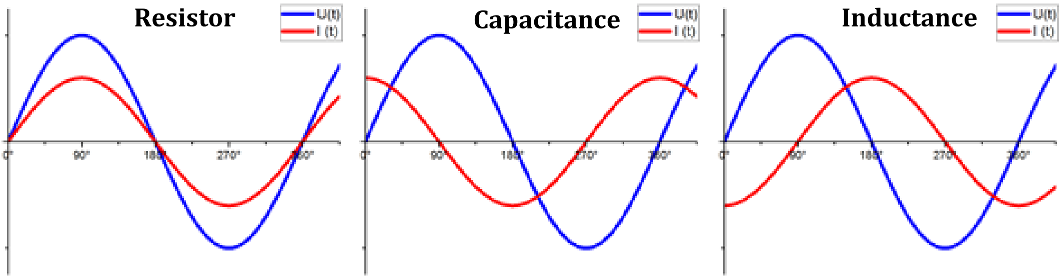

Figure 2.17 Phase shift of ac circuit elements: (left) at an ideal resistor voltage and current are in phase; (middle) capacitor current runs 90° ahead of voltage; (right) at an inductivity the current runs lags 90° behind current.

$$Z = Z' + i\,Z'' \tag{2.28}$$

The real component of the impedance Z’ identical to purely ohmic resistance, the imagery part Z’’ represents inductive and capacitive contributions to total impedance. Cartesian components Z’ and Z’’ can be transformed into their polar form using the following identities:

$$Z' = Re(Z) = |Z|\ \cos\phi \tag{2.29}$$

$$|Z| = \sqrt{Z'^2 + Z''^2} \tag{2.30}$$

$$Z'' = Im(Z) = |Z|\ \sin\phi \tag{2.31}$$

$$\phi = \tan^{-1}\left(\frac{Z''}{Z'}\right) \tag{2.32}$$

Combinations of circuit elements can be described applying the same laws as used for regular circuits: impedances in series are added up (eqn. (2.33)), parallel impedances the inverted sum of the individual contributions is calculated (eqn. (2.34)):

$$Z = Z_1 + Z_2 + Z_3 + \cdots \tag{2.33}$$

$$\frac{1}{Z} = \frac{1}{Z_1} + \frac{1}{Z_2} + \frac{1}{Z_3} + \cdots \tag{2.34}$$

Using these equations, the behaviour of arbitrary circuit models can be simulated or fitted to measurement data obtained from experiments. Modelling of equivalent circuits has to take all interfaces between separate phases in the path of the current into consideration. The most common ideal circuit elements are resistors R, capacitors C and inductors L. In case of direct current, the description of inductivities and capacities requires the consideration of changes of the potential only as the potential is turned on or off. When ac-potentials are applied to a circuit, the contributions of capacities and inductivities induce a phase shift of the resulting current relative to the excitation potential. This phase shift results from electric fields, storing or recuperating energy in electric fields at capacitors and inductors as the potential changes over time (Figure 2.17). Therefore the term of impedance is introduced, accounting for frequency-dependent electric resistance.

The voltage-current relationships various circuit elements are listed in Table 2.3. In addition to the common circuit elements resistor, capacitor and inductance, a variety of others has been developed to describe non-ideal behaviour of real systems. In this work the constant phase element and the Warburg- element shall be considered.

The constant phase element is used to describe the behaviour of “real” capacitances. The value of Y_0 has the dimension of a capacity in C and is modified by the exponent n which takes values between 0 and 1. At a value of 1 the CPE behaves like an ideal capacitor. For n = 0,5 the equation

Table 2.3 Impedance of various circuit elements for equivalent circuit modelling

Resistor	**R**	$Z_r = R$	**Constant Phase Element**	**Q**	$Z_Q = \frac{1}{Y_0(i\omega)^n}$
Capacitor	**C**	$Z_c = \frac{1}{i\omega C}$	**Infinite Warburg Element**	**W**	$Z_W = \frac{1}{Y_0\sqrt{(i\omega)}}$
Inductor	**L**	$Z_L = i\omega L$	**Finite Warburg Element**	**O**	$Z_O = \frac{1}{Y_0}\tanh\left(B\sqrt{(i\omega)}\right)$

for the CPE becomes similar to the infinite Warburg element. There is no real equivalent of the CPE, it is rather an artificial construct to describe non-ideal behaviour in measurement data resulting from effects too complex to be accounted for by theoretical mathematical description.

The Warburg-elements is used to describe diffusion at the electrodes surface. Its magnitude is frequency dependent, getting smaller towards higher frequencies. Real and imaginary contributions to the Warburg impedance are equal at all frequencies; therefore it can be easily identified by a straight line at 45° angle in the Nyquist diagram (Figure 2.18). The Infinite Warburg impedance is defined by the following equation:

$$Z_W = \frac{\sigma}{\sqrt{\omega}}(1 - i) \tag{2.35}$$

with

$$\sigma = \frac{RT}{n^2F^2A\sqrt{2}}\left(\frac{1}{c_O^*\sqrt{D_O}} + \frac{1}{c_R^*\sqrt{D_R}}\right) \tag{2.36}$$

In which σ is the Warburg coefficient which concentrates a variety of variables influencing diffusion processes. The above expression assumes an infinite thickness of the diffusion layer which is not fulfilled in many experimental circumstances. Therefore finite Warburg impedance accounts for the thickness of the diffusion layer by the factor $B = \frac{\delta}{\sqrt{D}}$ with δ being the thickness of the diffusion layer and D the diffusion coefficient:

$$Z_O = \frac{\sigma}{\sqrt{\omega}}(1 - i)\tanh\left(B\sqrt{(i\omega)}\right) \tag{2.37}$$

At high frequencies when ω→∞ or for the diffusion layer approaching infinite thickness δ→∞, the second term tanh approaches 1 and hence the finite Warburg transforms to the infinite.

$$Y_0 = \frac{1}{\sigma\sqrt{2}} \tag{2.38}$$

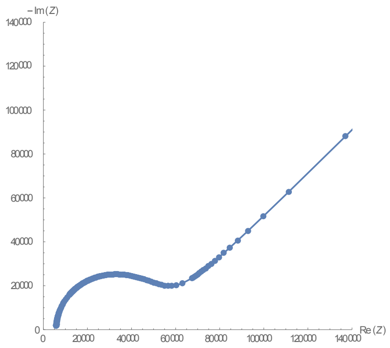

Figure 2.18 Warburg Impedance A straight line at 45° angle indicating a Warburg impedance in the observed system in correlation with the characteristic semi-circle of a RC- parallel ciruit.

Impedance data is commonly displayed in two different plots providing complementary information about the inspected system.

The most common form of presenting impedance data is the Bode plot, where the magnitude of the impedance $\underline{Z}$ and the phase ϕ are plotted versus the frequency as shown in Figure 2.19 a,b,d and e. Magnitude and Frequency are usually plotted on logarithmic scales to account for the wide range of frequency and impedance values. An ohmic resistor appears as a horizontal line in the Bode-diagram and is accompanied by a phase shift of 0°. Capacitances ca be recognized as diagonal lines in magnitude with a 90° phase shift.

Complementary to Bode-diagrams is the so called Nyquist plot, where the real part of the impedance is plotted on the x-axis and the imaginary part on the y-axis in the complex number plane. The y-axis accounting for the imaginary part is often inverted for reasons of convenience. Ohmic resistance appears as a horizontal line, capacitances and inductances as vertical lines (Figure 2.19 c). Usually both axes are plotted with identical spacing to avoid distortion. The above mentioned 45° angle indicating a Warburg-impedance is only found if both axes have the same scale This is also useful for the identification of time constants resulting from a RC-parallel-circuit which is represented by a semicircle (Figure 2.19 f). The width of the semicircle on the real axis is equal to the ohmic resistance. Several semicircles in a Nyquist-diagram indicate the number of RC- combinations present in the investigated system.

Figure 2.19 and Figure 2.20 provide an illustration of the influence of varying resistance and capacitance on the appearance of Bode- and Nyquist for simple RC-parallel and -series combinations. For both cases the resistance was kept constant while 3 different values of capacitance were simulated and vice versa. Simulations were performed using the Autolab Nova software (V1.10) also used for potentiostat control in impedance measurements and fitting of measured data.

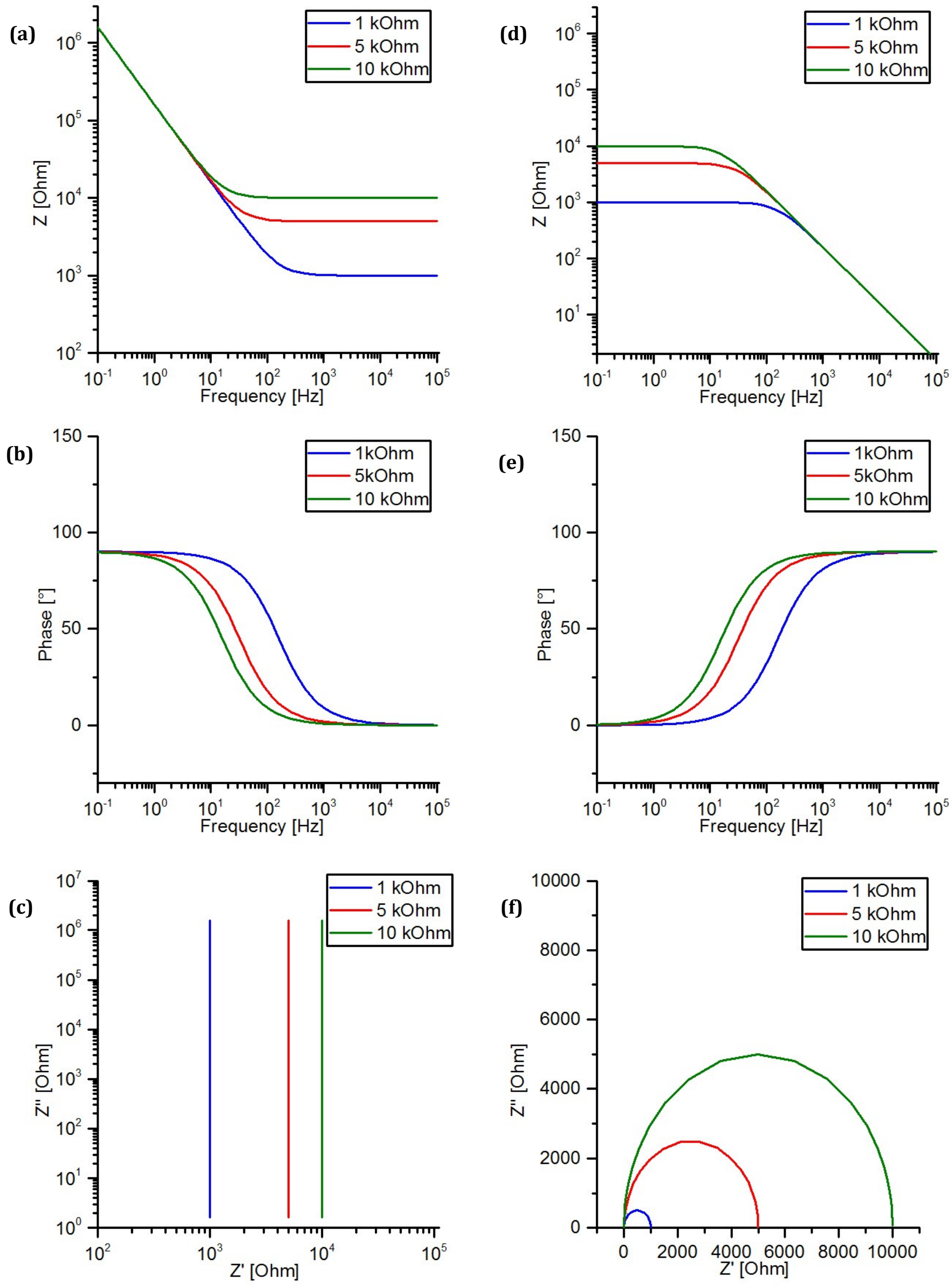

Figure 2.19 Influence of ohmic resistance on impedance for RC-series and –parallel circuits Impedance was simulated for a constant capacitor of 1 μF in series (left) and parallel (right) with resistors of 1, 5 and 10 kΩ using Autolab Nova software (V1.10). Bode plot (a) illustrates how a series resistor provides a lower limit at high frequency while increasing linearly towards lower frequencies; (b) The opposite situation is found in parallel ciruits with constant impedance at low frequency which constantly reduces towards 0 as the frequency increases; (c, d) Bode plots for phase similarly show the predominance of the capacitor at low frequencies in series and low frequency an parallel configuration;

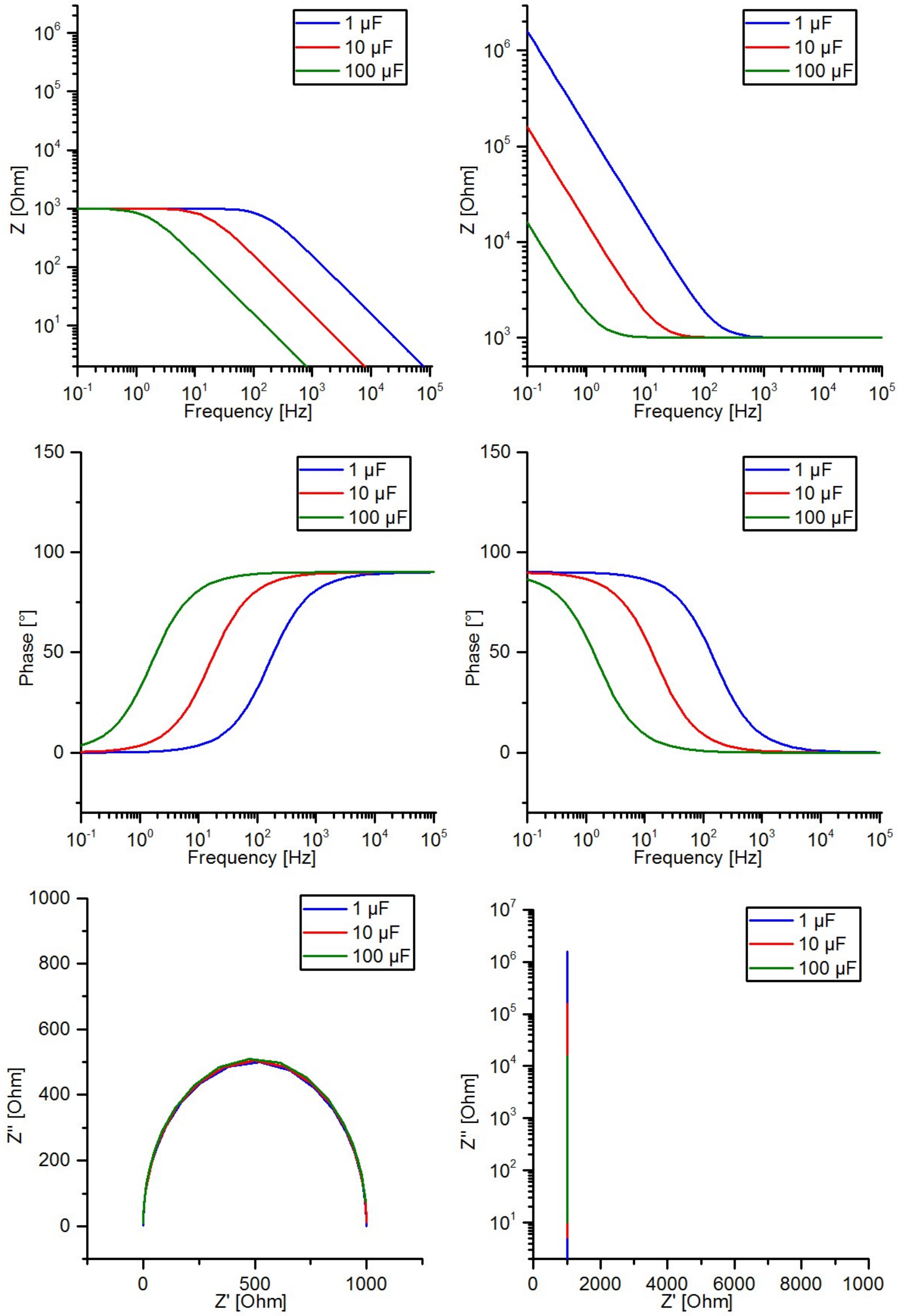

Figure 2.20 Influence of capacities on impedance for RC-series and –parallel circuits Impedance was simulated for a constant resistor of 1 kΩ in parallel (left) and series (right) with capacitors of 1, 10 and 100 µF using Autolab Nova software (V1.10).

3 Materials and Methods

3.1 Manufacturing of Gold Nanoelectrode Ensembles

Two complementary approaches were pursued for the manufacturing of gold-nanoelectrode ensembles (NEEs). The “classical” approach based on manufacturing each sample individually on 24x24 mm glass coverslips was studied and optimized in numerous details. In addition a scaled-up process for simultaneous manufacturing of multiple samples developed based on the classical approach.

The manufacturing process is summarized in Figure 3.1. Gold nanoelectrode ensembles were manufactured on glass substrates (24 x 24 mm, d = 0,15 mm (Carl Roth, Germany) or 50 x 50 mm, d = 3 mm, custom made) serving as mechanical support. These substrates were initially functionalized with a 50 nm gold layer on which the nanoelectrodes were grown. To facilitate the adhesion of gold, a 5 nm titanium layer was applied prior to gold coating. Polycarbonate membranes (ipPore™, it4ip, Belgium) of 25 µm thickness with pores of 100, 200 and 400 nm diameter served as templates for the nanoelectrodes. These membranes were also coated with

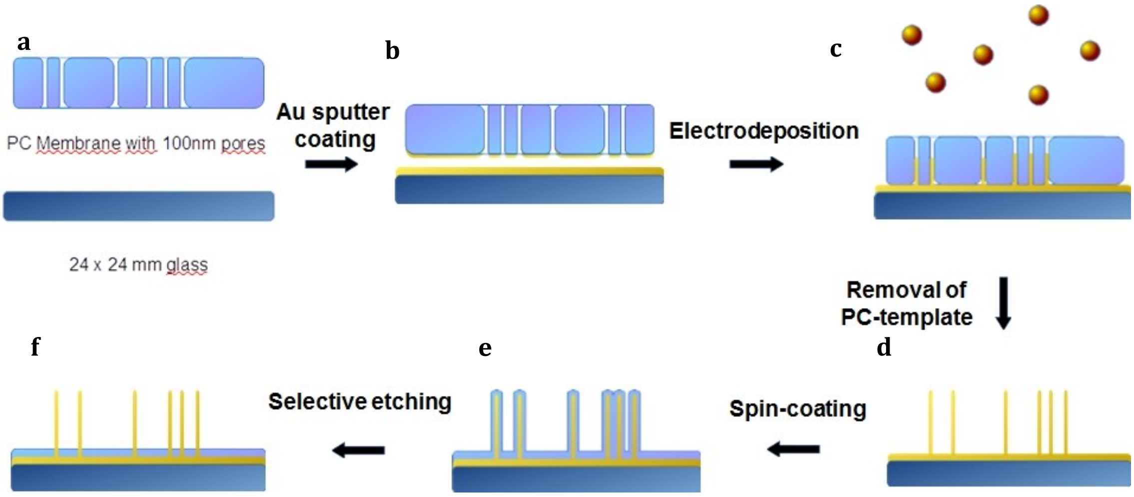

Figure 3.1 Scheme of functional nanoelectrode ensemble manufacturing ; (a) Starting materials, (b) Ti/Au coated glass and Au membrane, (c) electrodeposition into membrane pores, (d) removal of template membrane, (e) polycarbonate insulated nanoelectrode array, (f) selectively etched array ready for experiments

25 nm of gold and then attached to the gold-coated glass coverslips in a sandwich-like manner. The electrodes were then grown inside the pores at a cathodic potential of -1,5 V. After deposition the template was removed by dissolving the polycarbonate membrane in dichloromethane. Then an insulating polycarbonate layer was applied via a spin coating process and finally selective etching was performed to free the electrodes from polycarbonate while leaving the bottom insulating layer intact. The following sections will discuss the individual processing steps in detail.

3.1.1 Conventional Approach for NEE manufacturing

3.1.1.1 Cleaning of Glass Coverslips

Glass substrates of 24 x 24 mm had to be cleaned prior to metal coating to ensure good adhesion and to prevent structural defects in the metal film caused by dust particles and organic residues. Therefore glasses were placed in custom built racks made of Teflon, each holding ten coverslips. The glasses were then rinsed thoroughly with demin. water before the holder was placed in a 400 ml beaker with 150 ml isopropanol and sonicated for 10 minutes followed by rinsing with excessive amounts of demin. water. The rinsed glasses were placed in another beaker holding 250 ml of demin. water and again sonicated for another 10 minutes. After wet cleaning samples were first dried in air stream and then in an oven at 80 °C for at least 1 h before being processed in sputter coating or stored under dust protected conditions.

3.1.1.2 Sputter Coating of Titanium and Gold on Glass Coverslips

Metal thin films were manufactured by magnetron sputtering (BalTec MED010 or Leica ACE 600). Clean glass slides were placed on a custom-built plate holding ten samples which was mounted on the rotating stage of the sputter coater inside the vacuum chamber. The plate had radially aligned cavities matching the size of the glass coverslips to ensure the glasses remain centred under the sputter targets during the deposition process (Figure 3.2). Samples were constantly rotating at 15 rpm during all steps until the finished samples were taken from the chamber. Prior to coating the chamber was pumped to a base vacuum $< 5 \cdot 10^{-5}$ mbar. Once the base vacuum was reached, the pressure was adjusted to the desired values by allowing a constant flow of argon into the chamber. The coating was applied following a three-step procedure using parameters listed in Table 3.1.

The first step of titanium pre-sputtering, serving the purpose of removing oxides formed at the titanium target resulting from exposure to air is performed with the shutter closed. After this

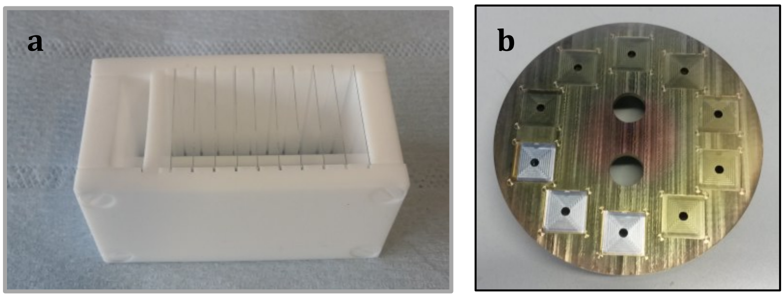

Figure 3.2 Sample holders for glass substrates (a) Teflon holder for up to ten glass substrates used for cleaning processes; (b) Plate custom built for sputtering over 24 x24 mm glasses. Ten cavities matching dimensions of the glasses are distributed around the perimeter of the plate. Their radial distance was chosen to ensure are center under the sputter target during sputtering. Holes in the center of each cavity help avoid displacement during evacuation of the process chamber. Two large holes at the center are for better handling of the plate.

step, the shutter was opened and the titanium layer was created at lower current than the previous removal of oxides. The third step creates the gold layer on top the adhesion supporting titanium film. Current and deposition time for gold were varied to evaluate influence of these parameters for ideal surface structures of the resulting gold film.

Measurement of resulting film thickness was monitored with the integrated quarz-crystal measurement system on the Leica ACE 600. Film thickness for samples prepared with the BalTek MED 010 was measured using a profilometer (DekTak). Samples were scratched using a sharp scalpel and the depth of the resulting scratches was measured on at least 5 different spots along the scratch.

Table 3.1 Parameters for glass-substrate sputtering under rotation

Step	Material	p(Ar)	Current I	Time
1	Ti (pre-sputtering)[1]	$1{,}2 \cdot 10^{-2}$ mbar	120 mA	300 s
2	Ti	$1{,}2 \cdot 10^{-2}$ mbar	60 mA	300 s
3	Au	$5 \cdot 10^{-2}$ mbar	15 -60 mA	300 – 900 s

[1] Pre-sputtering is performed with closed shutter

3.1.1.3 Sputtering of gold on polycarbonate template membranes

Coating of the template membranes was carried out on a circular plate similar to the one used for coating of glasses, but instead of cavities it was equipped with five petri dishes glued in place radially centred to match the position of the sputter targets. The sputter coater was evacuated to a base vacuum of $< 5 \cdot 10^{-5}$mbar before a pressure adjusted to a $5 \cdot 10^{-2}$mbar argon

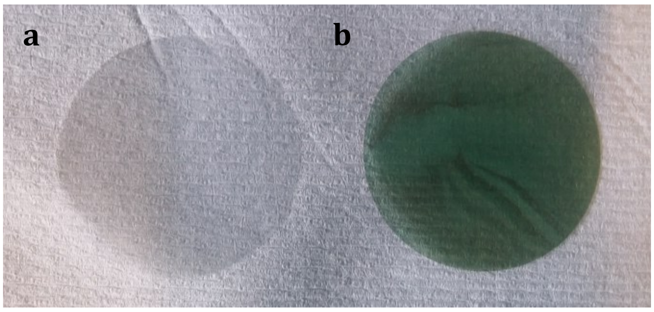

Figure 3.3 Template membrane before and after sputtering

atmosphere for gold sputtering. No sputtering of titanium is required for coating of polycarbonate surfaces. The membranes were then coated with gold at 60 mA for 180s while rotating the stage at 15 rpm during the process. The resulting gold layer has a thickness of approximately 25 nm. The coated membranes were then taken out and stored in petri dishes with the gold side up to avoid damage to the thin metal film.

3.1.1.4 Electrodeposition – Growth of Nanoelectrodes

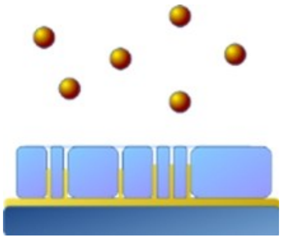

Gold coated substrate glasses were prepared for electrodeposition of the nanowires by gluing a thin strip of aluminium foil to one corner of each sample using a drop of silver ink (Sigma-Aldrich, Saint Louis, MO, USA). The aluminium strip served as electrical connection to the power supply (Figure 3.4a). After the glue has dried for at least 1 hour, a glass substrate was placed inside the cavity at the bottom plate of the deposition device (Figure 3.4b). The gold-coated template membrane was soaked in a bath of the electrolyte for 2 minutes to ensure wetting of the pores prior to attachment. The membrane had to be handled carefully with the gold coated side pointing upwards at all times to avoid damage to the gold film. After wetting, the membrane was carefully picked up using tweezers and excess electrolyte was allowed to drip off holding the membrane vertically. Then the membrane was gently rolled over the gold-coated glass so that the membrane is centred (Figure 3.4c). Inclusion of air bubbles had to be avoided as good as possible. Using a medium softness brush the membrane was carefully attached to the glass and residual air bubbles removed with gentle strokes slowly moving outwards from the centre until schlieren-lines became visible. Then the cylindrical deposition chamber was placed on the glass-membrane sandwich and pushed down, gently fitting into the braces fitted on the bottom plate where the cylinder is kept in place by three braces around the cavity (Figure 3.4). Special care had to be taken for the cylinder to be perfectly aligned, ensuring a tight seal between chamber and membrane to avoid leaking of the chamber.

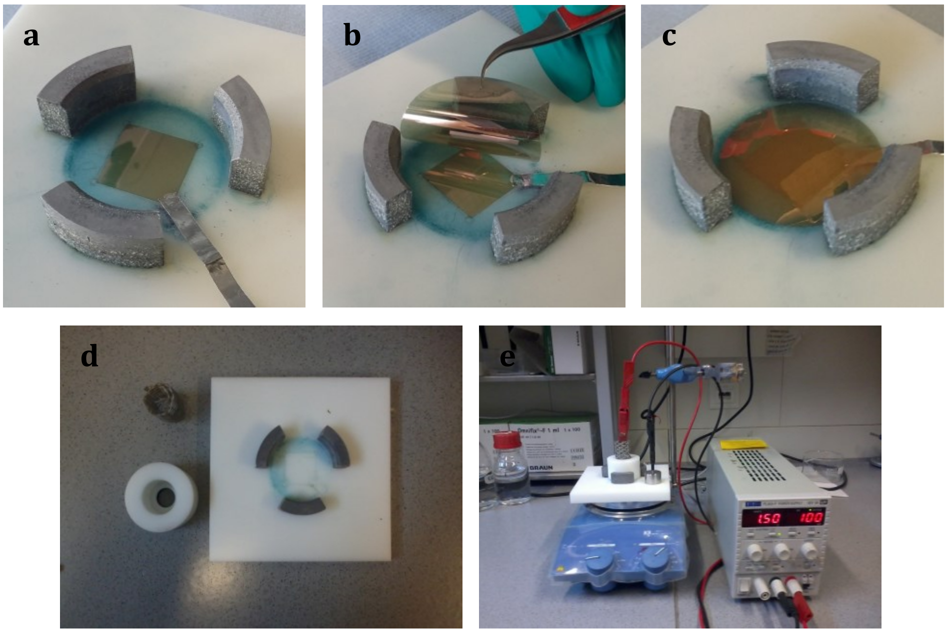

Figure 3.4 Electrodeposition setup (a) gold-coated coverslip with aluminium strip for electrical contact placed in cavity of deposition setup; (b) deposition chamber components platinum mesh electrode (top left), chamber body (bottom left), base plate (right); (c) gold-coated glass substrate with attached membrane on base plate; (d) complete chamber with closed chamber and power supply

After assembly the inner volume of the chamber was filled with 15 mL of gold-electrolyte (Conrad Elektronik, Germany) and a magnetic stirrer. To avoid contact between the stirrer and the membrane, the inside of the cylinder has two different diameters. The diameter of the lower part defines the contact-area between electrolyte and membrane surface on which electrodes were grown, the upper part was just big enough to fit the magnetic stirrer and mesh-electrode. The platinum-mesh electrode was fitted into the cylindrical opening completing the setup. Care had to be taken for the mesh not to obstruct rotation of the magnetic stirrer underneath. After turning on the stirrer, the position of the mesh-electrode was adjusted so it would sit as low as possible without interfering with the rotation of the stirrer. The aluminium stripe connecting the gold-surface and mesh electrode were then connected to the power supply with alligator clips and electrodes were grown at a potential of -1,5V while stirring at 800rpm. During deposition the resulting current was recorded for monitoring of the process using a customized LabView program. The length of the resulting electrodes was controlled by deposition time.

When the growth of the nanowires was terminated by turning off the power supply, the deposition-apparatus had to be carefully disassembled in order to recover the deposited sample. Electrodes were disconnected from the power supply, then the mesh-electrode and stirrer were removed from the electrolyte chamber. The electrolyte was carefully removed using a small pipette as good as possible while avoiding contact between pipette-tip and the surface of the template membrane. Next the cylinder had to lifted from the base plate avoiding any lateral movement as this may damage the electrodes from on gold surface. Successful growth of nanoelectrodes was visible in for of a darkened circle where the cylinder was open to the membrane surface. The 'sandwich' of glass substrate and attached template membrane was carefully removed from the base plate with tweezers, rinsed with small amounts of water to remove any salt residues and then placed on a sheet of paper to dry at air.

3.1.1.5 Removal of template membrane

After the nanoelectrodes were grown inside the pores of the membrane, the template had to be removed to obtain surfaces with free standing nanowires. This was achieved by dissolving the membrane in dichloromethane. Other solvents did either not have sufficient ability to dissolve the polycarbonate membrane or caused too much swelling of the polymer which in the worst case resulted in rupture of the nanowires. Only chloroform had the potential to dissolve the membrane in a satisfying manner, but it was not used due to its higher toxicity compared to dichloromethane.

After the deposited samples were dried at air, the parts of the membrane protruding over the edges of the glass substrate had to be removed, otherwise the samples would not fit inside a rack similar to the one used initially to clean the glasses for metal film coating. This was done by carefully cutting the membrane along the sides of the glass using sharp precision scissors. If samples were immersed in dichloromethane without removal of the protruding parts of the template, inhomogeneous swelling upon contact with the solvent would result in uncontrolled detachment of the template, rendering the samples unusable. The rack was then placed in a bath of 200ml dichloromethane inside a beaker for 2 hours. The dissolution of the membrane was indicated by schlieren lines in the solvent. When no more schlieren were visible the solvent was saturated with polycarbonate and the rack was moved to a fresh bath of dichloromethane for another 2 hours. A third bath was used to remove final residues. Finally the rack was immersed in a water bath for 10 minutes to remove any residual salts from the gold electrolyte which were insoluble in DCM.

3.1.1.6 Manufacturing the insulating polymer layer

The previously manufactured nanowire-surfaces were covered with a homogeneous layer of polycarbonate via a spin-coating process to create the functional insulation of the bottom gold layer. The spin coating solution consisted of 200 mg Bisphenol-A-polycarbonate (Sigma-Aldrich) dissolved in a

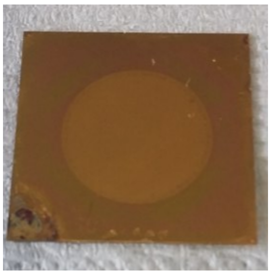

Figure 3.5 NEE on 24 mm substrate after spin-coating The area where nanowires were grown can be recognized by the turby appearance ant the centre of the substrate.

1:1 mixture of 2 ml dry Chloroform (Sigma-Aldrich) and 2 ml dry 1,2-Dichlorobenzene (Sigma-Aldrich). The mixture was prepared in a screw cap vial and shaken overnight to ensure proper dissolution.

Spin coating was performed in a two-step procedure. The samples were centred the spin-coaters stub and held in position by vacuum. At an initial speed of 500 rpm 400 µl of the polymer-solution were dispensed on the surface manually with an Eppendorf pipette. After 10 seconds he sample was then accelerated to speeds between 1200-1800 rpm for 30s to spin off the excess polymer solution and thin the film to the desired thickness. After the program has ended the samples were immediately transferred to an oven at 85°C for 1 hour to cure the polymer film.

3.1.1.7 Selective etching of the insulating layer[1]

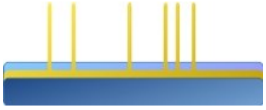

The polymer film generated by spin-coating had to be partially etched with the aim of leaving the insulating bottom layer intact whilst removing polymer residues from the vertical nanoelectrodes. Etching is usually performed during assembly of the experimental chamber before the electrodes are inserted. Therefore 1 ml of 2M NaOH was pipetted into the volume defined by the teflon ring confining the experimental chamber. Samples were etched for 30 minutes at room temperature before the solution was removed with a fine pipette tip connected to a water-jet vacuum pump. Samples were washed ten times by adding 1 ml of water with a pipette and removing the water with by vacuum suction.

---

[1] Although the etching step is performed only after the nanoelectrode-surfaces have been assembled into the experimental chambers (as described below in section 3.1.4) the process is described here to maintain the logical order of work steps.

3.1.2 Scaled-up process for NEE manufacturing

As the conventional approach for manufacturing of NEES was extremely time-consuming, a new method for large-scale manufacturing of sample surfaces was developed. Higher process efficiency was achieved by depositing on gold-coated glass substrates of 55 x 55 mm which allowed to make use of the entire surface area of the template membranes used in the process instead of restricting the deposition area with the conventional deposition chamber. The following section describes the changes that were made to the above described procedure to implement this approach.

3.1.2.1 Cleaning of large glasses

Starting material for large-scale deposition were custom made glasses of 55x55 mm obtained from the institutes glass workshop. Each glass was patterned with a wafer saw into nine squares of 15x15 mm or four squares of 20x20 mm prior to cleaning. Cuts of 0,5 mm depth were made on the backside of the glasses allowing easy separation of the glasses after deposition process and removal of the membrane (Figure 3.6). Large glass cleaning procedure was similar to the procedure used for smaller substrates. Glasses were placed in a custom rack holding up to five glasses and processed according to the previously described procedure (Chapter 3.1.1.1).

3.1.2.2 Sputter coating of large glasses

Large glasses were positioned on the substrate holder inside the process chamber ensuring their centres were aligned with the targets' centres. Coating of the glasses was performed in stationary mode or under constant rotation at 15 rpm as described in section 3.1.1.2 for smaller glasses. For stationary sputtering a single glass was centred under the titanium or gold target by manually controlled rotation of the substrate holder inside the chamber before each process was started. Stationary sputtering required shorter process times, but did not provide

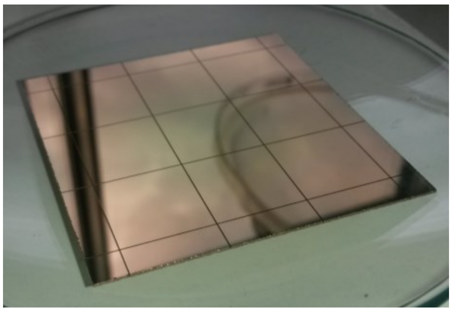

Figure 3.6 Large glass after coating with titanium and gold Gold coated substrate with groves for separation on the coated side. For better visibility the glass shown in picture was coated with gold on the groved side. In later experiments the flat side was coated instead as the groves caused problems of electrlyte leakage during the deposition process.

satisfactory results because of inhomogeneous film thickness across the surface. All process parameters are listed in table Table 3.2.

Table 3.2 Parameters for sputtering of large glass-substrate sputtering

Step	Material	p(Ar)	Current I	Time stationary	Time rotating
1	Ti (pre-sputtering)[1]	$1{,}2 \cdot 10^{-2}$ mbar	120 mA	300 s	300 s
2	Ti	$1{,}2 \cdot 10^{-2}$ mbar	60 mA	180 s	300 s
3	Au	$5 \cdot 10^{-2}$ mbar	15 -60 mA	300 s	900 s

[1] Pre-sputtering is performed with closed shutter

3.1.2.3 Growth of nanoelectrodes on large glasses

The gold-coated substrates were fixed to the bottom of a glass bowl with conducting copper tape, which also served as electrical connector to the power supply. The template membrane was soaked and attached similar to the conventional scale process. A glass cyclinder of 45 mm diameter was then glued on top of the membrane with Twinsil forming the chamber for electrolyte (Figure 3.7). A mechanical stirrer and the platinum-mesh counter-electrode were immersed into the electrolyte and the stirrer set to 400 rpm. The platinum mesh and copper tape were connected to the power supply using crocodile clamps and deposition was carried out at -1,5 V. The resulting current was recorded using the identical LabView program and the length of the electrodes controlled via the deposition time.

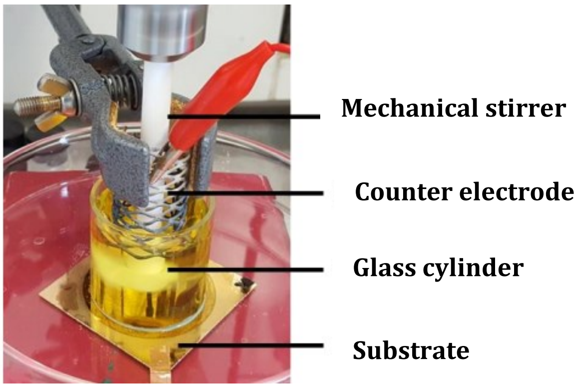

Figure 3.7 deposition setup for large substrates. The gold-coated subsrate is placed in a large petri dish and fixed to the bottom with copper tape which also served as electrical contact. A glass cylinder glued to the membrane confines the volume holding the electrolyte in which a mechanical stirrer and the platinum mesh counter-electrode are immersed.

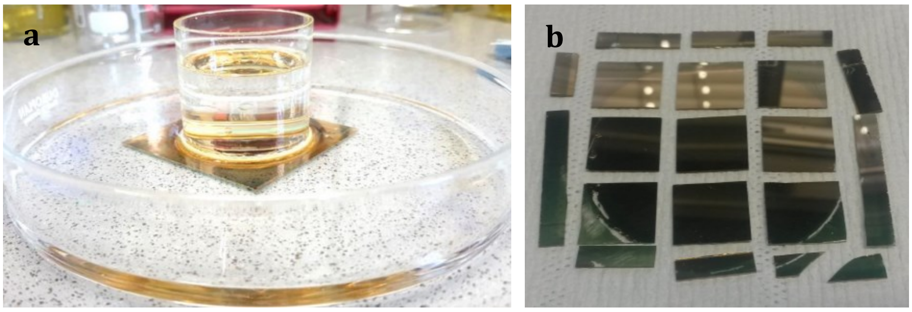

Figure 3.8 Processing of large substrates after deposition(a) large substrate with cylinder filled with dichloromethane for dissolution of the template membrane; (b) separed tiles obtained from large substrates after cleaning.

3.1.2.4 Removal of template membrane

Because the cylinder enclosing the electrolyte during deposition is glued to the membrane, it cannot be removed by immersion of the glass in a beaker of dichloromethane as the smaller samples were processed. This would cause high mechanical stress potentially damaging the nanoelectrodes resulting from shearing forces induced by the weight of the glass cylinder. Instead the electrolyte is removed from the chamber, then the surface is washed thrice with demin. H_2O before dichloromethane is filled into the cylinder. Every 30 minutes the dichloromethane is exchanged to prevent saturation. As the membrane underneath the glued area is fully dissolved, the chamber spilled its content into the dish below. At this point the glass cylinder can be removed and the glass was transferred into a beaker holding sufficient volume of dichloromethane to immerse the entire glass. After one hour the glass is removed from the dichloromethane bath and transferred into a water bath for removal of salt residues. After 1h the samples were removed from the water bath and dried at air. The dried samples were then separated along pre-patterned groves into 4 or 9 tiles of electrode deposited area (Figure 3.8).

3.1.2.5 Spin coating of separated tiles

The fragments of the large glasses were spin-coated employing the same procedure described in section 3.1.1.6. The dispensed volume was adjusted with regard to the smaller surface area of the tiles (20x20 or 15x15 mm). For 20 ml tiles 180 µl were dispensed, on 15 mm tiles only 150 µlwere sufficient to form the desired polycarbonate film. Spin speed and times remained unchanged, the bake out at 85°C for 1h as well.

3.1.2.6 Etching of spin coated samples

Etching on separated tiles of large glasses is carried out similarly as performed individually processed glasses described in section 3.1.1.7.

3.1.3 Manufacturing of Ag/AgCl reference electrodes

3.1.3.1 Silverchloride coating on wires

Reference electrodes were manufactured from 0,5 mm silver wire of 99,9% purity (Carl Roth, Germany). Silver wire was cut to pieces of ~50 mm length and initially cleaned by immersion first in isopropanol and then H_2O for 10 minutes each in a ultrasonic bath. Between cleaning steps the wires were rinsed with demin. H_2O. The wires were then coated with an AgCl-layer by electrodeposition. The silver wire and a counter electrode were immersed in a solution of 3M KCl. A coiled silver wire providing a lage surface area was used as counter electrode. A cathodic current of 0,1 mA was applied to the silver wire for 300s by a Source-Meter-Unit (Keithley 2635A, Tektronix, USA). The process was controlled and monitored by the same custom LabView program used for the deposition process. After deposition the coated wired were removed from the bath, rinsed with H_2O and dried at air.

3.1.3.2 Epoxy coating of silver wires

Pseudo reference electrodes were manufactured by coating of AgCl coated silver wires with commercially available silver ink (Basi Inc., Japan). The highly viscous ink was thoroughly mixed before coating. A pasteur pipette was immersed in the ink so a drop of ink would remain at the tip. By carefully moving the coated wire through this droplet into the inner pipette volume thin coating of the wire was achieved, as the ink is dragged towards the inside of the pipette during this process. The wire was moved in and out of the pipette a few times until a homogeneous coating was formed. Care was taken to only coat the AgCl-coated area of the pipette. The ink-coated wires were dried in an oven at 85°C for 1h.

3.1.3.3 Testing of reference electrodes

Reference electrodes were tested for their offset potential relative to a commercial Ag/AgCl electrode (Basi Inc., Japan). The electrode under test and the reference were both immersed in the same electrolyte and connected to a SMU (Keithley 2635A, USA). The OCP was measured using a custom LabView program recording the potential over time.

3.1.4 Assembly of experimental chambers

For etching and usage in experiments the spin-coated surfaces were assembled into the experimental chambers. The chambers provided mechanical support for the counter and reference electrodes and a confined volume for the electrolyte/cell culture medium used in the experiments.

Chambers were assembled using standard polycarbonate cell culture petri dishes (CellStar, Germany). Three holes were drilled through the side walls of the dishes with a bench drill (d = 1,5 mm), 90° separate from each other. Ridges were removed manually with a scalpel. The previously manufactured surfaces were placed at the centre of the petri dish and fixed to the bottom with tape on two corners. Next a custom made Teflon ring was glued on top of the NEA surface with Twinsil glue. Care had to be taken for the three holes in the ring for electrode uptake to be well aligned with the holes in the dish. This ring confines the exposed surface area of the NEE for the experiments. The cylindrical volume inside the ring holds the electrolyte solutions or cell culture medium in the following experiments.

For electrical contact to the NEA surface a copper wire (d ~ 0,1 mm, l = 50 mm) was used. Insulating material was removed at both ends and the wire was put through the one hole of the dish and fixed to the bottom so that its uninsulated end of ca. 5 mm would be superimposed to one corner of the NEA surface. A drop of conductive silver glue (Fluka, USA) was then dispensed on the corner and wire establishing electrical contact. After the glue had dried at least two hours, the etching process as described in section 3.1.1.7 was performed. Then the counter and reference electrodes were fitted through the holes on the outer petri dish and inner Teflon ring. A platinum wire was fitted across the Teflon ring through the opposing holes, the epoxy coated reference electrode was put through the third hole so its tip would stick into the centre area about 1 mm. Finally the entire petri dish except for the inner area of the Teflon ring was filled with Twinsil to protect the electrical contacts from moisture and for sealing the holes. After sterilization with 70% Ethanol and/or UV- irradiation the chambers were ready for use in cell culture experiments.

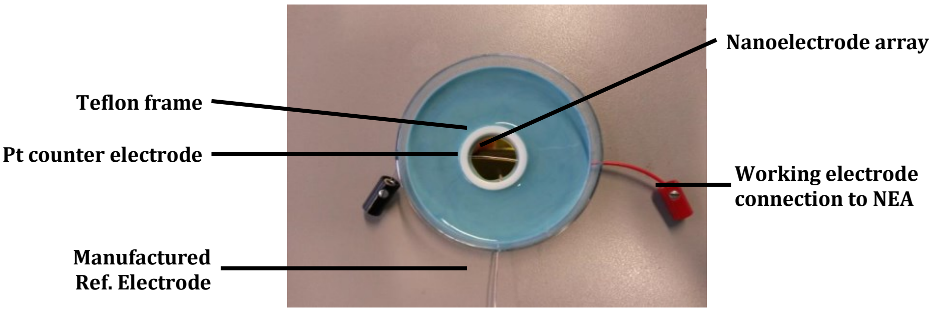

Figure 3.9 Assembled measurement chamber for NEEs NEEs are placed at the bottom of a petri dish. A Teflon ring glued to the surface confines the exposed area and bears the counter and reference electrode. A copper wire glued to the NEE with silver ink provides connection to the measurement circuitry. The area surrounding the Teflon ring is passivated with Twinsil.

3.2 Electrochemical Analysis of Nanoelectrode surfaces

Electrochemical analysis was performed using a Autolab PGSTAT302N potentiostat (Metrohm, Netherlands) controlled with Autolab NOVA (V1.10) software. Measurements were performed in a three electrode configuration using the experimental chambers described in section 3.1.4. Experimental chambers were placed inside a fume hood at ambient conditions. The electrodes were connected to the potentiostat inputs using crocodile clamps and the connecting wires were fixed with tape to avoid unintended movement of the chamber during the experiments. Then the chamber was filled with 1 ml of electrolyte solution.

3.2.1 Electrochemical Impedance Measurements

All EIS data was acquired using 0,1M NaCl solution in water. EIS spectra were measured at a fixed potential of 0V taking ten measurements per decade. Actual measurement frequencies were determined by the software according to this condition. In this work all spectra were measured from 10 kHz to 0,1 Hz at an amplitude of 10 mV RMS, which is also the standard range used in most relevant publications on this topic. Measurements at higher Frequencies often become very noisy due to shielding issues, below 0,1 Hz data acquisition becomes very time-consuming and provide little additional information, therefore they are usually abdicated. Higher signal amplitudes may be used, when the resulting currents are too small to obtain stable readings. After the experiment finished the electrolyte was removed from the chamber and it was washed at least five times with demin. water to clean it for later use.

3.2.2 Cyclic Voltammetry

For CV experiments 1ml of 0,01 M Ferricyanide (Acros, USA) in 0,1 M NaCl was filled to the experimental chamber. Measurements were taken using the linear sweep voltammetry configuration of the device. If not stated differently, sweeps were performed starting at 0 V with 0,6 V upper and -0,2 V as lower vertex points at a sweep rate of 0,1 V if not stated differently. Three consecutive sweeps were performed to confirm stability of the system. After experiments the chambers were cleaned and stored for later use.

3.3 Voltage and current measurements

After assembly and etching, the nanoelectrode surfaces are ready for measurements of electrical signals from living cells. In order to maintain cell viability, the measurement chambers needed to be set up inside a cell culture incubator (Figure 3.10). Inside the incubator an atmosphere of 5% CO2 at 37°C and saturated humidity was maintained to provide sufficient conditions for cell growth. Wires connecting the three electrodes of each chamber to the measurement devices were fed through the back port of the incubator which was sealed with a custom built, cylindrical Teflon plug. The plug itself seals the entire diameter of the port and has holes through which wires were lead. The holes were additionally sealed with Twinsil glue upon instalment. Shielded coaxial wires type RJ-174 were used to minimize electrical noise. At their ends the wires were carried plug which were used to establish electrical connection by plugging into the ferules at the chamber electrodes.

Outside the incubator all wires were connected to a matrix-switch unit which sequential measurement on up to ten channels. Each channel could be connected to either the voltage measurement system or the potentiostat for cyclic voltammetry and electrochemical impedance spectroscopy (Figure 3.10).

3.3.1 Measurement Program Layout

The electrical measurement system consisted of a source-meter-unit (SMU, Keithley 2612) which provided two independent channels for simultaneous measurement of voltage and current. Data recording, device configuration and control of the switch matrix were realized with a custom built LabView program. The program was designed to sequentially switch

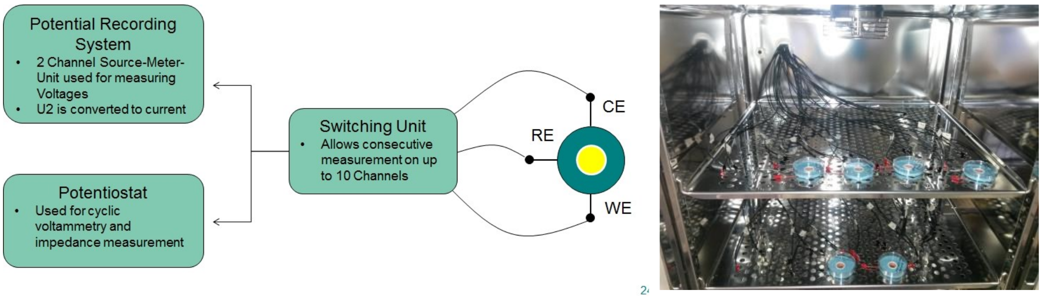

Figure 3.10 Scheme of electrical recording setup The three electrodes of the measurement chambers are connected to the matrix switch unit via RG174 shielded coaxial wires. The switch matrix selects individual samples and connects them to the voltage recording system or potentiostat. Samples prepared for measurements inside cell culture incubator. Five samples each were fitted to the upper and lower shelves of the incubator.

between the channels, taking a programmed number of measurements at one channel before switching to the next. After completing a cycle of taking a set of measurements on each channel, the program restarts at the first channel. Optionally the measurement can be interrupted after a cycle manually to take EIS of CV measurements. During this interrupt, channels can be selected manually allowing experiments with the desired chambers. The program provides full control of number of channels to be measured, number of data points on each interval and time between data points. The program automatically terminates after a number of cycles defined by the user, although theoretically recording could run endless.

3.3.2 Device Configuration

Two different configurations were used in course of experiments for this work. Of the two channels available with the SMU used in these experiments, either both were configured for voltage measurements or one was used for current and the other for voltage. The first channel was always used to measure the potential between the reference- and working-electrode. The second channel was either connected in parallel to a load resistor (hence the current could be calculated from the known value of the resistor) or it was wired in series with the resistor for current measurements (Figure 3.11). The latter configuration was considered to be the better one, but could only be realized after purchase of additional circuit boards for the switch matrix. The reconfiguration of the setup for direct current measurements also included reorganization of switch matrix wiring and reprogramming of the LabView routines adapting to the new wiring situation.

3.3.3 Voltage Measurement Configuration

As suggested by the manufacturer the voltage measurements with the respective channel configured to act as current source at 0 A. Source-range and -limit were set to lowest value available to minimize fluctuations. Measurement range was set to ±200 mV as cellular signals should not exceed this value allowing for highest precision of values acquired. For current measurements the device was configured to act as voltage source at 0V potential with current measurement range and limit set to 100 nA.

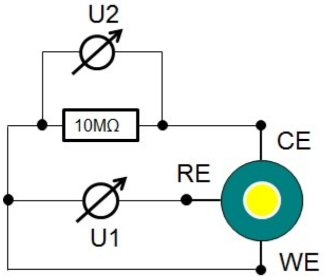

Figure 3.11 Circuit for electrical recording Experiments were performed using a three-electrode configuration. U_1 measured the potential between the reference- (RE) and working-electrode (WE), U_2 measured the potential at a 10 MΩ shunt-resistor inserted between counter- (CE) and working-electrode which was then converted into the corresponding current.

3.3.4 Measurement Speed

Settings affecting measurement speed were chosen considering aspects of precision and required acquisition speed. For long-term-experiments the data acquisition rate was commonly set to 1 Hz, therefore all settings for these experiments were chosen under the premise of maximum precision. As high precision measurements require considerable acquisition times, these settings could not be used.

Measurement speed is limited by the configuration settings of the SMU, as a rather high NPLC (Number of power line cycles) value of 10 was chosen to minimize background noise originating from power supply lines. NPLC defines the integration time of the ADC converter acquiring the measurement signal. As the power line frequency is 50 Hz, NPLC =1 corresponds to 20 ms, a value of NPLC=5 to 100 ms. The operating speed of the ADC converter provides a lower limit for data acquisition. If higher acquisition speeds were desired, the NPLC value had to be lowered for the ADC to keep up with requested measurements. As a value of 5NPLC is a rather conservative choice no significant change in noise was observed upon slight reduction of the NPLC.

Yet in order to perform high-speed measurements at intervals of 1 ms (and faster) the NPLC required to be set to 0,05 or below. The lowest possible value is 0,001 corresponding to 0,02 ms integration time, but the trade-off for fast integration is a significant increase in noise. Another problem performing high-speed data acquisition is the communication speed between measurement device and control computer. While at slower speeds data can be read as acquired, high speeds require use of internal buffers at the acquisition hardware. Acquisition time for high-speed measurements was therefore limited by the size of these buffers allowing only 50 s of recording at 1ms or 5 seconds at 0,1 ms acquisition speed. Data could only be read from the buffers after high-speed measurements had finished. Simultaneous data readout at high-acquisition speeds would require excessive additional programming and was therefore not pursued in the course of this work.

Preparation of experimental chambers for voltage measurements with cells

After assembly the experimental chambers holding the nanoelectrode surfaces needed to be introduced to a sterile environment before incubating them with cells. Sterilization was achieved by spraying and rinsing of all chamber components including plugs, wires and lids with excessive amounts of 70% Ethanol. While still wet the chambers were transferred to a sterile workbench and allowed to dry in the stream of air. To remove any residues of the ethanol-water mixture, the inner chambers were washed with sterile filtered water and dried in air stream again. Final step of the sterilization procedure was UV irradiation for 1h inside the sterile workbench.

To facilitate ideal cell adhesion the surfaces were coated with poly-L-lysin (PLL, Gibco, USA). To apply the coating, 1 ml of sterile cell culture-grade PLL-solution was pipetted on each surface and allowed to sit for one hour, then the solution was sucked off with a fine filter tip hooked up to a vacuum suction system. The surface was gently rinsed thrice by gently pipetting of sterile water ab subsequent removal with the vacuum suction. After these steps the chambers could be filled with cell culture media and transferred to the experimental incubator. Inside the incubator, electrodes were connected to the wires of the switch matrix. After configuration of the measurement program experiments could be started.

3.4 Cell culture

All experiments presented in this work were conducted with normal rat kidney cells of fibroblast type (NRK-49F, Sigma Aldrich). Cells were continuously cultured using standard cell culture protocols. Work was performed in protected atmosphere inside a sterile workbench. All materials and aqueous solutions and were obtained in sterile cell culture grade. Cell culture medium and phosphate buffered saline solution (PBS) were additionally sterile filtered through 0,2 µm pore filters. Live cells were cultured in Dulbeccos Modified Eagle Medium (DMEM) supplemented with 4% Glutamax™, 1% Pyruvate, 4,5 g l^{-1} Glucose and 10% fetal bovine serum (FBS). All components except FBS were already contained in DMEM when purchased. During incubation cells were kept inside a cell culture incubator at 37°C with 5% CO_2 atmosphere and saturated humidity.

Cells were grown inside T-25, T75 and T-175 cell culture flasks for adherent cells. The size of the flasks was chosen relating to the number of cells required for planned experiments.

3.4.1 Passaging of Cells

When cells reached 70-80% confluency, they were passaged and split to fresh flasks. After removal of used cell culture medium, adherent cells were first rinsed twice with 15 ml PBS and then incubated at 37°C with 1 mL of 0.25% trypsin in EDTA solution for 10 minutes. After incubation equal volumes of DMEM were added to the flask, then liquid containing the detached cells was transferred to a 15 ml falcon tube. Centrifugation of the falcon tube at 125 g for 5 minutes resulted in formation of a cell-pellet at the bottom of the tube. The supernatant liquid was removed and the pellet was re-suspended in 1 ml of DMEM with a 1ml Eppendorf pipette. Depending on the expected number of cells in suspension additional DMEM was added for dilution prior to counting in the coulter counter. This was necessary because the counter only yields reliable results if the concentration is not too high. For counting 100 µl of the cell suspension were transferred into special containers for the counter and diluted to a volume of 10 ml. After counting desired numbers of cells were either transferred to fresh cell culture bottles for further incubation or used in experiments.

3.4.2 Freezing of Cells

For long-term storage cells were suspended in a mixture of 95% DMEM with 5% DMSO in appropriate cry-vials of 2 ml volume. After regular washing with PBS, trypsination and centrifugation, cells were suspended in this mixture and their concentration was adjusted to 250k cells ml^{-1}. Each cryo-vial was filled with 1 ml of the cell-suspension. The filled cryo-vials were placed inside a freezing container filled with isopropanol and placed inside a -80 °C freezer. The isopropanol-filled container ensured a constant cooling-rate of ~1 °C h^{-1}. Cells were kept at -80 °C before being transferred to a liquid nitrogen tank for long-term storage.

3.4.3 Thawing of cells

Frozen cells were removed from the liquid nitrogen tank and rapidly thawed by immersion in a water bath at 37 °C while being constantly stirred. The cell-containing cryo-vial was transferred to a sterile work-bench and cells were transferred from the vial to a 15 ml falcon tube. Then 5 ml of DMEM with FBS at 37 °C were added slowly to the falcon tube. After centrifugation at 125 g the supernatant was removed and the obtained pellet of cells at the bottom of the falcon tube resuspended in 1 ml of DMEM. The resuspended cells were transferred to a T-25 cell culture flask and DMEM was added for a total volume of 5 ml. After 24 h the cells were passaged and transferred to a fresh flask. Cells from this or subsequent generations were used in experiments with NEEs.

4 Results and Discussion

4.1 Manufacturing of nanoelectrode arrays

First work on the manufacturing procedure for gold nanoelectrode ensembles was performed by Sauter, Schneckenburger and Seifert [76-79]. Yet many details of the manufacturing process remained unclear and the yield of the surface manufacturing process was very low. Low yield in this context means that numerous surfaces manufactured according to this protocol showed no or only inhomogeneous coverage of the deposited surface with the desired nanoelectrodes. In addition many samples were subject to formation of gas bubbles during electrodeposition, leading to detachment of the metal film and rendering fabricated samples unusable. Therefore a detailed investigation of all manufacturing steps was conducted and will be described in the following sections. The aim was, to establish an improved protocol for reliable and efficient manufacturing of NEE surfaces in larger numbers. In addition, a novel, scaled up process was developed allowing for the manufacturing of several surfaces in just one deposition step.

4.1.1 Cleaning of Glasses

Prerequisite for the successful manufacturing of NEEs was the fabrication of thin gold films on glass coverslips, which serve as substrates for the functional surfaces in this work. Glass coverslips need to be free of any particles or organic residues which would obstruct ideal adhesion of the metal thin films to be applied on the substrates via sputter coating. The previously employed method using caroic acid for cleaning of glass coverslips was discontinued in favour of a less hazardous procedure. A sequence of rinsing and sonication in demin. water and isopropanol was found to provide sufficiently clean surfaces. Substrates processed as described in section 3.1.1.1 yielded satisfactory results in all following processing steps and exhibited no problems of insufficient adhesion of the thin films during electrodeposition and removal of the membrane. It may therefore be assumed, that alterations of the chemical composition of the glass surface resulting from oxidation during the exposition to caroic acid have no influence on the adhesion of the sputtered titanium and gold layers. Additional

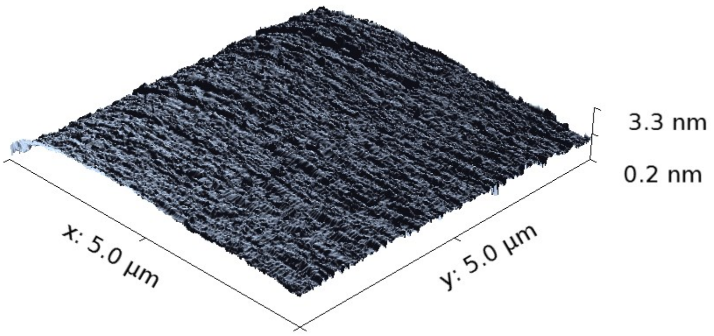

Figure 4.1AFM of glass after cleaning Glasses substrates showed hardly any roughness. Average roughness R_a for all samples tested was below 1 nm.

treatment of the glasses in oxygen plasma was considered an option but not found to be necessary for the same reason.

Since it was found that the surface structure of the gold film was of high importance for successful growth of nanoelectrodes (see below), the glasses used as substrates for the functional surfaces were checked with atomic force microscopy. In case of increased surface roughness of the substrate, this may influence on the deposited metal thin films and should therefore be excluded. Glass surfaces were mapped and average roughness was determined from the data obtained. Data obtained from these experiments showed no structural defects of any kind, hence an influence on the surface structure of the metal films was excluded. Except for minor structural defects on individual substrates which could not be detected by inspection with the naked eye, the glasses were considered perfectly suitable for use as substrates for the NEEs.

4.1.2 Sputtering of Titanium Thin Films

Before nanoelectrodes could be grown on the substrate glasses, a conductive metal film had to be deposited on the glass coverslips. Gold was chosen for this purpose, because it can be easily processed in sputtering and electrodeposition, has excellent electric conductivity and is biocompatible. Since the adhesion of gold on glass is insufficient, an additional metal layer facilitating the adhesion of gold required was required. Titanium or chromium are commonly used for this purpose [80]. In this work titanium was chosen to avoid adverse effects of chromium leakage into the cell culture medium in case of structural defects in the metal film and/or insulating layer. Although diffusion of titanium in thin gold films is documented as well, it has no significant impact on samples prepared in this work as the diffusion is very slow and only occurs at temperatures >200°C [81]. If the adhesive layer would come into contact with cell culture medium in later experiments, the adverse effects of dissolved titanium would be far less compared to the impact highly toxic chromium species.

As briefly mentioned in the introduction, the previously established procedure for titanium/gold coating of glass coverslips had to be revised as problems with detaching of the metal films and bubble formation prevailed in the following manufacturing steps, especially during electrodeposition and removal of the template membrane. In early stages of this work, problems with the adhesion of sputtered thin gold films and the reproducibility of electrode growth on the prepared surfaces repeatedly occurred. Therefore a closer investigation of both, titanium and gold sputtering processes was conducted.

Insufficient adhesion was in most cases accompanied by formation of air bubbles which were observed after the electrodeposition on the template membranes. Upon removal from the deposition chamber, few to numerous bubbles could be observed on parts or the entire surface. Number and distribution of the bubbles appeared to be entirely random, ranging from few bubbles of different sizes of up to several millimetres in diameter to numerous small ones covering the entire surface. Inspection with the naked eye of these phenomena revealed, that the bubbles actually resided between the glass coverslip and the sputtered gold film. If allowed some time for relaxation, the bubbles would eventually vanish, likely by diffusion of the included gas through the metal film. It is assumed that the evolution of molecular hydrogen is contained in these bubbles, as the reductive potential at the cathode during electrodeposition is well beyond the water splitting limit. The sites of the bubbles could be recognized as circular patterns on the surfaces even after the gas has diffused out. Upon removal of the template membrane in dichloromethane, the gold film would detach in these sites, eventually tearing even larger areas from the surface, rendering these samples unusable for further experiments. It should be noted though, that even at bubble-sites growth of nanoelectrodes was observed, and therefore no connection between insufficient growth and lack of adhesion was found here.

The old protocol for titanium sputtering suggested pre-sputtering the target with the shutter closed for 60 s with a current of 60 mA at a pressure of $1{,}2 \cdot 10^{-2}$ mbar. As the above mentioned problems of bad adhesion prevailed, the hypothesis of a dysfunctional titanium layer being the cause for this was tested. A systematic evaluation of was enabled with a new sputter coater (Leica ACE600) becoming available, which allowed monitoring of film thickness during sputter deposition. First observations revealed an increased titanium deposition rate, when titanium was sputtered in repeated processes within a short period of time. This was taken as an indication, that during repeated processes, the target's structure was altered, most likely due to a deteriorating oxide layer at the target's surface. As a consequence it was concluded, that titanium films sputtered under these conditions were of dissimilar composition. Therefore very

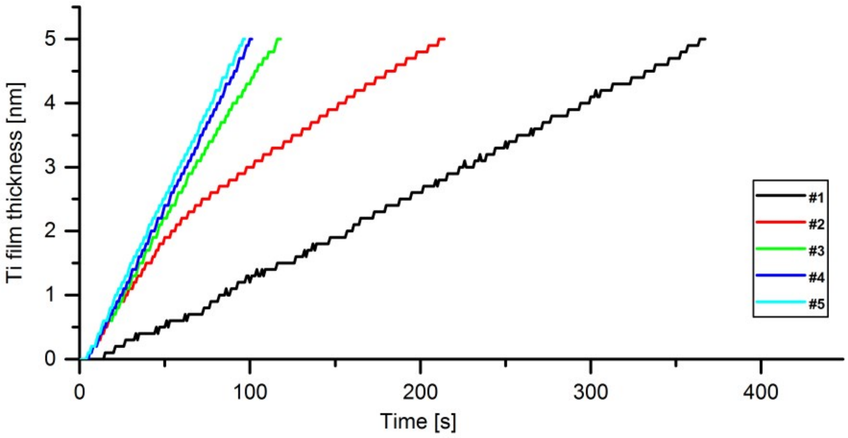

Figure 4.2 Effect of pre-sputtering on titanium deposition rate Titanium film thickness was monitored during deposition of a 5 nm layer after 300 s of pre-sputtering at 120 mA. The procedure was repeated several times until a steady deposition rate was observed. After the fourth run equaling a total of 1200 s pre-sputtering a steady deposition rate was observed. The deposition shows a step like beavior as the resolution of film thickness measurement is limited to 0,1 nm.

harsh conditions were chosen to remove the oxide layer. The pre-sputtering time was extended to 300 s and the current increased to 120 mA before a layer of 5 nm Ti was coated at 60 mA. The pressure was not altered. To verify the effectivity of these changes, repeated processes were run without venting the chamber in between steps to avoid reoxidation of the target. The target was pre-sputtered for 300s before opening of the shutter and coating of 5 nm titanium. It was observed, that the deposition rate increased with each run (Figure 4.2). After the fourth cycle only miniscule changes of the deposition rate were observed corresponding to a total of 900 s pre-sputtering being required before a reproducible deposition rate was observed. Therefore it must be assumed, that surfaces produced according to the old protocol were subject to irregular coating solemnly depending on the state of the target at the time of the experiment.

For closer evaluation of the effect of extensive pre-sputtering, the target was examined with electron dispersive spectroscopy (EDS) and electron microscopy. Unfortunately EDS data did not provide useful results, because the titanium L_α line at 0,395 keV overlaps with oxygen's K_α at 0,525 keV forming one broad overlapping peak (Figure 4.3). Even if present, the intensity of the oxygen signal resulting from a passivation layer of only few nanometres thickness on top a bulk titanium body is likely so small, that it would likely not be detectable with this method. Other spectroscopic techniques capable of the detection of Auger-electrons may be capable of providing more information regarding the composition of the targets surface but were not pursued as this aspect was considered less important.

The SEM images reveal a drastic change in surface morphology of the titanium target after the

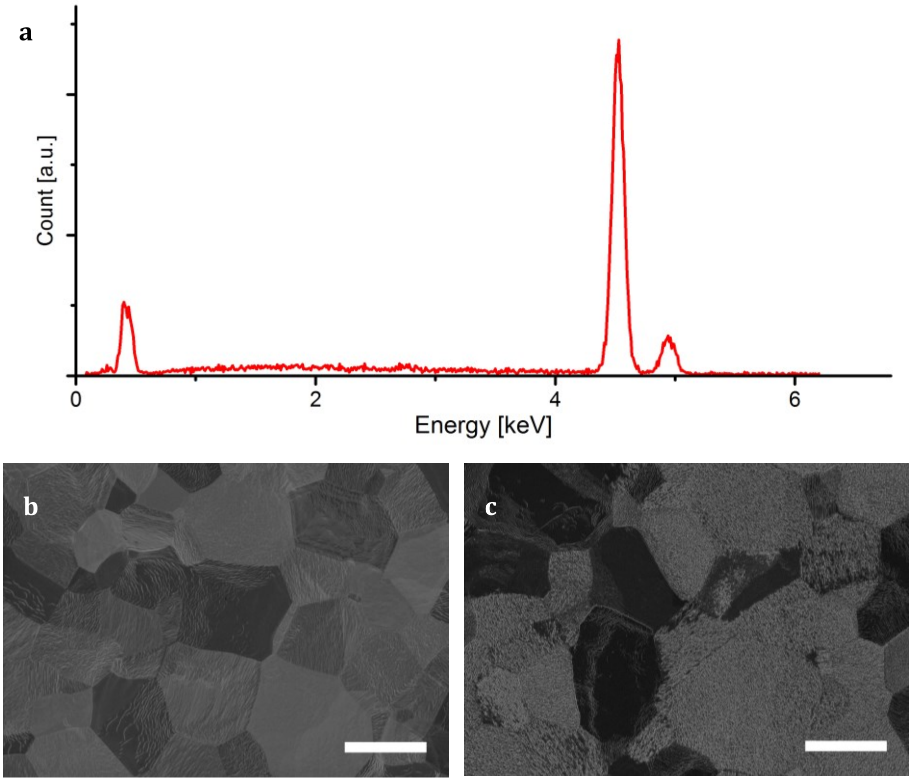

Figure 4.3 SEM images of the titanium target before and after pre-sputtering (a) EDS spectra detected from the titanium target before pre-sputtering. The presence of titanium is indicated by the presence of the characteristic lines Kα1 at 4,512, Kβ1 at 4,933 and Lα1 at 0,452. No presence of oxygen is indicated by the spectrum. Images of 1 kx magnification taken before (b) and after 900 s (c) of pre-sputtering at 120 mA (p = 1,2x10-2 mbar). Scale bars are 20 µm.

pre-sputtering was applied. Imaging of the titanium target at higher resolution than depicted in Figure 4.3 (1 kx) was not possible because of heavy charging effects, which are likely to be caused by the dielectric characteristics of the TiO_2 passivation layer on top of the target. After the pre-sputtering the surface shows clear sign of material ablation and appears to be a lot rougher. SEM imaging of the titanium layer on glass could not be conducted, because the film was too thin for imaging without most severe charging effects from the glass underneath. Attempts for imaging at very low acceleration voltages were not capable to provide the required resolution while still showing charging artefacts.

Further a change in the colour of the plasma burning under the target was observed within a few minutes after initiation of the pre-sputtering process (Figure 4.4). A similar change in the colour of the plasma was observed when gold was sputtered, but here it would take only few seconds until the reported colour change was observed. Likely because oxygen adsorbed to the targets surface is removed in the first seconds of the process.

Figure 4.4 Plasma color change during sputtering Plasma under the titanium target immidiatly after ignition and after a few minutes of sputtering at 120 mA.

Based on these findings titanium sputtering procedures were modified. By standard, titanium was pre-sputtered for 900 s at 120 mA before each process to ensure proper conditioning of the target. When more samples were prepared in sequence only 300 s of pre-sputtering were used to compensate for effects caused by exposure of the target to air when the process chamber was opened for loading of new substrates. This measure proved to be very successful as the problem of detaching gold surfaces was successfully eliminated after implementation of these changes in the process. Samples sputtered with 5 nm titanium could not be imaged successfully in the SEM as severe charging occurred.

4.1.3 Manufacturing of Gold Thin Film Electrodes

4.1.3.1 Sputtering of Thin Gold films

Thin gold films were prepared in succession to titanium coating on the same machine without venting the process chamber between steps to avoid possible oxidation. While titanium is only required to facilitate the adhesion of gold, this layer is a key component of the electrode ensemble. It serves as electrical connector for shuttling electrical current from the power supply to the growth sites of the nanowires during the following electrodeposition step and connects the wires to the measurement circuitry when the NEEs are used in experiments.

To provide sufficient electrical conductivity, a minimum thickness of 25 nm is required for the gold film [81]. At lower thickness only percolating islands of gold may be formed which do not provide required electrical properties [82]. A thickness of 50 nm gold was therefore specified in previous descriptions and also maintained in this work. Gold is not prone to oxidation like titanium due to its noble metal properties, therefore the formation of oxygen-species at the target's surface must not be expected and hence no pre-sputtering should be required. To confirm this hypothesis, the deposition-rate of gold was monitored for several consecutive

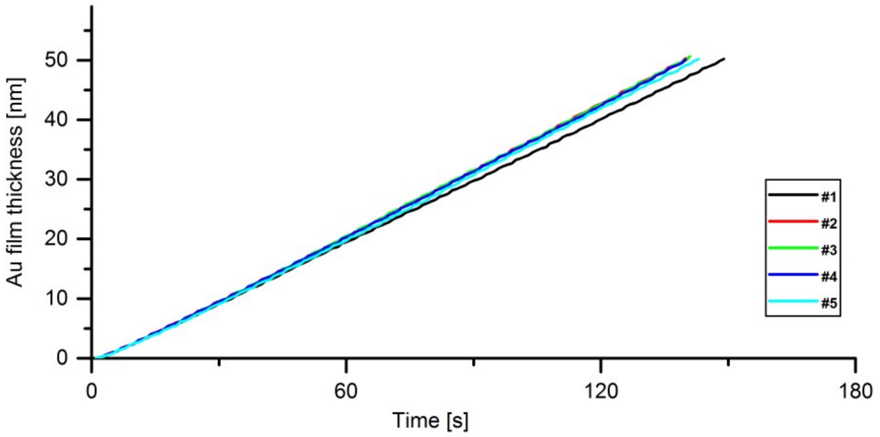

Figure 4.6 Sputterning of Gold .Comparison of growth rates for Au at 60 mA. Several processes were run in sequential arrangement to test for deviations. Only the first run shows slightly reduced depostion rate.

processes which were performed in direct succession; results are shown in Figure 4.6. Only the first process shows a slightly decreased deposition rate, while during all following processes no differences could be observed. Yet the difference is very small compared to the increased sputtering rate achieved for titanium as described in the previous section. The difference between the first and following runs was so small, that from these findings it was not considered necessary to take measures of pre-sputtering for the manufacturing of gold thin films.

Another issue obstructing efficient preparation of NEEs was the prevailing problem of inhomogeneous electrode growth on the gold surfaces. Many samples would show only sparse growth of nanoelectrodes, often clustered in small regions of the surface, or no electrodes at all.

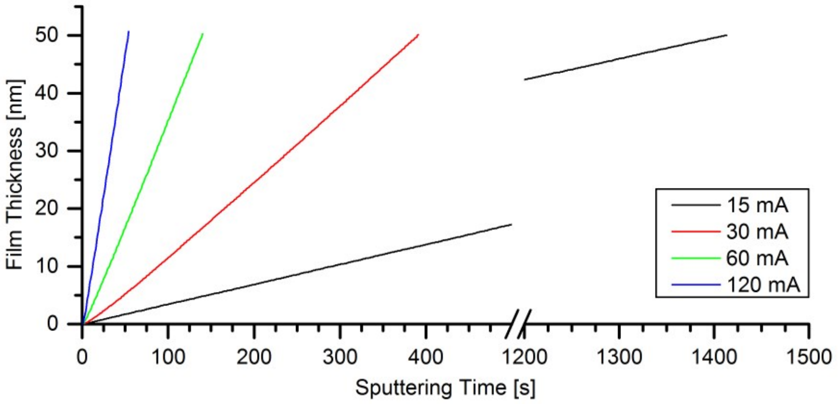

Figure 4.5 Deposition rates of gold at different sputtering currents Processing time for deposition of 50 nm of gold increased as the current was lowered. At 30 mA samples could still be prepared within moderate times, while at 15 mA the required deposition increased almost by a factor of four.

To address this problem the fine structure of sputtered gold films was examined. The structure and hence the properties of sputtered gold thin films are very sensitive with respect to process parameters such as pressure, current, etc. [83].

Therefore samples of 50 nm thickness were prepared, sputtered at different currents between 15 – 120 mA. The films prepared at different currents exhibited different reflective properties visible to the naked eye. Samples prepared at lower currents appeared rather dark, less reflective and more greenish in colour. Higher currents yielded shinier, golden surfaces. Significant differences in the resulting morphology were confirmed by SEM imaging (Figure 4.7). Gold films sputtered at lower currents yielded more inhomogeneous structures consisting of cracks in between islands of gold. Interestingly, samples prepared at 30 mA show more and larger voids at higher density compared to samples prepared at 15 mA. Such structures are described as percolating films and can have significantly different structural and electronic properties compared to regular polycrystalline thin films [84]. Higher currents resulted in more homogeneous surfaces. It could not be resolved whether these cracks reach to the bottom of the film or are rather parts of a sponge-like structure appearing at the surface, as examination by SEM could not provide sufficient insight in the gaps.

Attempts to study the depth of the gaps by AFM were also not successful because the tip diameter is too big. Nevertheless vast differences of the surface structure of the sputtered gold were revealed by AFM (Figure 4.8). Higher currents yielded surfaces with fine grain structure, while at lower currents the presence of extended hills and groves was revealed by AFM.

Measurements of the sheet resistance for the gold films sputtered at different current showed no significant differences with values ranging between 1-3 Ω cm^{-2}. Deviations observed

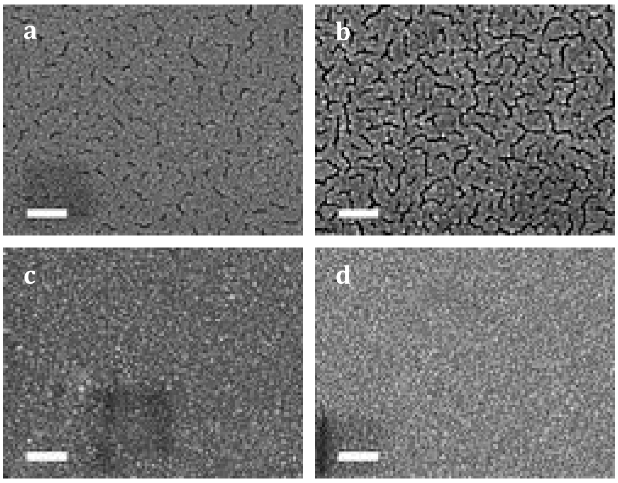

Figure 4.7 Fine structure of sputtered gold surfaces Samples sputtered with 5 nm Ti and 50 nm Au were prepared with gold sputtered at different currents: (a) 15 mA, (b) 30 mA, (c) 60 mA and (d) 120 mA on glass. Scale bars are 200 nm.

between similar samples were not larger than in comparison to other samples of different surface structure and can most likely be assigned to the limits of precession for equipment used in these tests.

After the discovery of these differences in surface morphology, a decided investigation of their influence was made to determine their influence on the growth of nanoelectrodes. Electrode growth was carried out most successfully with gold films sputtered at 15 and 30 mA while the surfaces prepared at higher currents showed hardly any nanoelectrodes. Likely the inhomogeneous surface structure of thin films prepared at lower currents offers more sites where crystallization can be initiated. Although this finding is rather empirically, it nevertheless proved to be correct for prediction of nanoelectrode growth success. An in-depth investigation of crystallization processes at the gold surfaces was beyond the scope of this work and was therefore not pursued. Based on these findings the standard procedure for the preparation of gold coated substrates was adjusted to use surfaces prepared at 30 mA. Sputtering at only 15 mA required excessive process times which caused problems of overheating targets and was therefore not continued (Figure 4.5).

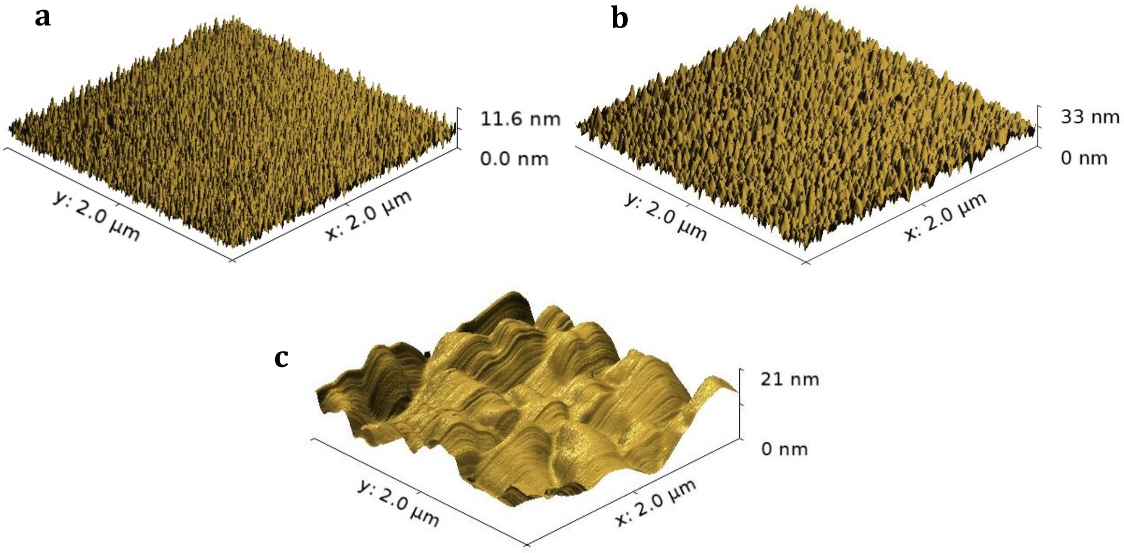

Figure 4.8 AFM of gold after sputtering at different currents Sputtering of gold yields different surface structures depending on the current. Higher currents like (a) 120 mA (b) and 60 mA yield more homogeneous fine structures compared to (c) 30 mA sputtered surfaces.

4.1.3.2 Sputtering of larger glasses

The methods and experiments discussed in the previous sections were all related to the preparation of small glasses of 24 x 24 mm. While findings related the sputtering conditions and surface structures can be applied to larger glasses as well, their dimensions have to be taken into consideration as they exceeded the size of the sputtering target. Although material deposition in sputtering pressure ranges used in this work is mostly governed by diffusion, the thickness of the deposited film varies with distance and incident angle of the substrate relative to the sputter target. While for smaller glasses the deviations are rather negligible, in course of the development of a large scale deposition process this issue needed to be addressed. Large glasses were coated with identical process parameters as the smaller ones, but two different modes, stationary and rotating sputtering were tested.

As shown in Figure 4.9, the surfaces sputtered in stationary mode show a strong decrease in film thickness, spreading out radially from the centre of the coated surface. The example presented in this Figure was intentionally coated with larger thickness than normally used. Film thickness in the corners of the square area investigated was only half the thickness compared to the centre. This difference was already apparent by visual examination of the samples as the difference in thickness could be recognized from circular areas of different reflective properties showing different colours. In contrast surfaces coated under rotation exhibit much smaller

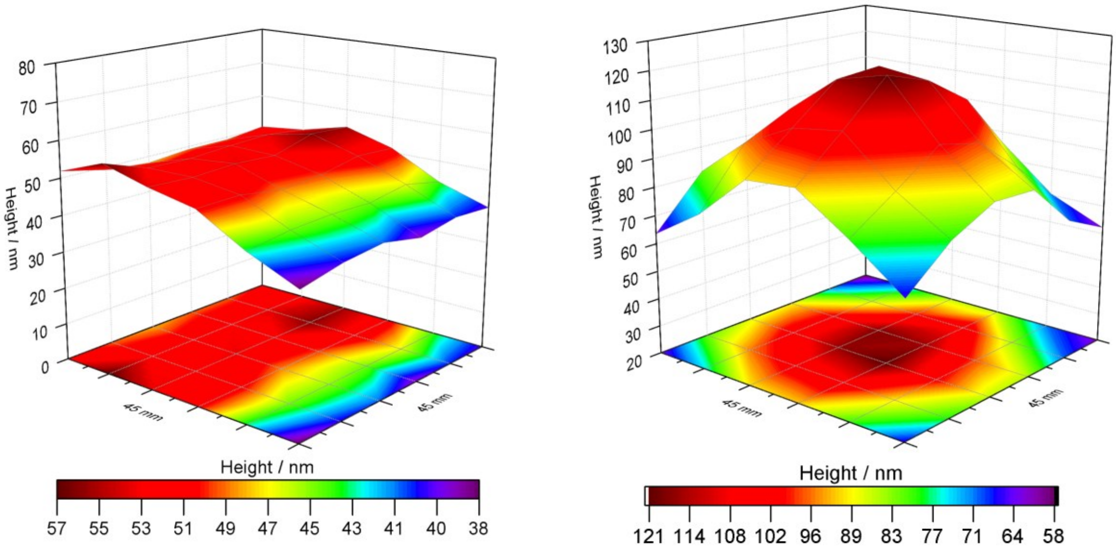

Figure 4.9 Thickness of gold sputtered in stationary and rotational mode on large glasses Thickness of gold sputtered on large glasses was measured at numerous according to a square grid projected on the glass surface. Images show 2D- and 3D-projection of the height measured for different modes of sputtering. Samples prepared while rotating the stage only have a gradient in direction of the radius of the rotational axis of the sample holder while samples prepared without rotation exhibit radially symmetric decrease of the film thickness of higher magnitude.

differences in film thickness, which in addition only occur along a linear dimensional gradient. Based on these findings the surfaces sputtered in rotating mode were considered more suitable for future experiments.

4.1.3.3 Electrical Conductivity of sputtered gold films

After the discovery of variations in morphology, samples of different surface structure were tested for their electric conductivity, because the sheet resistance may be increased in percolating thin films. Samples sputtered at 15 and 60 mA of 50 and 100 nm thicknesses were tested for ohmic behaviour by gradually increasing the potential from 0 to 150 mV (Figure 4.10). The range for testing was chosen in accordance with the signal amplitudes usually detected in experiments with cells on the functional surfaces.

For samples of 100 nm thickness only marginal differences in sheet resistance was measured. Sheet resistance was approximately 0,5 Ω cm^{-1} for both samples of 100 nm thickness. Testing of samples with only 50 nm thickness revealed a bigger difference: 1,1 Ω cm^{-1} for samples sputtered at 60 mA compared to 1,4 Ω cm^{-1} for samples coated at only 15 mA.

Despite this measureable difference which is in accordance with literature findings, sample processing was continued with 50 nm film thicknesses, because were found to be more likely to suffer from bubble formation and sheet detachment when processed through the deposition procedure. Likely thicker samples are subject to higher stress during the procedure resulting from their thickness.

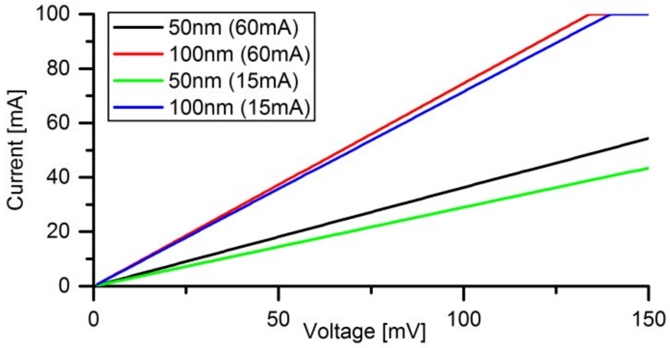

Figure 4.10 Electrical conductivity of sputtered gold films Electical conductivity measured for percolating gold films obtained at 15 mA and crystalline gold sputtered at 60 mA.

4.1.4 Manufacturing of Nano Electrode Ensembles / Growth of nanowires

Vertical free standing nanoelectrodes were grown on thin gold films prepared as described in the previous section. Issues of bubble formation and/or inhomogeneous distribution of electrodes across the surface could be eliminated by optimization of pre-sputtering conditions for titanium and sputtering current for gold, eliminating bubble formation and facilitating homogeneous electrode growth. Both measures were crucial for reliable preparation of NEE surfaces.

Preparation of the NEE surfaces by galvanic deposition into the pores of the template membrane is the key step in the manufacturing process. All steps within the procedure require manual processing of the individual samples for several times, therefore many sources of error are inherent to this step. Consequences of mishandling can range from minor structural damage to

Table 4.1 Error sources during preparation of NEEs

Error	Consequence	Solution
• Detaching of aluminium contact	• No electrical contact to power supply • Insufficient electrode growth	• Application of sufficient amount of Ag-glue •Adjusting drying time
• Leakage from electrolyte chamber	• loss of control over electrode growth	• Ensuring tight seal between surface and chamber
•cracking of substrates inside deposition chamber	• Samples destroyed	• Application of lower pressure when sealing the chamber • controlling appropriate positioning of the substrate inside the cavity after attaching the membrane
• detaching of the membrane during removal from deposition chamber or during rinsing	• Samples destroyed	• Handling with appropriate care
• cracking of samples when cutting of excess parts of the membrane	• Samples destroyed	• Handling with appropriate care
• detaching of the membrane when placing in rack holder	• Samples destroyed	• Avoiding shear forces while processing samples into the rack holder
• detaching of the membrane when dissolving membrane	• Samples destroyed	

complete destruction of the sample. Table 4.1 provides a list of most common errors and possible countermeasures.

In previous works only nanowires of 100 nm diameter have been manufactured [76-79]. This work adds fabrication of 200 and 400 nm diameter nanowires to the scope. Template membranes with larger pore diameters were purchased from the same manufacturer and product line (it4ip, Belgium), therefore no differences to the previously used 100nm pore membranes were to be expected. Membranes were processed similarly by coating with 25 nm gold prior to their use in electrode manufacturing. No special observations were made when coating 200 nm pore membranes, but some 400 nm pore membranes were considerably deformed after being sputtered with gold. Despite this deformation, most membranes could still be used as adhesive forces from the liquid film between membrane and glass compensate the deformation when brought into contact. However for some membranes the deformation was too big to be overcome and the membranes had to be discarded.

In addition, membranes with higher diameter pores were only available with different at different pore densities which needed to be accounted for when comparing results of experiments. Electrodeposition for nanoelectrode growth was performed equally for all pore diameters. After the process-chamber was assembled as described in section 3.1.1.4, deposition was carried out for a defined period of time while the current was recorded. Regardless of the pore diameter, deposition current always started at 1mA which was the limit defined by the power supply settings, dropping very quickly within a minute below 500 µA. Independently of the pore diameter, in all processes the current trace displays a prominent “shoulder” where the decay of the current slows down or in case of the 400 nm samples even becomes constant for more than one minute. After passing this shoulder current decay increases again before

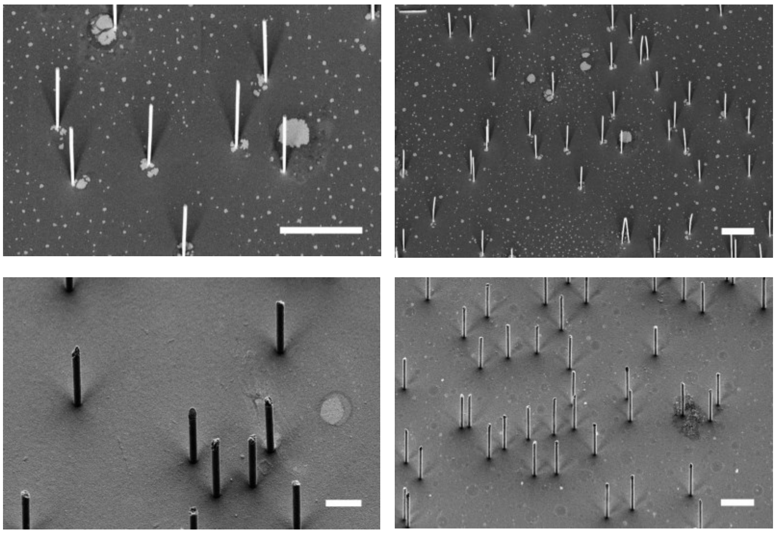

Figure 4.11Nanoelectrodes after removal of the template membrane Electrodes of 200 nm (top, scale bars 5 µm) and 400 nm (bottom, scale bars 2 µm) diameter.

approaching a lower minimum where the current becomes almost constant. Experiments interrupting the deposition process while the current went through the “shoulder-stage” could not reveal its origin. Surfaces where growth was interrupted during early stages did not differ from samples processed for longer times, except for shorter electrode length, which was a finding to be expected.

Overall it is quite remarkable, that the highest currents are recorded for 100 nm pores which also have the lowest density of pores, therefore exposing a considerably smaller surface are as compared to the 200 nm and 400 nm samples.

After the deposition was complete, the current was turned off and the process chamber was disassembled. Removal of the samples from the process chamber was one of the most delicate steps in the whole manufacturing process as the membrane is now attached to the gold coated glass surface. It was crucial to apply as little stress as possible to the “sandwich” while removing it from the base plate. When washing off excess electrolyte after deposition care had to be taken, that no water would enter between glass surface and membrane as the capillary forces of water entering between membrane and glass would immediately destroy the structures and lead to film detachment.

After rinsing the samples were left to dry at air for several hours, then the excess parts of the membrane protruding over the edges was cut off using scissors. Again this step required delicate handling as precise removal of the excess membrane along the edges of the glass was essential for fitting the samples inside the rack holders for subsequent removal of the template membrane in dichloromethane. Collision of the scissors with the glass would result in mechanical stress leading to detachment of the membrane and/or cracking of the glass which in most cases would render the sample being processed unusable.

After removal of the protruding membrane parts the samples were placed racks similar to those used for cleaning of the glasses in the beginning of the procedure. Sample holders were then carefully placed in a bath of dichloromethane for one hour before the solvent was exchanged. After passing through three baths of dichloromethane, the template was entirely removed but residues of inorganic salts were still present on the substrates. These residues were removed by a short bath in water for 10 min which was not used in earlier studies. After this final cleaning step samples were dried at air before being further processed.

4.1.4.1 Analysis of bulk gold electrodes and uncovered NEEs

Bulk gold and NEE electrode surfaces after template removal and cleaning were tested for their electrochemical performance with impedance spectroscopy and cyclic voltammetry. These measurements should give an initial indication of the overall performance of the surfaces as electrodes and allow better evaluation of results from later experiments with samples processed thorough the following manufacturing steps. Performance of NEE samples was expected to be equal of or better compared to the bulk gold electrode, as the vertical nanowires on its surface should increase the surface area and improve electrical properties of the surface as the nanowires allow for better diffusion [66].

Both types of electrodes provided very similar results in EIS measurements (Figure 4.12 and Figure 4.13). Impedance magnitude in Bode plots for both electrodes resembles the behaviour of a simple combination of a resistor and a capacitor in series, showing constant ohmic resistance at high frequencies before at about 200 Hz a transition into a linear increase towards lower frequencies is observed. This ideal behaviour is not confirmed by data in Bode phase and Nyquist plots. For both electrodes the phase does not reach full 90° phase shift but rather goes into a slight declined towards lower frequencies. In the Nyquist plane both electrodes show a slight incline of the plot indicating involvement of diffusion effects. For both electrodes the measured data was fitted using the Randles-circuit model which is commonly used for description of real electrodes. The solution resistance in these measurements was determined

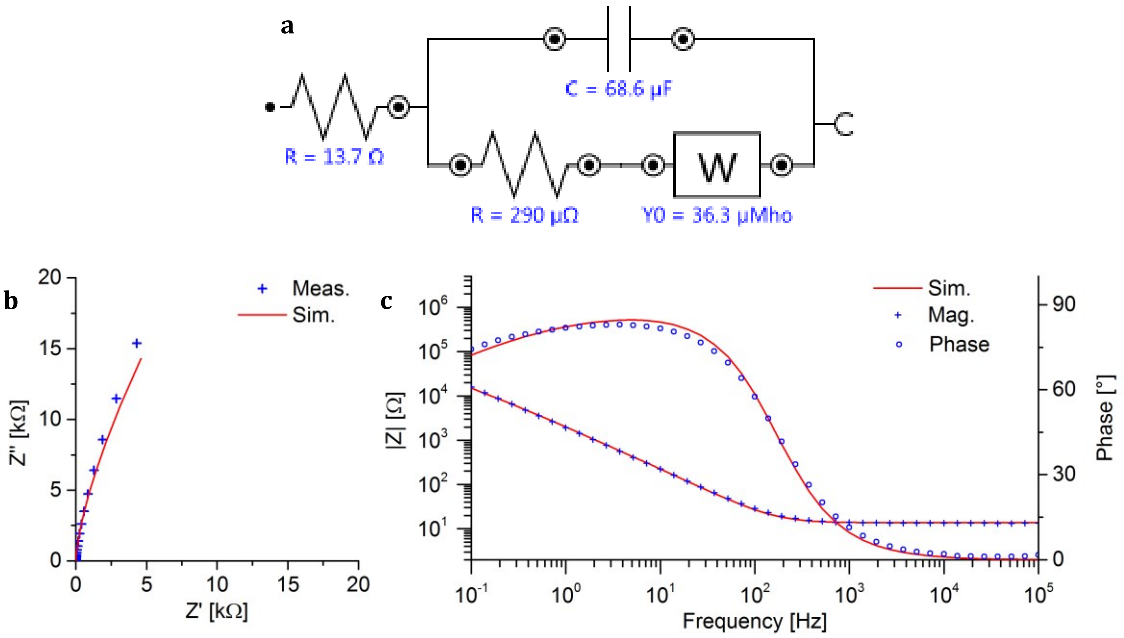

Figure 4.12 Impedance of bulk gold surfaces (a) Equivalent circuit used for modelling of measured data with resolved values; (b) Bode and (c) Nyquist plot for bulk gold substrates measured in 0,1 M NaCl; blue marks represent measurement data, red lines represent simulated simulation from equivalent circuit fitting

to be R_S = 13 Ω. The following RC-parallel element is almost exclusively governed by the capacitance of C = 68 µF, with small contributions of the Warburg element accounting for kinetic contributions.

Theoretically an equivalent circuit model for the NEEs should contain separate contributions of the bulk gold surface and the nanowires protruding from it. Therefore modelling with an additional RC-circuit element, added in parallel to the model established for the bulk gold surfaces, was attempted. Unfortunately This model should account for the separate contributions of bulk gold and the nanowires as competing elements, where the current passes either through the bulk surface or through the nanowires. Unfortunately this model provided no satisfactory results when fitted to the measured data. A good fit for the measured data was achieved using the same Randles-circuit-model as used for the bulk electrode. The approximation was even further improved, when the ideal capacitor element used for bulk gold electrodes was replaced with a constant phase element accounting for non-ideal behaviour of the system. The CPE-coefficient was determined to be n = 0,91 which is still close to “ideal” behaviour. These deviations may occur through structural defects and inhomogeneity resulting from the difficile manufacturing procedure. The difficulties encountered when modelling these rather simple examples illustrates the problems inherent to equivalent circuit modelling, which increased during the analysis of samples after the additional processing steps described below.

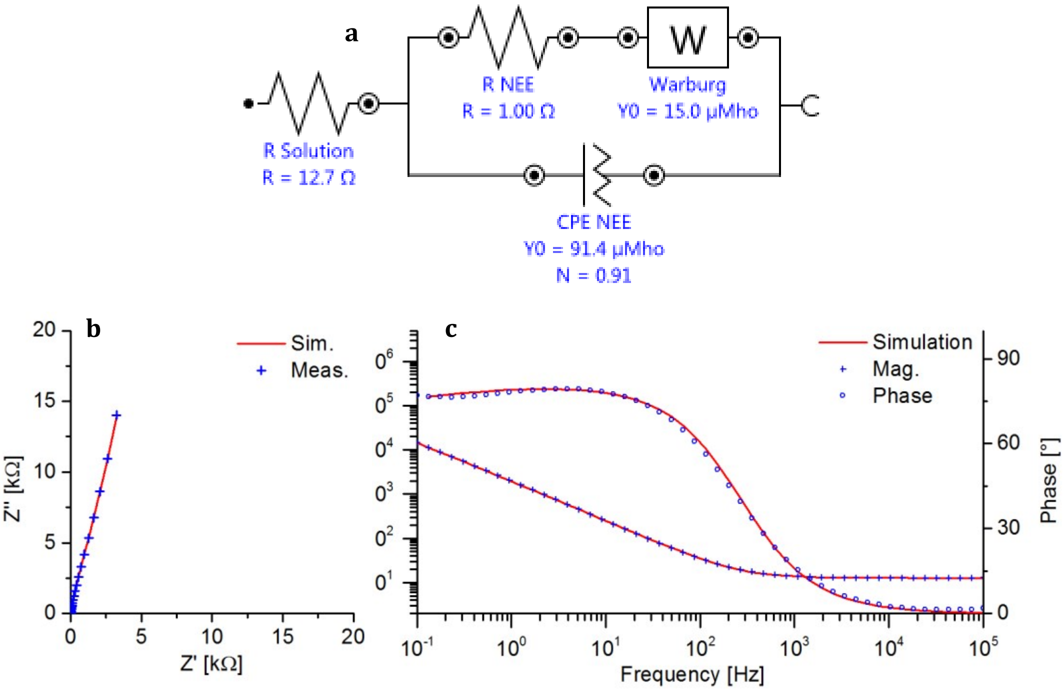

Figure 4.13 Impedance of bulk gold surfaces (a) Equivalent circuit used for modelling of measured data with resolved values; (b) Bode and (c) Nyquist plot for bulk gold substrates measured in 0,1 M NaCl; blue marks represent measurement data, red lines represent simulated simulation from equivalent circuit fitting

4.1.4.2 Cyclic Voltammetry of Bulk Gold Electrodes and NEEs

Both types of electrodes were tested using cyclic voltammetry (CV) measurements. Experiments were performed in a solution of 0,1 M NaCl as supporting electrolyte with and without the addition of 10 mM ferricyanide.

Electrodes of both types show regular behaviour with well-defined anodic and cathodic waves present in the cycle, as expected for the fully reversible reaction of ferricyanide (Figure 4.14). This behaviour is in accordance with the behaviour of thin film electrodes described in literature [85]. For bulk gold electrodes the peak separation is about 70 mV which is not too far from the theoretical value of 59 mV. CVs obtained from measurements with NEEs are slightly broader in shape and show a higher peak separation of about 90 mV. It is rather surprising, that the current intensity for the NEEs is actually lower than for the bulk electrodes. The opposite as was expected as the NEEs should provide a higher surface area and superior diffusion properties at the nanowires. It is assumed that the separated sheets observed in electron microscopy do certain resistances and capacities reducing the current transfer at the electrolyte-interface (Figure 4.15).

It must be mentioned, that the experimental chamber design used for all experiments in this work was not ideal for these measurements, because the design of the chamber was focused on ideal conditions for experiments with cells and not electrochemistry. The volume of the chamber confined by the Teflon ring only holds only 1 ml, which is rather small, especially for bulk electrodes without coverage of the insulating film. In addition the counter-electrode should be large with respect to the working electrode. When working with the uncovered electrodes in these experiments, the opposite is the case as the surface of the platinum wire is only 12 mm^2 compared to 78 mm^2 for the bulk gold electrode. Therefore quantitative analysis of the data may be erroneous. This is an unfortunate circumstance, but it was the priority to perform

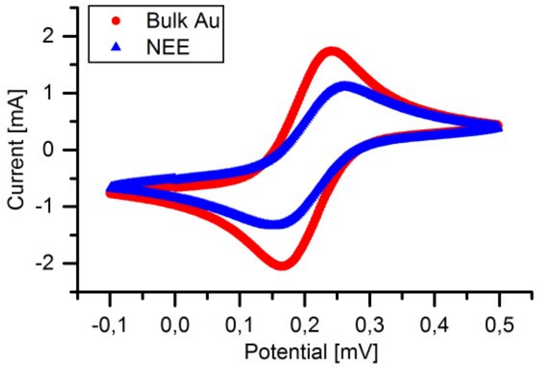

Figure 4.14 Cyclovoltammogram of bulk gold and NEE electrodes Higher currents were detected for bulk gold electrodes when compared to NEEs. This may be a result of the adverse influence of the sheet structure shown in Figure 4.15. Measurements performed in10 mM $K_4[Fe(CN)_6]$ in 0,1 M Nacl, $\nu = 100$ mV s^{-1}.

experiments under the same electrode- and chamber-geometry like the following experiments with insulated surfaces. In these following experiments the size of the counter electrode will be sufficient as most of the surface will be covered by the spin-coated insulating film. For the same reason the currents in these later experiments lower and hence the turnover of the analyte, eliminating or reducing the effect of possible changes to its concentration. To overcome this issue of misbalanced electrode size, a reconstruction of the entire chamber-concept would have been required which was beyond feasibility.

Despite the above mentioned experimental deficiencies from this, non-ideal chamber construction, the results presented here are believed to be true at least in a qualitative fashion. For determination of the maximum peak currents a counter electrode of several square centimetres would be required which cannot be integrated into this setup. Both anodic and cathodic peak potential are well defined and the peak separation is about 80 mV, which is an acceptable value compared the 59 mV for a perfect system, especially considering to the non-ideal chamber construction.

The unexpected finding of inferior performance of the NEEs in CV may be explained by findings during the investigation of flawed samples with partially detached surfaces in the SEM. The surface of deposited NEEs does not consist of one homogeneous gold film, but instead three well separated layers of gold where observed in the electron microscope (Figure 4.15). The under most layer exhibits the same structure as observed for bulk gold samples with the desired percolating structure for the deposition process. The top layer likely originates from the sputtered gold film on the template membrane. Both films are fused together by the third sheet in the middle, likely formed from the residual electrolyte trapped between template and substrate. According to this theory, the "shoulder" in the current traces during the deposition process would result from the reduction of the material trapped between the gold films. The currents would then drop as all enclosed material has been reduced. This hypothesis is also

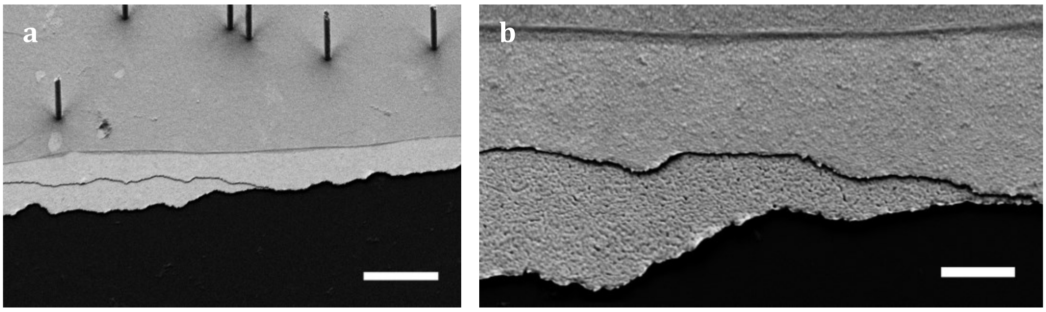

Figure 4.15 Gold layers after Deposition A sample with partially detached gold film after removal of the template membrane reveals the structure underneath nanoelectrode surface: it consists of three separate layer layers of gold originating from the sputtered gold film (front), a gold film formed by the electrolyte during deposition and the attached gold film from the template membrane.

supported by the finding that the entire deposition process failed if only water instead of electrolyte was inserted between the gold films before deposition. From the observation of these three separate sheets within the metal film, it must be assumed that certain electrical capacitances and resistivity exist between the separate sheets, accounting for the reduced peak currents in CV.

Another experiment was performed to test for the influence of different length of nanowires. CVs were measured nanowires of two different lengths (Figure 4.16). The results show a tendency towards higher currents for NEEs with longer nanowires as it was expected. Nevertheless the maximum currents were subject to spreading as a result of inhomogeneous sample quality.

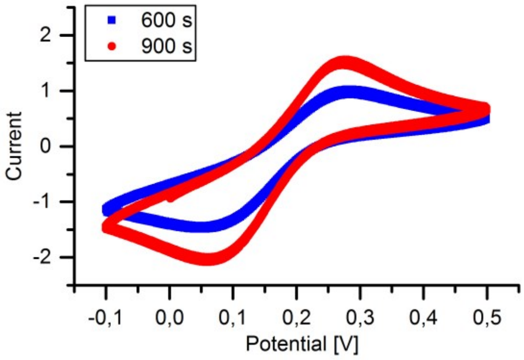

Figure 4.16 Cyclovoltammetry with NEEs of different electrode length Electrodes of higher length exhibit higher currents. Measured in 10 mM $K_4[Fe(CN)_6]$ in 0,1 M NaCl, $\nu = 100\ mV\ s^{-1}$.

4.1.5 Spin coating

After the template membrane was dissolved, ensembles of free standing nanoelectrodes were obtained. For successful interfacing of cells with the NEAs, an insulating layer was required to avoid depolarization of the cells. The insulation ensures that electrical contact is solemnly established via the nanoelectrodes and not through contact of the conductive bottom layer with the cell culture medium. In this case depolarization of the cells may occur by providing a current path from the intracellular space to the surrounding medium.

Spin coating is a very delicate process requiring numerous parameters to be perfectly balanced in order to obtain thin films in a reproducible manner. Spin speed, acceleration and deceleration rates, the amount of solvent (mixture) dispensed, concentration of dissolved material, viscosity and vapour pressure are interdependent parameters, which determine the thickness of the film and its structural integrity as the solvent evaporates during and after spinning [86]. In previous works a brief protocol for coating the substrates with Bisphenol-(A)-polycarbonate dissolved in a 1:1 mixture Chloroform and 1,2-Dichlorobenzene was established. Although providing films of acceptable quality, no quantification of the film thickness was conducted. This gap was closed by coating substrates at three different spin speeds and measuring the resulting thickness with a profilometer. The results show an exponential decay in film thickness with respect to the spin speed (Figure 4.17). This is in agreement with the expected behaviour for spin coated films. Speeds higher than 1800 rpm were not tested because film thicknesses of less than 400 nm as obtained from spin speeds > 1500 rpm are not desired. Also the centrifugal forces at higher spin speeds could potentially damage the vertical electrodes. After spin-coating samples were immediately transferred to an oven and dried at 85°C for 1h.

The dried samples were of yellow-green colour at the centre area surrounded by a red ring separating the side areas. In these parts closer to the edge of the surface, the polycarbonate has

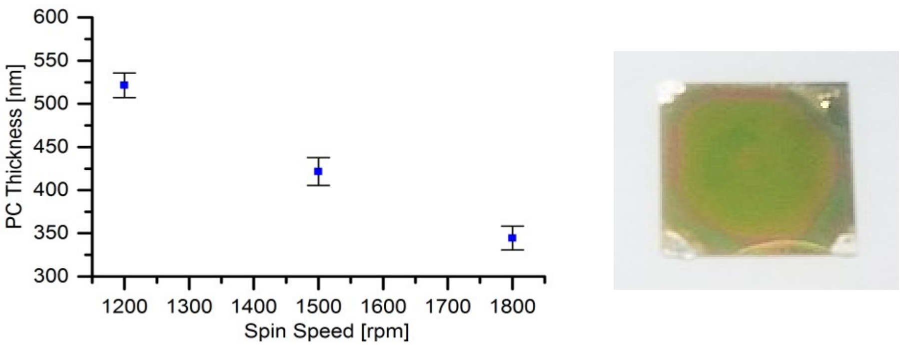

Figure 4.17 Thickness of spin coated polycarbonate films depending on spin speed (left) results from measurement of film thickness on conventional samples of 24 x 24 mm. (right) spin-caoted NEE after annealing at 85°C

a larger thickness. This can hardly be avoided in spin-coating process but is only of little significance, as the in the experiments the area is confined to the centre part by the experimental chamber construction (see below) where the thickness of the film is constant.

4.1.5.1 Analysis of Insulated Surfaces

For bulk gold surfaces passivated with spin-coated polycarbonate significantly higher impedances compared to bulk samples were expected due to the dielectric properties of polycarbonate. Spectra should provide information about the quality of the insulation layer, especially for NEE surfaces with the vertical nanowires extending higher than the thickness of the polycarbonate film measured after spin-coating. Therefore the parts of the nanowires should have only little or no coverage increasing the admittance of the system.

Data measured from bulk electrodes confirmed very good insulating behaviour of the spin-coated polycarbonate films (Figure 4.18 a-c). The magnitude of the impedance indicates purely capacitive behaviour within the measured frequency range up to 100 kHz. In accordance with this result the phase is shifted almost 90° over the entire range. In the range of 1-100 Hz measurements became unstable; therefore measurement points show slight deviations. Slight

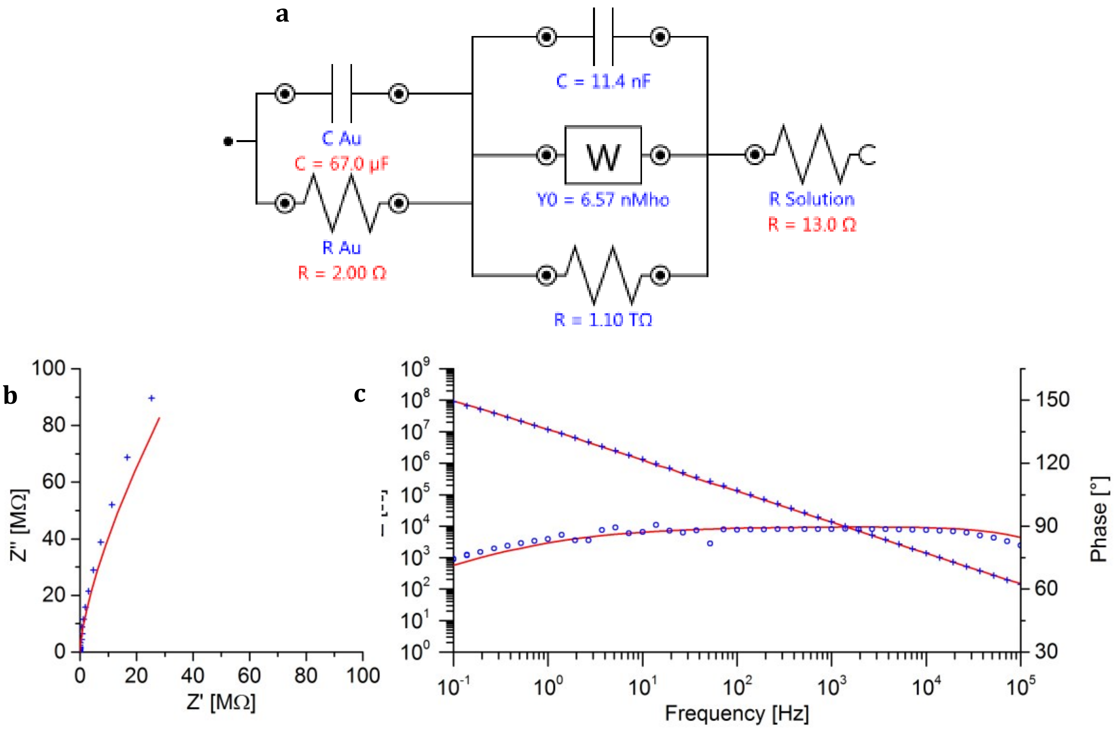

Figure 4.18 Impedance of Au-surface insulated with polycarbonate (a) Equivalent circuit used for modelling of measured data with resolved values; (b) Bode and (c) Nyquist plot for bulk gold substrates measured in 0,1 M NaCl; blue marks represent measurement data, red lines represent simulated simulation from equivalent circuit fitting.

curvature towards both ends of the measured spectrum indicate possible effects of other components but these frequency-ranges were not accessible with the instruments used in this work. Circuit modelling for this case was done based on the results for the bulk gold electrode. An RC-parallel circuit with C_{Au} =76 µF and R_{Au} = 2 Ω was complemented with another RCW-parallel element that should account for the resistance and capacitance of the polycarbonate film. The Warburg-elements was also added in parallel at this point as the insulating film now forms the interface to the electrolyte. In accordance with the physical current path the solution resistance is placed in line with the rest of the circuit. All previously determined parameters were kept constant during fitting of the RCW-element. The resulting values of R_{PC} = 1,1 TΩ and C_{PC} = 11,4 nF appear very plausible considering the insulating propertiers. A rough estimate of the capacitance assuming a simple plate capacitor with an area of 1,5 cm^2 and plate distance of 400 nm using ε_{PC} = 2,9 provides a value of approximately C_{Th} = 9 nF which is surprisingly close.

As expected the spectra obtained from NEE surfaces shows very different behaviour: In the Nyquist plane an incomplete semicircle indicates the presence of at least one RC-element before the plot transitions into a 45° incline indicating mass-transfer governed kinetics (Figure 4.19).

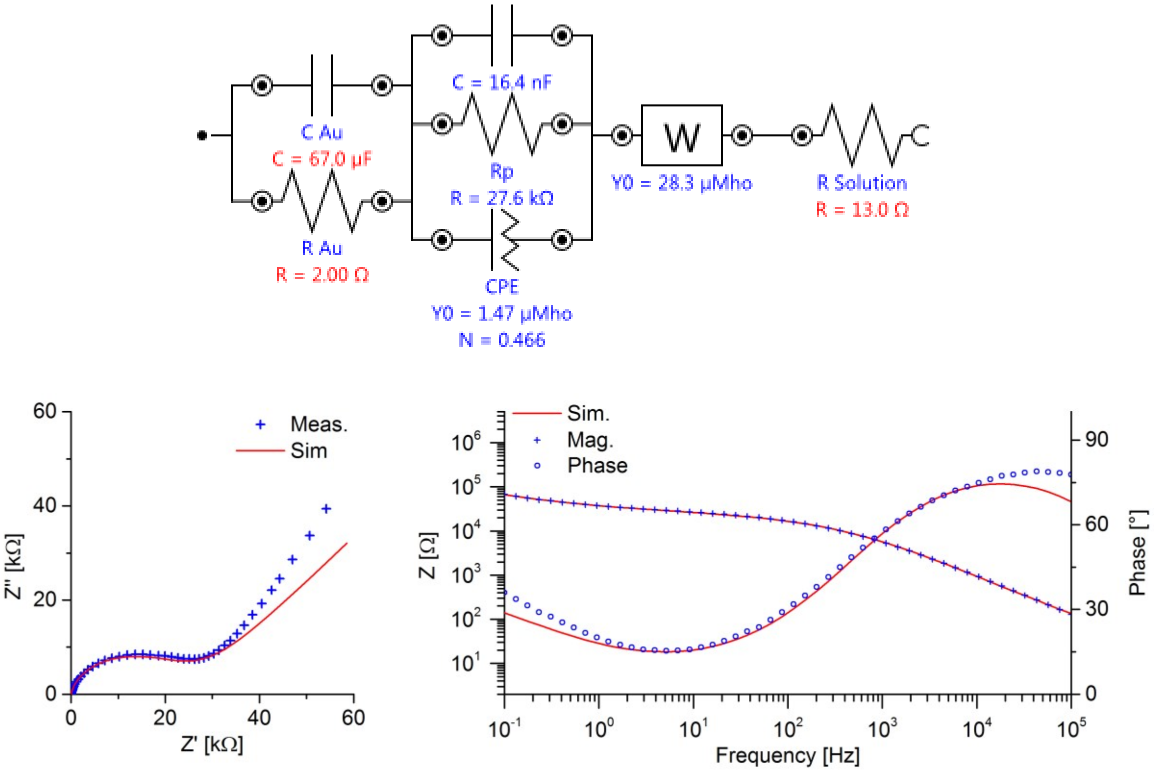

Figure 4.19 Equivalent circuit for NEES with polycarbonate coating(a) Equivalent circuit used for modelling of measured data with resolved values; (b) Bode and (c) Nyquist plot for bulk gold substrates measured in 0,1 M NaCl; blue marks represent measurement data, red lines represent simulated simulation from equivalent circuit fitting.

The presence of such kinetics is an indication of an electro-active electrode surface at which such reactions can take place. The maximum impedance at low frequencies is three orders of magnitude lower than for the insulated bulk gold electrode and only one order of magnitude greater than for surfaces without polycarbonate insulation.

Equivalent circuit modelling for the coated NEE was attempted following the same procedure described in the above section. This time another RC-parallel element was added to the model proposed in . The idea was to model an alternative current path through the nanoelectrodes which competes with the equivalent circuit element representing the insulating film, but unfortunately no acceptable correlation could be established using this model. Instead the equivalent circuit displayed in Figure 4.19 was developed. Theoretically there should be a competition between current paths, but like this can simply not be resolved by from the data obtained. Instead both effect are modelled together by the R-C-CPE-parallel element with the Warburg-impedance in series. This surface model was developed empirically and although it fits the data at least in terms of impedance magnitude, its accuracy should be confirmed in further experiments.

Cyclic voltammetry of polycarbonate coated samples was performed to verify the insulating properties of the film. For coated bulk gold electrodes only minute currents were measured like a result of charging of the insulating film (Figure 4.20). The obtained curve had an elliptical shape indicating capacitive charging. The current measured on uncoated bulk gold electrodes was six orders of magnitude higher compared to insulated ones. With the current in the range of only few microamperes there is no electrode reaction present in this example.

A different appearance is encountered for the insulated NEE: Towards negative potential a

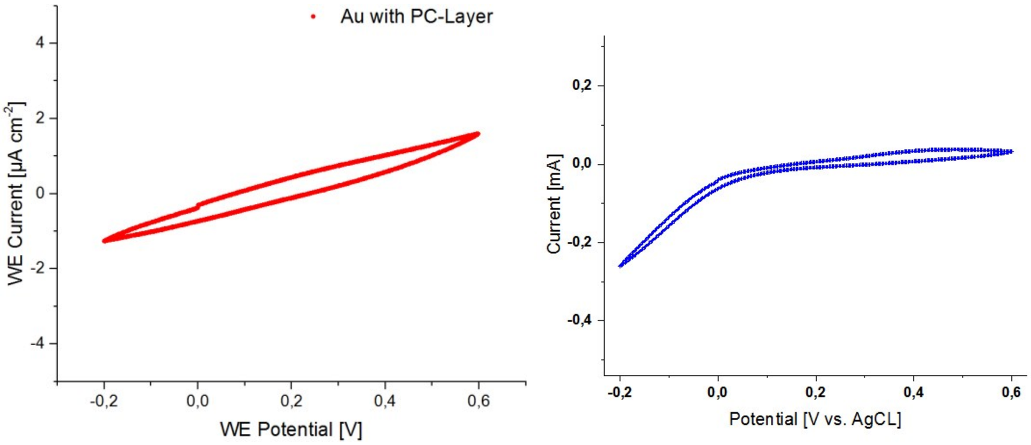

Figure 4.20 Cyclic voltammetry with polycarbonate coated electrodes Insulated bulk gold electrodes only show an elliptical voltammogram resulting from capacitive charging. NEEs after spin-coating show a strong reductive current occurring at negative potential. Measured in 10 mM $K_4[Fe(CN)_6]$ in 0,1 M Nacl, ν = 100 mV s^{-1}

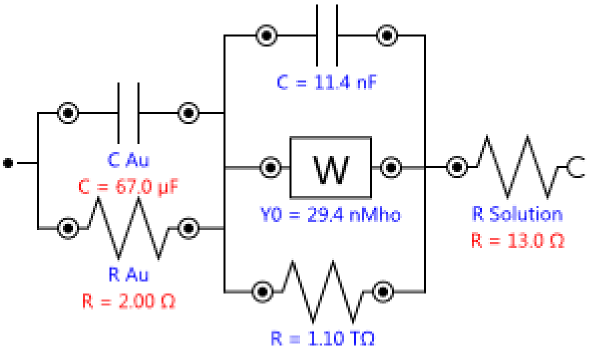

Figure 4.21 Equivalent circuit for PC-coated gold after etchingA capacitance of 11,4 nF for the polycarbonate insulating layer is obtained from equivalent circuit modelling. A value of 9 nF is obtained from simple calculation for a plate capacitor with similar dimensions as the spin-coated film.

distinct increase of the current can be seen, although it is as well few orders of magnitude below the uncoated samples. The origin of this reductive current is unknown, because if it would a rise from a reaction of the insulating film it should be visible in the experiment with the bulk gold electrode. This is not the case, therefore no exact statement about this observation can be made.

4.1.6 Electrochemical Analysis of the Etching Process

4.1.6.1 EIS after etching of insulated surfaces

EIS measurement of etched polycarbonate on gold electrodes was performed to get an impression whether the insulating properties of the film are reduced as a result of the etching process. Possible effects of the etching process should be easier to identify in this scenario than with samples of NEEs, as their behaviour is already significantly altered by the presence of the nanoelectrodes. In the ideal case these experiments should help identifying the changes detected in NEE samples to changes in the insulating film.

In case of bulk gold electrodes no severe change in impedance was expected, as the etching process should leave the insulating film mostly intact. This was confirmed by the experimental findings (Figure 4.22). Similar to the not-etched sample the Bode-diagrams of magnitude and phase indicate purely capacitive behaviour of the electrode (Figure 4.18). The resistance was so high that it was hard to obtain a stable measurement, as can be seen in the phase-plot. Phase shift is almost 90° over the whole covered frequency-range. Similarly the Nyquist plot shows an almost perfectly vertical line. From this result it may be concluded, that the integrity of the insulating film is not corrupted by the etching.

For NEE samples the etching of the insulating layer should result in reduced impedance after the polycarbonate insulating layer was successfully removed from the nanowires. Impedance magnitude as displayed in the Bode-plot is significantly reduced in the moderate frequency range between 10 Ω and 1000 Ω. Similar the phase passes through a second maximum at approximately 5 Hz with 60°. In the Nyquist plot the presence of an additional time constant at high frequencies is detected similar to the observations for the not-etched sample. Only this time the resistance and capacitance obtained for this time constant by the electrochemical circle fit is smaller than before etching, hence it may assumed that here the effect of the etching process becomes visible.

Cyclic voltammetry of bulk gold electrodes with etched insulation layer did not detect any faradaic current. Dunring none of the performed experiments defined oxidation or reduction peaks could be observed. Instead only elliptically shaped voltammograms were observed, showing the result of capacitive charging. The highest currents were observed at the vertex-potentials at a magnitude of less than 2 µA which is considerably low compared to almost 2 mA measured with bulk gold electrodes without the insulating film. In comparison to the response from insulated electrodes previous to etching shows only miniscule changes. In the absence of

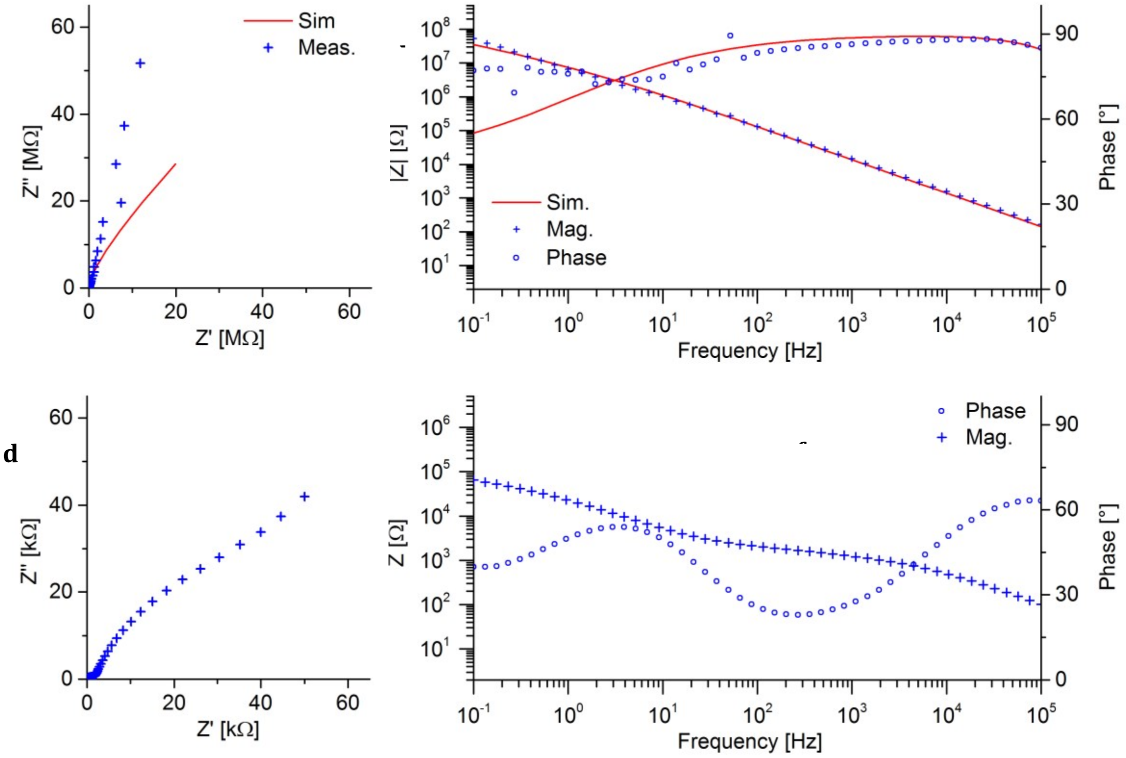

Figure 4.22 impedance of bulk AU with PC passivation after etchingEIS data of (a-c) PC-insulated bulk gold electrode after etching (d-f) NEE with 100 nm electrodes after etching; Bode plots of magnitude (a, d) and phase (b, e) and Nyquist diagram (c, f)

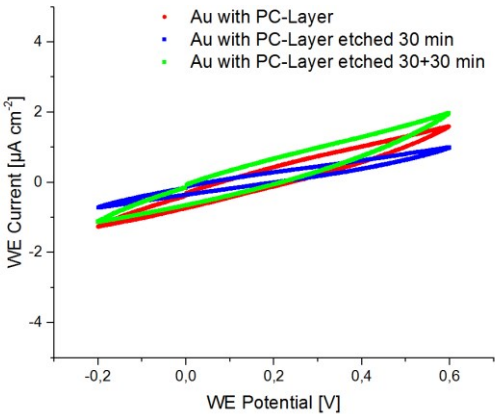

Figure 4.23Cyclic Voltammetry of etched insulation on bulk gold electrode Even after extensive etching of 1hour no significant change is detected in the spin-coated film using CV. Measured in 10 mM $K_4[Fe(CN)_6]$ in 0,1 M Nacl, ν = 100 mV s^{-1}.

any faradaic reation at the electrode the detected currents must solemly result from capacitive charging of the working electrode and insulating layer.

Cyclic voltammetry of etched NEEs should provide a quantitative insight to the capability of the nanowires for faradaic electron transfer. The selective etching process should significantly improve the NEEs capabilities to facilitate such reactions. Voltammograms of the NEEs before etching discussed in the previous section showed that these samples were already exhibiting significantly higher currents than insulated flat electrodes. The question was, to what extend this current would be enhanced after the etching and how close to the behaviour of NEEs without insulation. For this reason the performance of insulated NEEs was compared before and after etching. Additional experiments dividing the etching process into short intervals were performed to closely follow the changes resulting from etching (Figure 4.24). Voltammograms of etched samples show a higher current with defined maxima which were recognizable

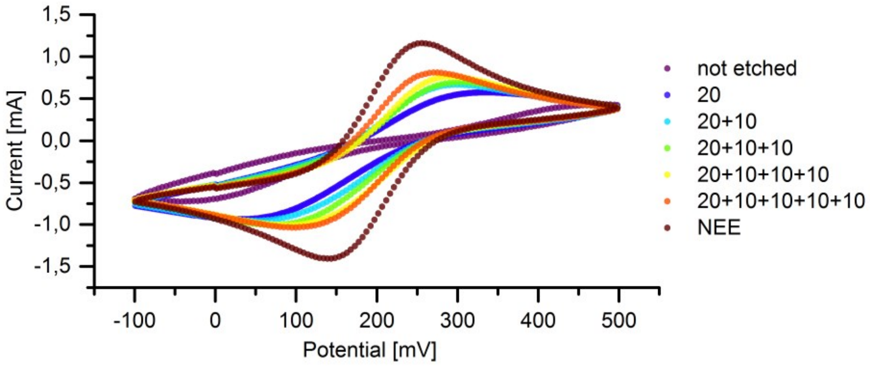

Figure 4.24 Cyclic voltammetry of NEEs after etching Repeated CV experiments during etching steps reveal a clear increase in current at the NEEs achieved after ecxtensive etching. Measured in 10 mM $K_4[Fe(CN)_6]$ in 0,1 M Nacl, ν = 100 mV s^{-1}

previous to etching. Nevertheless these peaks are separated 200-300 mV which is far from ideal reversible behaviour. When etching was performed in several intervals the continuous improvement of charge transfer became even more obvious.

4.1.6.2 XPS Analysis

Additional analysis of the etching process was performed with x-ray photoelectron spectroscopy (XPS). For better comparison NEEs without insulation were also included in the experiment. NEEs with polycarbonate insulation were tested before and after the etching process. Data obtained from these measurements is summarized in Figure 4.25. For better representation, peaks were not labelled in the plot but instead summarized in Table 4.2.

The intensity for uncoated NEE surfaces is much higher and is dominated by two very intensive peaks cleary assigned to gold at 83,6 eV (Au 4f7) and 87,2 eV (Au 5p3). Further gold signals of medium intensity are detected at 335 eV (Au 4d5) and 352 eV (Au 4d3). The presence of very strong signals of carbon (285 eV, C 1s) and oxygen (531 eV) was not expected for uncoated NEEs but can be explained with residues from the template membrane used in the deposition process which was not entirely removed from the surface. From energy and elements in question for the sample only silicon would be a suitable candidate. As the penetration depths of X-rays in metal is only a few nm at the most, the presence of silicon in the measured signal may hint to damages in the metal film where the glass substrate is uncovered.

The spectra recorded from polycarbonate-coated NEEs before and after etching are of very similar structure in terms of intensity and position of the detected peaks. For both samples the spectra are dominated by two prominent peaks of carbon (284 eV) and oxygen (531 eV). This was to be expected as the surface consists of polycarbonate and is hence composed mostly from

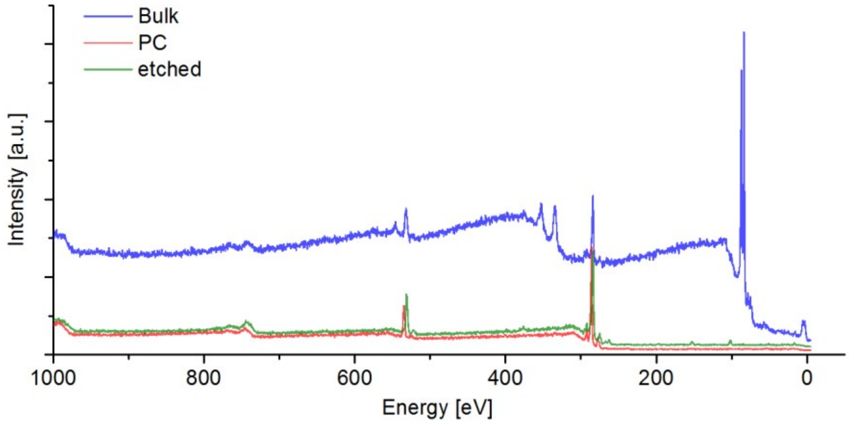

Figure 4.25 XPS spectra of NEE surfaces Data recorded at 20kV

these elements. In the etched sample peaks of very low intensity at 101 and 152 eV, likely to be assigned to silicon can only result from contamination or stray signals from the edges of the specimen. The only signals potentially resulting from the presence of gold were detected at 760 eV (Au 4s). However this signal is present in all samples with similar intensity and is therefore not considered as sufficient proof of successful etching of the nanoelectrodes. Since the penetration depth of the x-rays is rather low, the nanowires may still be covered under a thin polycarbonate layer despite the etching. But the absence of any other signals assignable to gold lead to the conclusion, that with XPS no sufficient analysis of the NEEs can be performed, therefore the investigations with this method were discontinued.

Table 4.2 XPS experiments with NEES Overview of detected signals, their assignment and intensities in examined samples. Gold signals are highlighted in grey colour.

Energy / eV	Assignment	NEE	NEE + PC	NEE + etched PC
2,8	Si 3p	weak		
5,6	Au 5p	weak		
83,6	Au 4f7	very high		
87,2	Au 5p3	very high		very weak
101,6	Si	medium		very weak
152,4	Si 2s			very weak
285	C 1s	high	high	high
335	Au 4d5	medium		
352	Au 4d3	medium		
531	O	medium	medium	medium
760	Au 4s	weak	weak	weak

4.1.6.3 GFP labelling of free nanowire electrodes

In order to test whether the etching procedure was successful, in early stages of this work the NEEs were labelled with His-tag-GFP method. Etched NEEs were first incubated with 0,04 mM NTA and 0,4 mM $NiCl_2$ in PBS in H_2O for 1h. After washing with PBS, GFP was coupled to NTA by incubation with 10 mM His-GFP in PBS for 20 min. Samples were again rinsed and then the nanowires were imaged with laser-scanning microscopy.

If etching was successful, the nanowires should now be visible as vertical structures. This was found to be the case, as indicated by the appearance of vertical structures in random distribution over the observed surface (Figure 4.26). Nevertheless the intensity of the fluorescence from individual nanowires shows large variations, indicating inhomogeneous coverage of the nanowires with the NTA-GFP label, likely as a result of inhomogeneous removal of the polycarbonate from the nanowires. Despite this deficiency the experiment was taken as an indication for the general functionality of the alkaline etching with 2 M NaOH. Unless in case of macroscopically large defects, the method was not expected to allow judgement of the integrity of the polycarbonate bottom layer. Microscopic pores eventually caused by the etching procedure would show only little or no intensity compared to the labelled nanowires. Impedance spectroscopy was instead used in further studies, allowing quantification of the obtained results and being a non-destructive method.

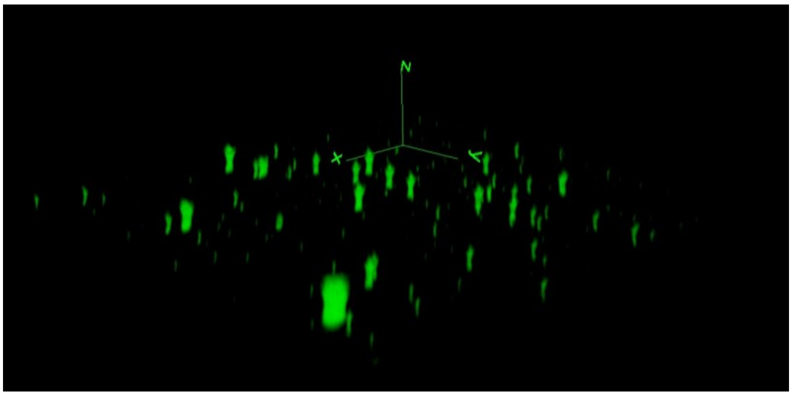

Figure 4.26 NEE surface labed with GFP vib Ni-NTA bonding. Nanowires are well visible as vertical green structures. Different intensities indicate inhomogeneous coverage of the nanowires.

4.1.7 Manufacturing of reference electrodes

The electrochemical analysis of nanoelectrode ensembles required a three-electrode configuration for reliable electrochemical measurements. Only with this configuration an independent measurement of voltage and current is possible. In such a configuration the working- and counter-electrode are complemented with a reference electrode allowing accurate measurement of referenced potentials. In literature electrochemical potentials are commonly referenced with respect to the standard hydrogen electrode (SHE). As SHEs require excessive constructional effort they are often replaced by reference systems such as the silver/silver chloride ($Ag|AgCl|Cl^-$) or calomel ($Hg|Hg_2Cl_2|Cl^-$) electrodes which allow the construction of more convenient electrodes and provide a constant reference for a broad range of applications [87, 88]. Potentials measured relative to silver chloride- or calomel-electrodes can be converted SHE-referenced potentials taking into account their relative offset towards this reference standard.

In this work, the use of commercially available reference electrodes was not possible due to the small dimensions of the experimental chambers and their incompatibility for long-term use in cell culture medium, as proteins contained in the serum would congest the porous frit of the electrodes. Although there are specialized electrodes available for use in cell culture environment, these are limited to short term use and require extensive cleaning procedures to remove protein residues accumulated during operation. Therefore a miniaturized solid state reference electrode (SSRE) was used in this work. SSREs offer excellent opportunities for miniaturization as they only require a thin film to be coated on a conductive substrate, e.g. a printed metal pad or a metal wire of small diameter. Since manufacturing of these electrodes is simple and cheap, fresh electrodes could be used for any experiments.

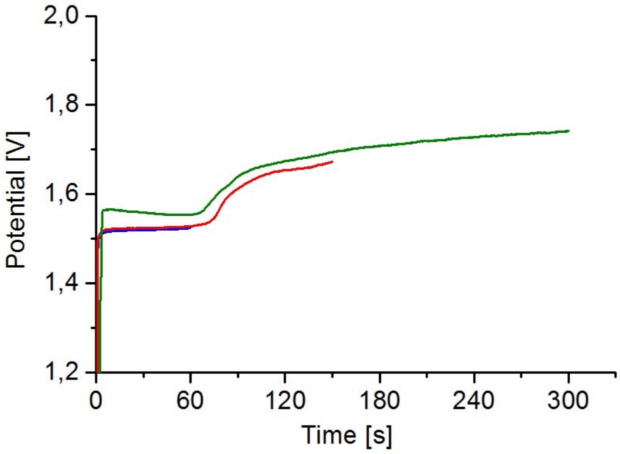

Figure 4.27 Deposition of AgCl on silver wires Voltage was recorded during deposition of AgCl on silver wires from 3M KCl solution. Plot shows voltage recorded during deposition of different times. Samples were inspected with SEM afterwards as shown in the next figure.

In this work a silver wire of 99,9% purity (d= 0,5 mm, Roth, Germany) was first coated with a layer of AgCl by cathodic reduction in an aqueous solution of 3M KCl at a current density of 0,3 mA cm^{-2} (Figure 4.27). Before coating silver wires were cleaned by sonication in isopropanol and water using the same procedure used for glass coverslips. Comparison of AgCl deposition on cleaned and untreated silver wires showed both requirement and effectiveness of the cleaning procedure. Uncleaned wires required higher potentials for deposition and resulted in inhomogeneous coating. After the current was turned on, the recorded voltage rises quickly before reaching a plateau at about 1,5 V which remains constant for 60 seconds before a further increase in voltage could be observed. To understand the origin of this voltage characteristic, wires were coated for different time length (Figure 4.27) and investigated under the SEM (Figure 4.28 a-c). The wire coated for only 60 s shows incomplete coverage of the surface. After 120 s the coverage is almost complete but small gaps can still be observed. These are closed and after the 180 seconds the surface is entirely covered and the crystallites become smaller. From these results it was concluded that deposition times of at least 180 seconds are required to ensure homogeneous coating of the wire with silver chloride.

After manufacturing of the AgCl coating the wires were coated with silver ink to complete the SSRE. The tips of silver chloride coated wires were immersed into epoxy-silver resin and the film was thinned using a glass capillary pipette. The wires were carefully moved in and out of the pipettes opening to form a homogeneous coating over a length of 5-10 mm at the tip. Coated

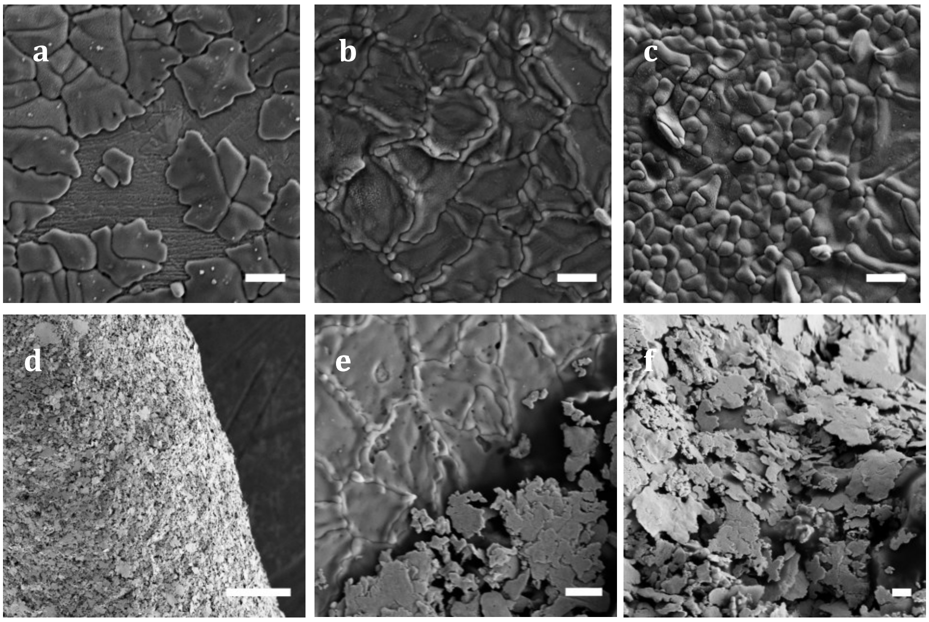

Figure 4.28 AgCl coating on silver wires after Coating of silver wires was performed at a constant potential of 0,1 mA while the resulting potential was recorded. (a) 60 s; (b) 150 s; (c) 300 s; Scale bars are 2 µm. border of electroplated AgCl and epoxy-coating; (center) magnified view of the same are showing apparent structural differences; (right) epoxy-cated area.

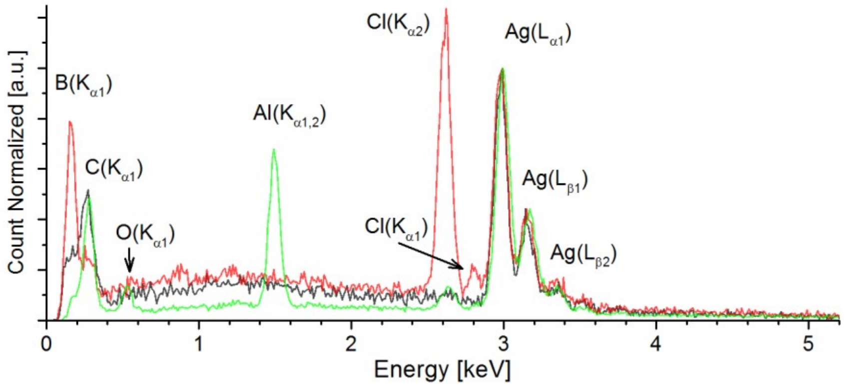

Figure 4.29 EDS of reference electrodes EDS pectra of bulk Ag-wires (black), AgCl-coated wires (red) and wires coated with epoxy-resin (green). Peaks are labeled with assigned spectral lines according to reference [89]

wired were then dried in an oven at 80°C for 1hour to cure the epoxy resin. The coatings obtained with this method would form a leaf-like structure at the surface (Figure 4.28 d-f). Chemical composition of the manufactured coatings was examined by electron dispersive x-ray spectroscopy (EDS). Spectra were recorded for bulk silver wires, silver-chloride coated wired and the epoxy coated wires at an acceleration voltage of 10 kV (Figure 4.29). For better comparison all data presented is normalized with respect to the silver $L_{\alpha1}$ line, which has the highest intensity for this element [89].

The presence of silver was clearly confirmed in all samples by the presence of lines matching the elements fingerprint: two overlapping lines at 2,97 and 2,98 keV (Ag $L\alpha_{1,2}$, high intensity,), 3,15 keV (Ag $L\beta_1$, medium intensity) and 3,34 keV (Ag $L\beta_2$, weak). After normalization to the Ag $\beta_{1,2}$ line, all spectra exhibit striking similarity.

Another line present in all examined samples is assigned to carbon at 0,27 keV (C K_α). It is of notable intensity for bulk and epoxy-coated samples. On silver chloride coated wires its intensity is even higher and the peak is shifted to 0,15 keV. According to EDS databases, lines at this energy would be assigned to beryllium or boron, but from the previous processing the presence of these elements can be excluded, especially in such quantities. More likely it is a result of drifted detection which can occur as EDS detectors can become instable at low energies. The origin of carbon lines in the sampled is also unclear, as the samples should not contain significant quantities of carbon. More likely the origin of these lines must be from contamination within the detector, of the sample holder or within the SEM chamber rather than from the sampled wires. The silver-chloride coated wire shows the presence of chloride clearly by lines at 2,62 keV (Ag) and 2,79 keV (Ag $K_{\beta1}$). The overlapping $K_{\alpha1}$ and $K_{\alpha2}$ lines are also marked by a small shoulder of the line.

Wires coated with the epoxy-resin were expected to show lines for carbon and oxygen being the constituents of the paste. For carbon a shifted signal at 0,15 keV was detected as already discussed above. The presence of oxygen was confirmed as well by the corresponding line at 0,52 keV (O Kα). For chloride only a very weak signal is detected, likely a result from penetration of the electron beam into lower silver-chloride layer underneath the epoxy-resin. The presence of a strong line assigned to aluminium in the spectrum was assumed to be an artefact from the way the data was acquired: If spectra were recorded at the centre of a wire, the intensity of the signal originating from silver would exceed all other lines so they would become almost invisible. To obtain appropriate intensity from the coating, measurements were performed towards the edges of the wire where a higher penetration depth into the coating could be achieved (Figure 4.30). The disadvantage of measurement in this location was the occurrence of the strong ling from aluminium and carbon resulting from stray electrons. To confirm this hypothesis the intensities of all elements likely to be present were mapped by EDS to obtain information about spacial distribution of the individual elements (Figure 4.30). As expected silver, chlorine, carbon and oxygen are detected with good intensities and matching the position of the coating within the field of view. Mapping for potassium was only done to test for possible residues of potassium chloride from the deposition process of the AgCl layer.

Data for the silver-epoxy-resin show a very strong peak for aluminium although the presence of this metal especially at such quantity was not expected. The signal of aluminium may arise from the sample holder, as spectra were taken towards the side of the wire where a larger portion of the applied coatings could be measured. In spectra taken at the centre of the wire, the silver signal became predominant as the bulk material of the wire contributes to the signal as well, covering the peaks from other elements with its high intensity.

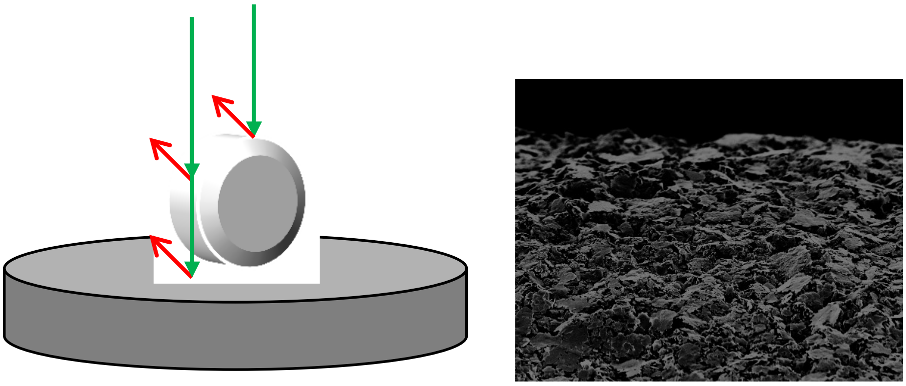

Figure 4.30 Auquiring of EDS data (a) Schematic depiction of EDS acquisition. Green arrows indicate excitation by the electron beam, red arrows emitted bremsstrahlung. Bulk and AgCl-coated wires were sampled at the centre of the wire to stray radiation. Data for epoxy coated wired had to beobtained towards the edge of the wire to obtain acceptable intensity of oxygen; (b) SEM image of detection area for EDS mapping as shown in Figure 4.32.

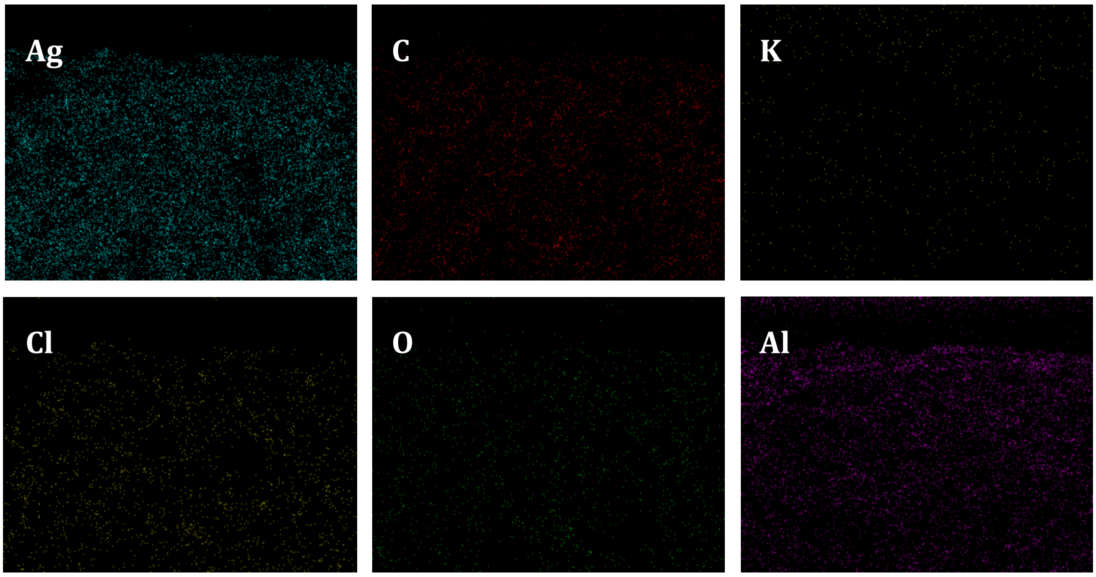

Figure 4.32 Distribution of elements on a epoxy-coated silver wire Silver, chlorine, carbon and oxygen mapping is well alligned with the sample position displayed in the previous figure. Potassium channel shows only weak singal with randon distribution, likely a result of background noise. Aluminum is well alligned with sample position as well, source unknown.

Despite the inconclusive results from the EDS measurements the electrodes were tested for their performance in experimental use. The offset compared to a regular AgCl-reference-electrode was measured by immersing both electrodes into a solution of 3M KCl and monitoring the offset potential over extended periods of time (Figure 4.31). In these tests the manufactured SSREs proved to be very stable. Potential offsets ranged between 5-20 mV and improved continuously as the manufacturing routine was standardized. Only minor drift was detected in the range of 2-3 mV over 20 hours or several microvolts within one hour. From these findings the SSREs were considered suitable for the measurements intended within this work.

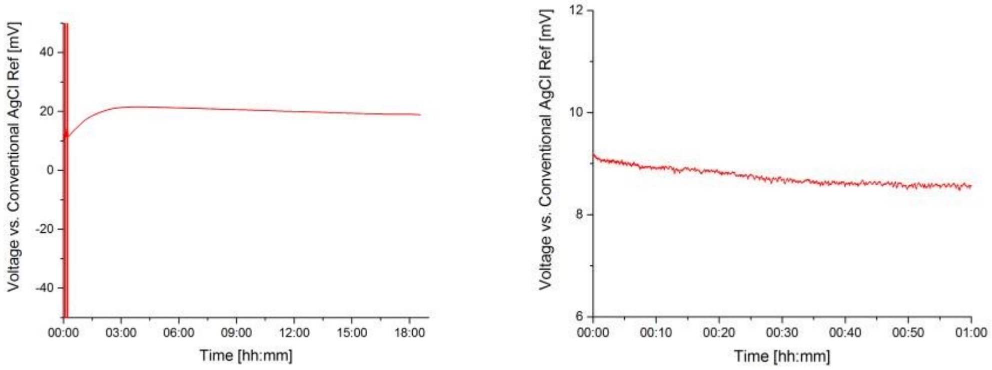

Figure 4.31 Stability tests of manufactured SSREs Voltage recorded between manufactured SSREs and a conventional reference electrode immersed in 3M KCl.

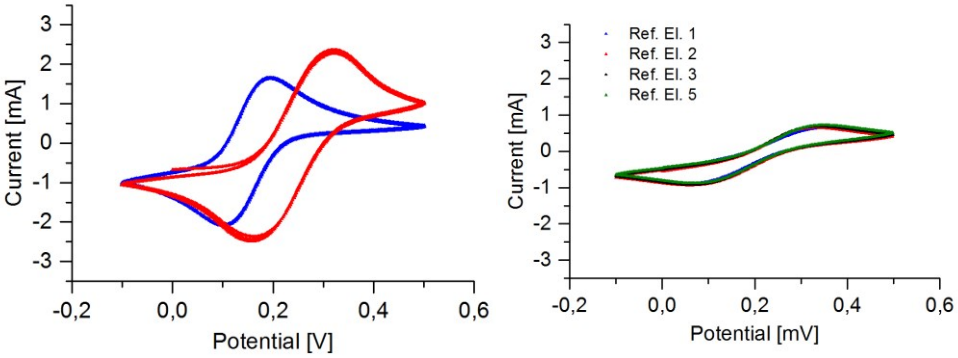

Figure 4.33 Cyclic voltammetry comparing SSREs to conventional (a) Comparison between manufactured SSRE (blue) vs. conventional AgCl-ref. electrode (red); (b) Test of of reproducibility between SSREs used with the same NEE sample

Comparative experiments between SSREs and conventional reference electrodes were also performed using cyclic voltammetry (Figure 4.33). Both electrodes show slightly dissimilar behaviour in various aspects.

Peak currents are lower and separation is smaller than for the SSRE. Peak separation of only 80 mV is a very good value (compared to theoretical 59 mV) indicating good performance of this reference. On the other hand the quotient between anodic and cathodic peak currents is 1,12 which is higher than the conventional electrode which only show minor deviation from the ideal value of 1.

The conventional reference electrode shows higher peak separation in slightly widened current traces. This may originate from a higher distance to the working electrode which could not be further reduced due to its bulk dimensions. This is also the reason why the use of the SSREs was tested and the results appear to support this argument. The observed current peak ration of 1,01 is almost ideal.

Table 4.3 Peak currents and potentials

		Ip	Ep	$\frac{I_a}{I_c}$	$E_a - E_c$
SSRE	**Anodic**	1,9 mA	0,19 V	1,12	0,08
	Cathodic	1,7 mA	0,11 V		
AgCl	**Anodic**	2,24 mA	0,31 V	1,01	0,14
	Cathodic	2,21 mA	0,17 V		

4.2 Generator Experiments

The initial experiments of this work were performed with an experimental setup that was disadvantageous for several reasons and therefore discontinued. The individual components and the changes made will be discussed below. Results from this initial setup as well as the newly developed measurement setup as outlined in the experimental section will be described.

4.2.1 Development of the Experimental Setup

4.2.1.1 Measurement Chamber Designs

Functional NEE surfaces were assembled into experimental chambers to be used in experiments with cells. The chamber had to fulfil several functions:

- Protection of the NEEs from moisture
- Providing a reservoir for cell culture medium
- Holding counter- and reference-electrode (when used)

Initial experiments were performed with an experimental chamber made of solid Teflon as depicted in Figure 4.34. The chamber was built from a bottom- plate and an upper body which were connected with four screws. The bottom plate featured a cavity of appropriate dimensions to hold the NEE-samples. The upper body had a cylindrical opening at the centre which confined the volume holding the cell culture medium. Two additional channels provided side access to this volume through which cell cultured medium was continuously perfused and removed at a

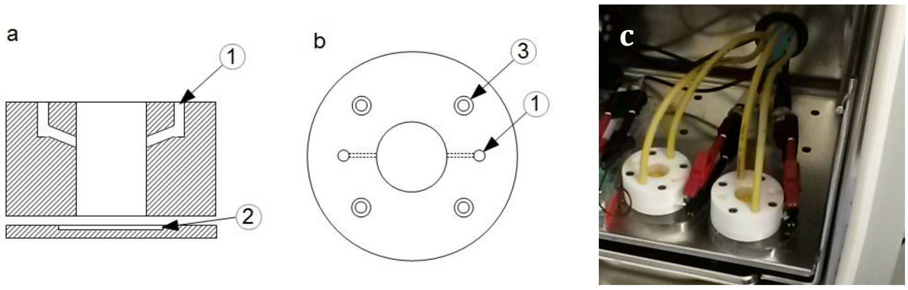

Figure 4.34 Initial Measurement chamber and setup (a) side and (b) top view of measurement chamber used in initial experiements. (1) Channels cut through the sides were used to hold the gold wire used as counter electrode and for perfusion of cell culture medium via a syringe pump. (2) Cavitiy in the bottom plate for the NEE surfaces. (3) Holes for screws connecting top and bottom part of the chamber. (c) Experimental chamber inside th cell culture incubator with attached tubes for media perfusion and crocodile clamps aside for connection to electronic circuitry.

constant flow rate. In addition the gold wire used as counter electrode for the electrical measurements was led through these channels. The use of this chamber was discontinued for the following reasons:

- Mechanical stress on the substrates when the connecting screws were attached often led to cracking of the samples rendering them unusable. In other cases mechanical failure occurred some time after the assembly as a result of additional tension built up from heating of the massive Teflon body to the incubator temperature of 37°C. If the screws were attached too lightly leakage occurred. Failure of the structural integrity of the substrate or (slow) leakage often could only be detected by erroneous readings and/or after disassembly forcing the experiment to be aborted.
- The cylindrical volume holding the cell culture medium was approximately 3 cm in height; therefore diffusion of CO_2 from the chamber atmosphere towards the cells was limited and very dissimilar to the situation in regular cell culture flasks.
- Medium perfusion required long tubing for connection to the syringe pump outside the chamber. The tubing required extensive cleaning and was found to be an additional source of contamination. Tubes had to be bent to connect to the chambers resulting in tension which may induce movement of the experimental chambers at random time point during experiments. Due to the volatile connections of NEEs and gold wire counter electrode this often resulted in faulty connections. In addition, the perfusion of a total volume of several tens of millilitres within 48-72 hours was found to be unnecessary.
- Gold wires of only 5 µm diameter used as counter electrodes were very problematic in handling. On many occasions the wire would break upon assembly into the channels or when the tubing for medium perfusion was attached or detached. The small diameter of the wire was also problematic when establishing contact to the measurement circuitry. Often loose contact occurred in the connection between crocodile clamp and gold wire.
- The incubator used in these experiments only had a small volume and no ventilation system. Although equipped with a water reservoir for providing a saturated humidity atmosphere, it was observed that it could take up to 10 hours for stable atmosphere in terms of temperature and humidity to be established.
- The use of a gold wire instead of a conventional reference electrode impeded the comparison of the measured potentials to other results published in literature. Electrochemical experiments could not be performed with only two electrodes available in this setup.

To overcome these disadvantages, various types of chambers were constructed and tested, ultimately leading to the development of the chamber construction presented in the experimental section above (Section 3.1.4). These intermediates were part of an evolutionary process leading to the design presented in the experimental section. The individual advantages of these development steps shall only discussed briefly pointing out the main findings paving the way towards the next chamber design.

First a “double chamber” was developed capable of holding two substrates of which one was used as counter electrode (Figure 4.35 b). This design replaced the problematic gold wire initially used by a glass substrate sputtered with bulk gold without functionalization. The chamber also featured holes in the bottom plate for transmission microscopy allowing observation of the cells on the substrate during or after the experiments without dismantling the entire chamber. Although avoiding the use of the thin gold wire was beneficial, this chamber was still constructed according to the same concept consisting of top and bottom part interconnected by screws. Therefore problems with sealing and rupture of substrates through mechanical stress prevailed. Electrical connection to the NEEs via the thin aluminium stripe was also problematic with this setup.

Next the integration of NEEs into standard laboratory six-well plates was tested (Figure 4.35 c, d). NEEs were placed at the bottom of the wells and copper wire was glued to the edge of the substrates to provide connection to electronic circuitry. Gold plated connector-pins were immersed in the cell culture medium through a hole in the lid of the plate, functioning as

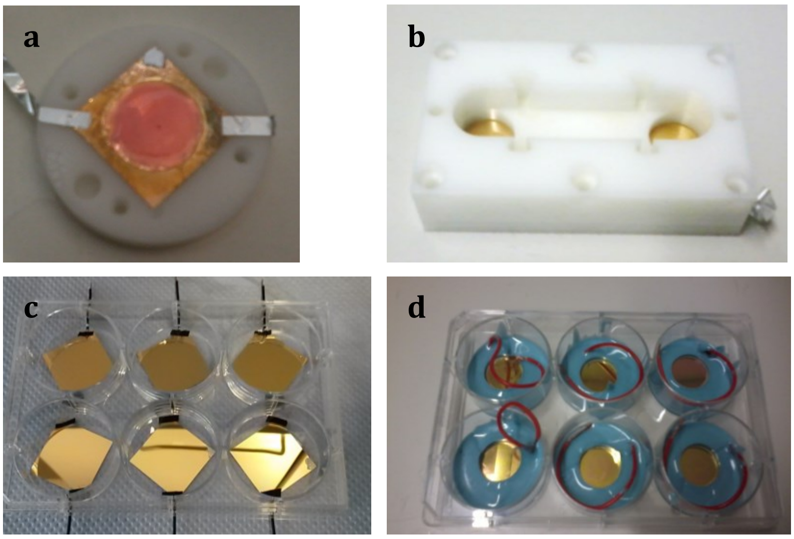

Figure 4.35 Various designs of experimental chambers (a) Bottom plate with NEE of the chamber used in initial experiments; (b) Double chamber for two substrates made of Teflon; (c) Bulk gold substrates in well plate with copper-wires attached; (d) well plates with substrates after sealing with Picodent.

counter-electrodes. These solutions replaced the volatile connections via aluminium-stripes and thin gold wire. The bottom of each well was covered with Picodent-silicon polymer to ensure only the functionalized surface area of the substrate came into contact with cell culture medium. To protect the functionalized surface area, hollow metal cylinders were placed to the substrates before the glue was poured into the well. The removal of these metal cylinders was found to be the biggest disadvantage of the concept as sheer forces and local mechanical stress on the substrate resulted in recurring damage to the polycarbonate insulation and/or thin metal films. Besides the risk of damaging the substrates during the processing, the six-well-experimental chambers were also disadvantageous in handling during the experiment, especially inside the small incubator. Due to close spacing of the wells and the counter-electrodes integrated to the lid, many cables for electrical connection had to be located in close proximity. When the lid was opened, e.g. for addition of cells, the electric circuit was disrupted disturbing the aspired continuous measurement.

From this experience the fourth generation of experimental chambers as described in the experimental section was developed. The use of single petri-dishes resolved issues of close proximity of the samples in the six-well plates. The Teflon ring glued to the substrate combined functionality of confining the experimental chamber volume and holding the counter- and reference-electrodes allowing the transition from two- to three-electrode-configuration. With the electrodes now integrated to the bottom part the lids could now be removed without inflicting the measurement process.

4.2.1.2 Multi-Channel Measurement / Electrical Setup

With the initial experimental setup the number of simultaneous experiments was limited to only two chambers by several factors:

- The perfusion system not being capable of supplying more than two chambers.
- The incubator providing only very limited space, especially in connection with the tubing system required for perfusion.
- Availability of expensive source-meter-units for electrical measurement

Limitations caused by the perfusion system could be overcome by omitting it from the setup. As already mentioned in the previous section, there was no requirement for perfusion. The amount of cell culture medium contained in the experimental chamber was more than enough within the experimental timeframe of up to three days.

Moving the experimental setup from the small bench-top incubator to a larger one with integrated ventilation provided improved conditions for cell growth and the required space for

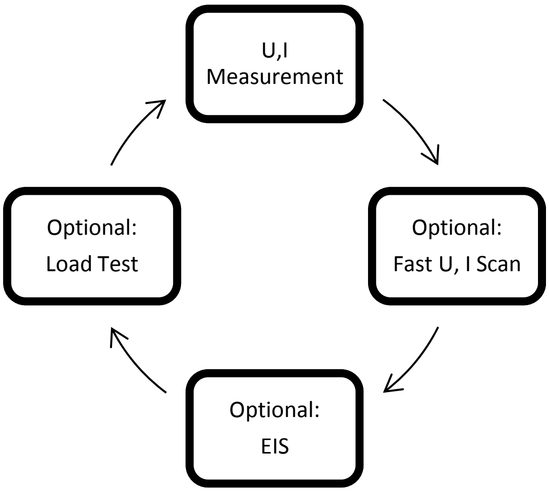

Figure 4.36 Flow Chart of automated measurement cycle Main function of the measurement program was the consecutive recording of voltage and current on all channels.

simultaneous work with up to ten samples. The ventilation system ensured much faster establishment of a homogeneous atmosphere in equilibrium with saturated humidity at the desired temperature and CO_2 levels.

The key component for multi-channel-measurements was the integration of a matrix-switch-unit (MUX) routing the connections of the measurement chambers to a variety of measurement devices. The switch matrix was controlled via a customized LabView program, which was designed to periodically take measurements from each of the connected chambers. It would run in a continuous cycle through all connected chambers until a defined time limit was reached or the measurement was terminated by the user. The voltage- and current-recording could be interrupted manually or at defined intervals to perform additional tasks like high-speed-measurements, electrochemical impedance spectroscopy or load testing. After completion of these additional tasks the UI-recording would resume.

The program was designed to give the user maximum control over all variables in the measurement. The number of chambers in the experiment can be chosen between one and ten. The program will only cycle through the defined number of chambers, thereby avoiding gaps in the recorded data. For each UI measurement-cycle the number of measurements per interval and acquisition rate can be defined.

When triggered the optional segment for fast measurements would temporarily reconfigure the measurement hardware for high acquisition speed. This function was meant to detect action potential from cells incubated on NEEs. Measurements were recorded at 10 kHz and stored in the internal buffer because data transfer to the PC was not capable of keeping up with measurement speed. The length of the scan was therefore limited by the size of the buffer holding up to 50k values. After the buffer was full, recorded data was transferred to the PC before the program would proceed with the next step.

In load experiments the capability of the source-meter-units to act as a current-sink was used to simulate an electrical consumer connected to the experimental chamber. The source-meter unit would determine the present voltage and current levels put out by the experimental chamber and would then dissipate a certain percentage of that power as defined by the user.

The only measurement option requiring additional manual operation was the interruption for electrochemical impedance spectroscopy. This program segment would connect the outputs of the experimental chambers to external connectors to the potentiostat for impedance measurements and request the user to trigger the impedance measurement for the selected chamber. These measurements needed to be separately triggered within the potentiostat's software which could not be interfaced with LabView. After acquisition of impedance the user would confirm this inside the LabView program which would then either connect the next chamber to the potentiostat or resume UI-measurement.

To ensure a continuous electrical circuit between the working- and counter-electrode, a 10 MΩ resistor was inserted into the circuit connecting both electrodes of each chamber while not being to the measurement devices and the integrated shunt resistor. This modification was added after first experiments with the MUX showed disturbing effects of charges built up on the chambers' electrodes in their off-time during the measurement cycle.

4.2.2 Culturing of NRK49F-cells on NEEs

General compatibility of NRK-49F cells towards NEE substrates was already documented in previous works. Therefore only a brief comparison between cells in standard cell culture dishes and cells were incubated on NEE substrates was conducted. Figure 4.37 shows cells grown on different substrates. All surfaces except regular cell culture dishes were pre-treated with poly-L-lysine to facilitate cell adhesion. In all samples typical behaviour with respect to adhesion, spreading and proliferation was observed qualitatively.

Time-lapse observation of cells on NEEs over extended periods of time confirmed these findings (Figure 4.38). Cells would readily move across the surface with well-defined filopodia specifically locating to sites of the nanowires. It appears that that these sites are somewhat preferential for cell adhesion. Processes of cell proliferation - detachment, cell division and reattachment - were also repeatedly observed repeatedly within the timespan of the experiment. If given enough time, cells grew to confluency just as in regular cell culture dishes. Therefore it may be assumed, that incubation on NEE-substrates does not pose any adverse effects towards cell viability.

Future investigations should look more closely into the precise mechanism of cell adhesion and the formation of focal adhesions at the electrode site and subsequent effects of cell velocity, proliferation and the organization of the actin cytoskeleton.

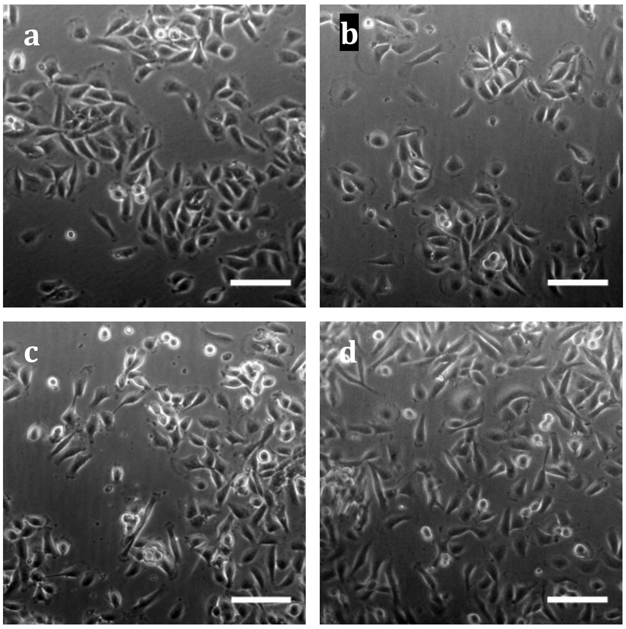

Figure 4.37 NRK49F cells on various substrates (a) standard six-well plate; (b) bulk gold surface; (c) NEE without polycyrbonate insulation; (d) NEE as used in experiments; all surfaces except six-well treated with PLL prior to cell seeding. Scalebars are 100 µm.

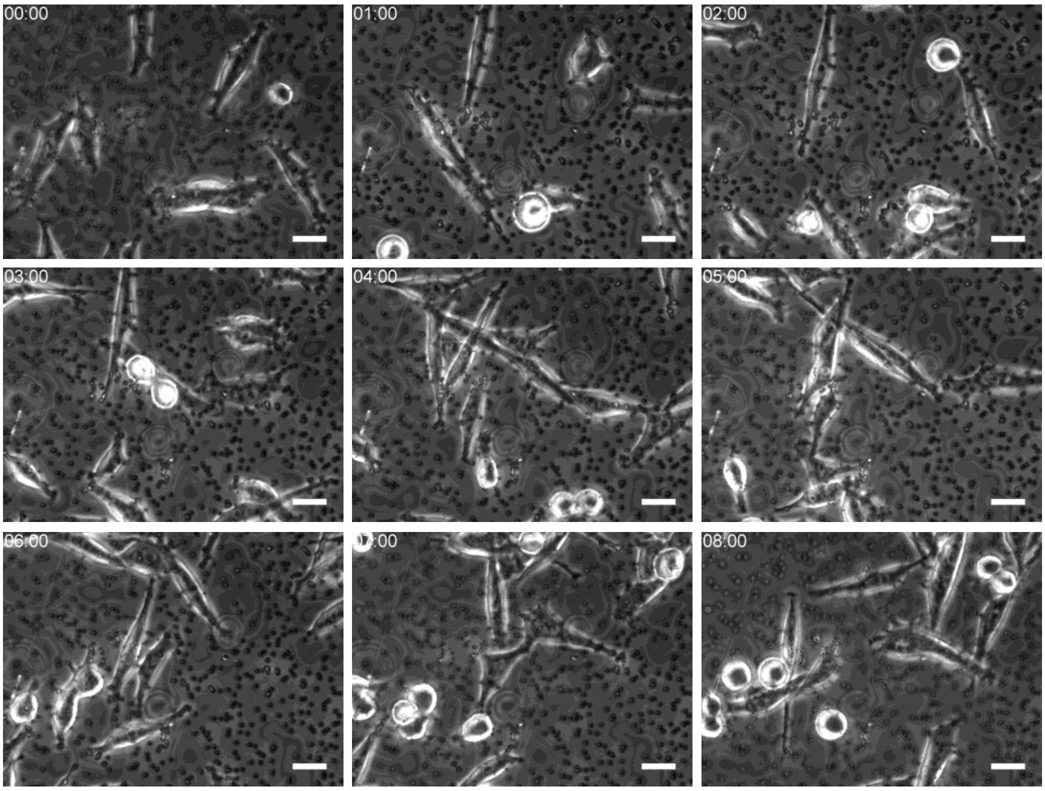

Figure 4.38 Long-term observation of cell spreading on a NEE Cells incubated on NEE at 40x magnification. Scale bars are 20 µm. Black dots are identified as locations of nanoelectrodes. Cells readily reside on nanoelectrodes and filopodia seem to specifically adhere to nanowire sites.

4.2.3 Electrical Measurements

The ultimate aim of this study was to establish a stable interface between living cells and the vertical nanowires of the NEEs, suitable for measurement of electric activity of the cells. NEEs were assembled into experimental chambers as previously described and placed inside a cell culture incubator equipped with electrical wires for connection to the matrix switch unit.

Voltage and current recording was started after all samples were placed inside the incubator and filled with cell culture medium. Usually no cells were added right from the start as it was observed that the chambers needed several hours to reach a steady state. Most likely this drift is the result of adsorption-processes at the gold nanowires. After the chambers had equilibrated cells were added to the chambers.

4.2.3.1 Measurements with conventional two electrode setup

Initial experiments were performed still using with NEEs integrated to the Teflon chambers. After assembly of the chambers and treatment of the surfaces with poly-L-lysine, they were placed inside the incubator, filled with cell culture medium and connected to the electronic circuitry and perfusion system. Voltage recording was then initiated after the incubator was closed without cells added to the chamber yet. This first stage of recording shall be referred to as “phase I” and was used to determine the offset voltage for the individual chambers, which would vary for almost any experiment performed with this setup. Within a few hours the recorded voltage would settle to a certain value, typically several few to tens of millivolts above or below zero. In the ideal case, NEEs of similar structure were expected to exhibit similar offset values like in the experiment displayed in Figure 4.39. The beginning of Phase II was initiated by

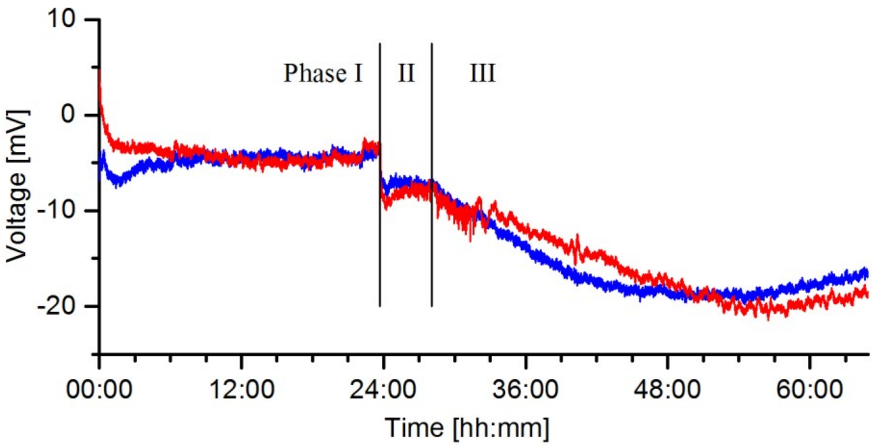

Figure 4.39 Voltage measurement with conventional two electrode setup NEEs with 100µm nanowires were allowed to equilibrate for ~22 h before cells were added (phase I). Voltage drop observed in phase II results from the addition of cells. During phase III adherent cells grow to confluency.

the addition of cells to the equilibrated chambers, resulting in an immediate leap of the detected voltage, usually slightly towards more negative potential. After this leap the potential would settle to a value slightly lower than before the addition. During this phase the cells added to the experimental chamber would sediment to the NEE surface and begin to adhere. Phase III begins 4-6 hours after addition of the cells when the voltage decreased further towards more negative potential. During this stage the cells fully adhered to the surface would proliferate until a confluent cell layer was formed on the NEEs. In some experiments the voltage would remain constant at this level for several hours, while in others it decreased gradually after reaching the maximum value.

The initial offset voltage before addition of the cells as well as the magnitude of the potential drop upon cell adhesion to the NEE were subject to great variations in all experiments performed with this setup. The experiment displayed in Figure 4.39 represents the rare example of both NEEs used in the experiment showing very similar behaviour throughout the time of recording.

4.2.3.2 Comparison of bulk gold electrodes and NEEs with cells

To proof the correlation of the measured signals to the nanowires present at the NEE surfaces, the performance of polycarbonate-coated bulk gold electrodes was tested in conjunction with cells. Bulk gold electrodes were spin-coated and etched similar to NEEs and assembled into experimental chambers. The overall signal showed more noise than in measurements with

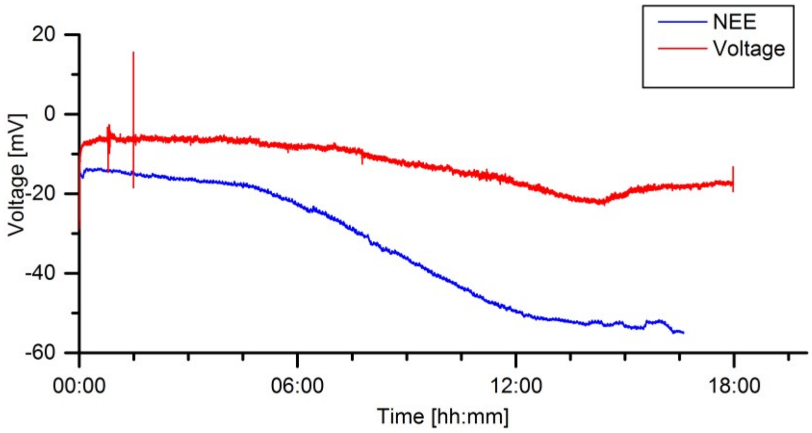

Figure 4.40 Voltage measurement with NRK49F cells on PC-coated bulk gold electrodes and NEEs Measuerement started with addition of the cells. NEEs (blue) in this experiment show the characteristic increase in potential towards more negative values upon cell adhesion while insulated gold electrodes show only minor response upon incubation with cells (red). The chracteristic decay of the potential typical with NEEs is not observed.

NEEs, which results from the increased capacitance of the insulated electrode. As the cells adhere to the polycarbonate surface and form a confluent layer, a slight tendency towards negative potential was observed in this experiment as well, but not anywhere near the magnitude that was observed in experiments with NEEs.

4.2.3.3 Influence of cell adhesion /deprivation of serum

As discussed in the theoretical section, penetration of nanowires into living cells is more likely to occur as a result of forces induced by cell adhesion to the surface. In order to test the influence of cell adhesion on the measured potentials, cells were incubated on NEE surfaces without fetal bovine serum (FBS) added to the cell culture medium. NRK-cells grown on NEEs (or any other surface) without addition of serum to the cell culture medium do not adhere due to the absence of required growth factors. This behaviour was confirmed by observation of cells in regular cell culture dishes. Without serum added to the culture medium cells would sediment to the surface of the dish and remain in in a rounded up state, typical for cells in suspension. Cells would readily move as a result of externally induced movement of the medium indicating the absence of any adhesion. Upon addition of serum, cells adhered and transition to typical morphology was observed within few hours.

The same experiment was performed in the electrical measurement setup. In accordance with these observations under cell culture conditions, no change in measured voltage was observed when cells were seeded on NEEs in absence of FBS (Figure 4.41). When adhesion was triggered by addition of FBS, cells readily adhered to the surface resulting in the previously observed rapid change of the potential towards more negative values. This change would occur more even more rapidly than observed in previous experiments without initial deprivation. Although direct observation of the adhesion process was not possible in this case, because the experiments were

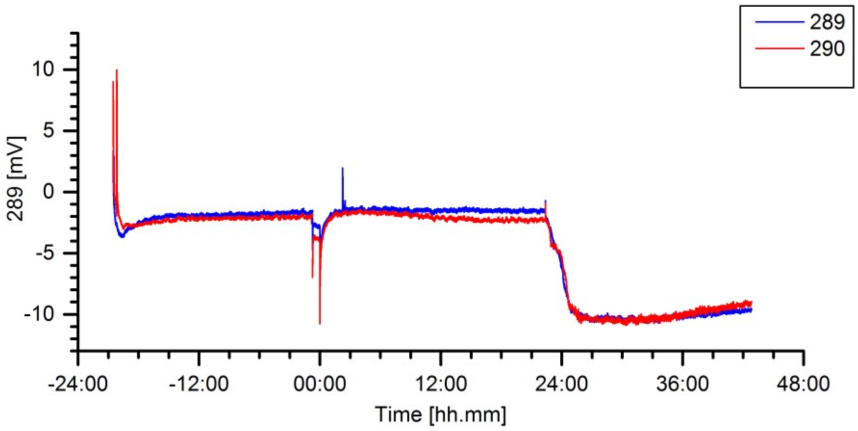

Figure 4.41 Influence of cell adhesion on measured potential changes NEEs were first allowed to equillibrate, then cells were under deprivation of serum. No change of the potential is observed.

performed with the Teflon chambers in which there was no optical observation possible. Considering the an adhesion-dependent mechanism for the penetration of nanowires into cell as postulated by Melosh et al. it appears likely, that this is also the case in this experiment. Further experiments combining electrical measurements and optical observation under a microscope could provide additional confirmation of this correlation.

4.2.3.4 Voltage Measurements with Three Electrode Configuration

After various alterations of the measurement setup were implemented (as mentioned above), voltage and current measurements with cells on NEEs were performed using the three electrode configuration. For the experiment shown in Figure 4.42, eight identical NEE samples with nanowires of 100 nm diameter and 1,5 µm height were assembled into experimental chambers and placed inside the cell culture incubator. In addition to voltage and current recording, EIS

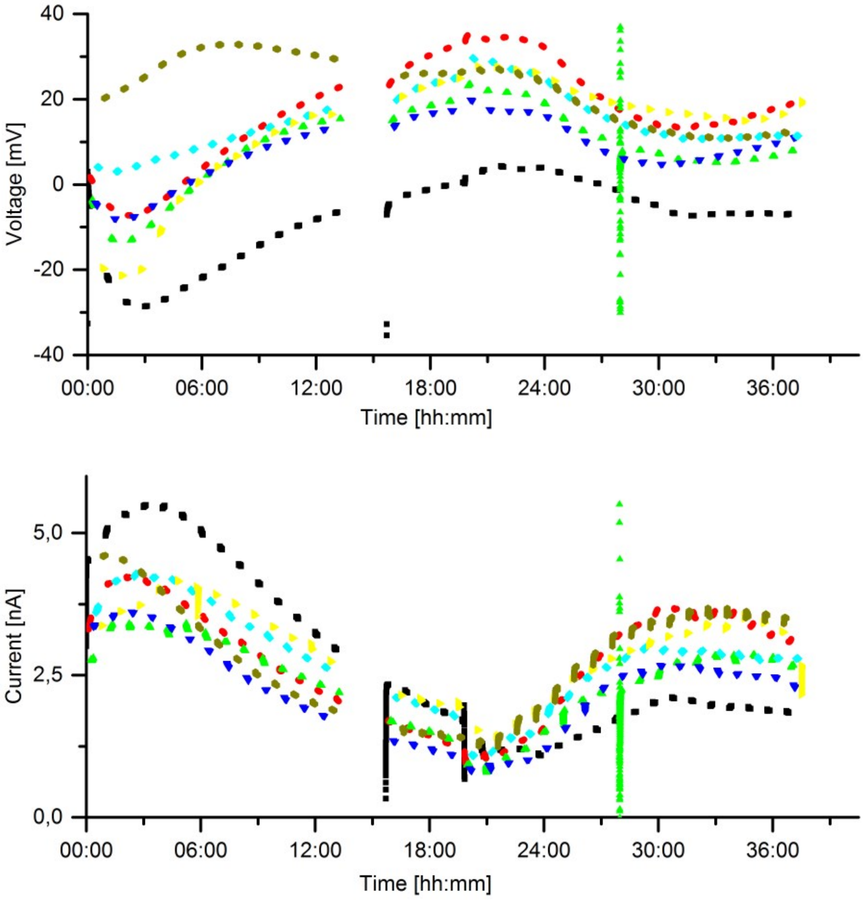

Figure 4.42 Voltage and Current Measurement with cells on 100 nm NEEs NEEs with 100 nm naowires of 1,5 µm in lengh were usedd in this experiment. Voltage recording was started without cells added to the chamber. After 14 h recording was interrupted for EIS measurements. After recording was continued, cells were added to the chambers 19 h after the beginning of the experiment.

spectra were measured at different time points for all chambers using the interrupt option in the LabView program. Results from these EIS measurements will be discussed below in section 4.2.3.7.

Again first the behaviour of the chambers was observed without cells added. The results shown in Figure 4.42 only show seven plots because one chamber provided erroneous data, likely due to insufficient electrical contact. Here the voltage did not settle to a constant value but was rather subject to a continuous drift, unlike measurements in two electrode configuration. This drift towards more positive potential set in approximately 3 h into the experiment. Despite the absence of cells on the NEEs, rather large currents were detected during these first hours of the experiment. The highest currents were detected 3 hours into the experiment, after this time point a continuous decline towards zero was detected with all samples. The interruption of the measurement for impedance spectroscopy did not have an influence on these trends in both current and voltage recording.

When cells were added after 19 hours, no change was observed in the voltage signals, but the current dropped to a value of only ~ 1 nA as an immediate response to the addition. The exact reason for this is unknown, but it may be caused by blocking of the electrodes as cells sediment to the surface. Within an hour after the cells were added, the current slowly begins to increase. This increase stops about 12h after the addition of cells when all channels reach a maximum value of current, which remains constant for the rest of the experiment. Voltage recording displays a drop towards more negative potentials about 6 h after the cells were seeded which occurs simultaneously in all channels. This trend continuous until 12h after the addition of cells. At the same time when the current recording reached its maximum value, the voltage drop ends

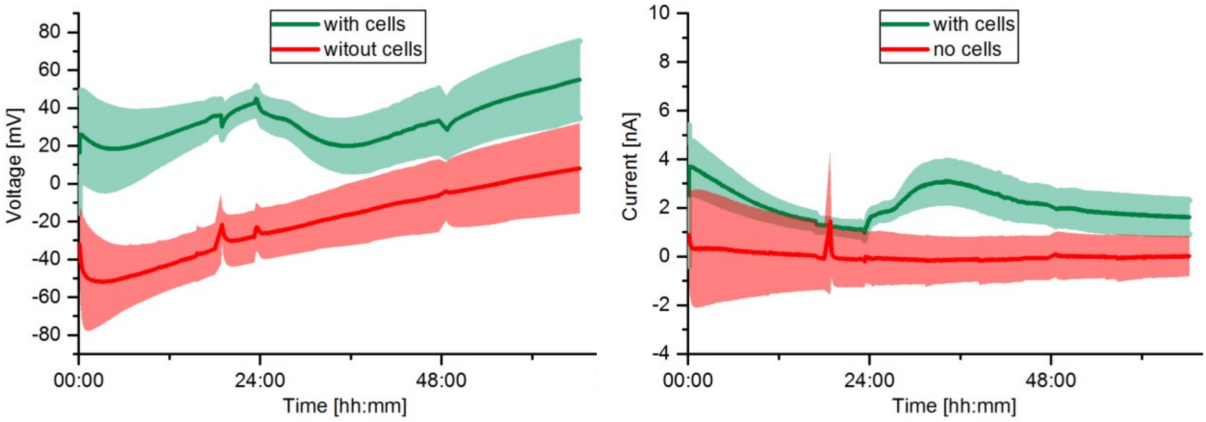

Figure 4.43 Voltage and current recorded from NEEs with/without cells seeded

Before addition of cells all samples show the same drift towards positive potential. Cell addition after 24h to some of the samples results in the previously observed potential-drop and increase in current, while no response is detected in samples without cells and drift towards positive values sets in again.

The overall appearance of the voltage recording is in accordance with the results of previous experiments conducted with two-electrode configuration. The potential drop upon adhesion of the cells to the NEE surface within a few hours after the addition of cells is very similar to previous observations, although the continuous drift of the chambers must be considered rather unfavourable. If the drift was removed by baseline subtraction, the similarity of the results obtained in two-electrode configuration with the Teflon-chambers becomes even more obvious. The improved homogeneity of the samples used in this experiment is resembled by the mostly uniform response of all measured samples. Five out of seven samples show a very uniform response.

To confirm that the measured changes of voltage and current correlate to the presence of cells on the NEEs, another experiment was performed in which only few NEEs were incubated with cells (Figure 4.43). No relevant changes of potential or current were observed with samples without cell. The different offset of samples with and without cells seen in the voltage plot is a random artefact resulting from the deviations continuously present within samples of the same type. Nevertheless less despite the different offset and drift behaviour, the response resulting from incubation of the NEEs with cells is clearly detectable in the measurements. The fact that surfaces incubated with and without show different offsets in the initial stage of the experiment without cells added yet is of random nature and was not expected. Despite these deviations the absence of any response in the samples without cells provides another indication of the desired interaction between the manufactured NEEs and cells incubated on them.

4.2.3.5 Influence of electrode length

The aspect ratio of nanowires is a decisive factor for successful intracellular access of such structures. Therefore NEEs with nanowires of different length were compared in experiments with cells. Electrodes between 1,4 and 1,8 µm height were used in this experiment (Figure 4.44). Similar to previous experiments, the chambers were first allowed to settle over a period of 24 h before cells were added. Upon addition of the cells the voltage drops observed for the different electrode length is of the same magnitude for all samples. Therefore no conclusion regarding the length of the electrodes could be drawn from this experiment. Of course the variation of electrode length in this experiment is rather small, but the used samples were chosen in accordance with other publications, where common length of the nanowires varies between 1,5 - 2 µm. Below 1,5 µm the aspect ratio is too low to expect intracellular access, length of more than 2 µm increase the tension on the cellular membrane and thereby the chance of penetration through the cell.

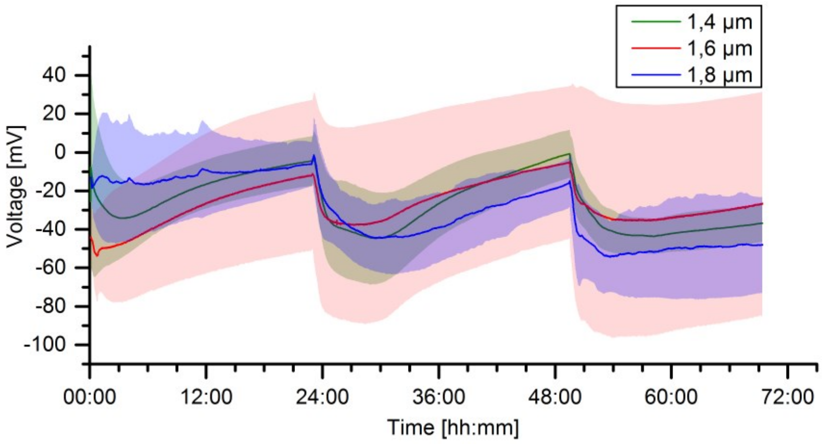

Figure 4.44 Influence of electrode length on measured voltages 100 nm NEEs of different length were observed with and without cells added. No significant influence of the length was observed in this experiment.

4.2.3.6 Experiments with electrodes of different diameters

With the diameter being the second most important parameter for the cell-nanowire interaction, the results of experiments with cells on substrates with nanowires of different diameters were compared. NEEs with nanowires of different diameters were tested according to the standard experimental protocol. During measurement without cells added to the chambers a trend towards higher offset values for nanowires of larger diameter became obvious similarly, the offset current was increased for the 400 nm nanowires, while the response for 200 nm and 400 nm wires was more or less the same. For both voltage and current the observed trends prevailed after the addition of cells: The magnitude of the common potential drop after the addition of the cells increases with the diameter of the nanowires and so does the detected current. These effects may result from increased surface area of the larger wires as well as their lower impedance.

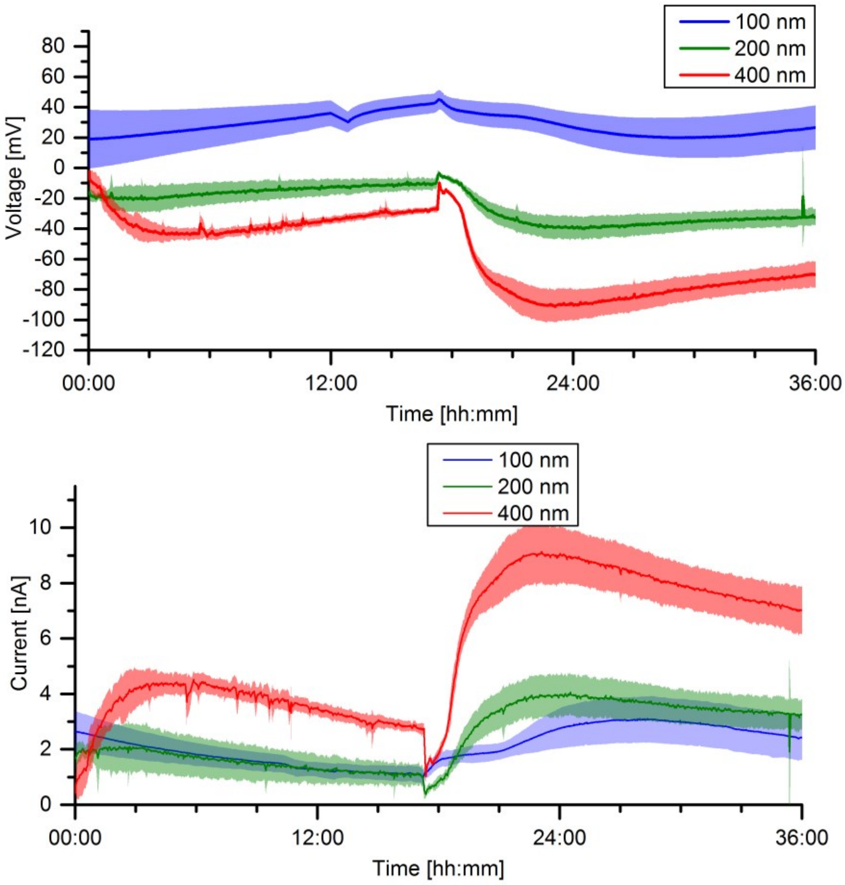

Figure 4.45 Influence of nanowire-diameter on the measured voltage The results show a clear tendency towards higher amplitude of the detected potential changes as well as the current detected from nanowires of larger diameter.

4.2.3.7 EIS with NEEs

Impedance spectroscopy was performed in four different time points during this experiment (Figure 4.46):

(i) With the NEE in its initial state.

(ii) After coating with poly-L-lysine.

(iii) 14 hours into the experiment before addition of the cells.

(iv) 19 hours after the addition of cells.

The idea was to establish this method as a tool to evaluate the properties of individual NEEs before and during experiments. Eventually the data obtained from these measurements would show a correlation between the voltage and current measurements and the impedance data. In the ideal case equivalent circuit modelling was hoped to resolve the interaction between the nanowires and the cells adhered to them as outlined in the previous section.

Measurements of the impedance for each sample in its initial state should provide a reference for the following measurements. Next the influence of poly-L-lysine coating for adhesive support was tested. Measurements before the addition of cells was expected to reveal alteration resulting from interaction of the NEEs with the cell culture medium. Finally measurements were performed at the end of the experiment when a confluent layer of cells was formed at the NEE surface.

In Figure 4.46 the impedance magnitude and phase are summarized for one of the samples at the four time points previously described. Unfortunately the results obtained in these experiments do not allow making any conclusions with regard to the above mentioned aims.

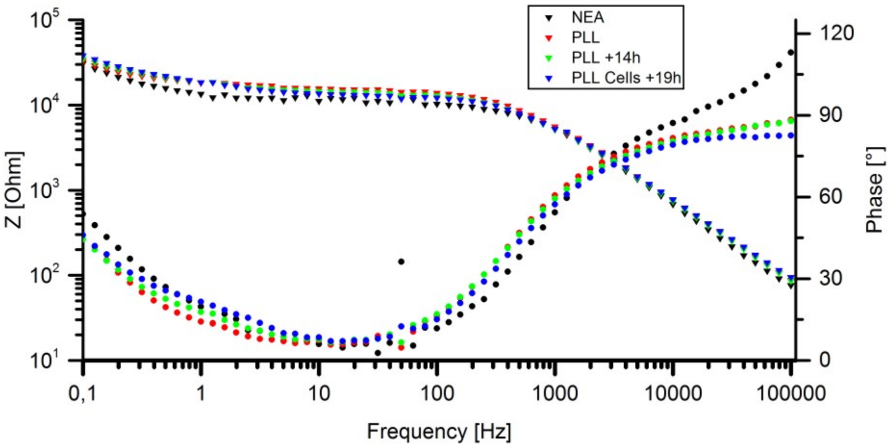

Figure 4.46 Impedance Magnitude and Phase of an NEE during voltage measurement with cells No signicicant differences were observed during an experiment with cells on nanowires.The impedance of the nanowires themselves is too large and superimposes on effects possibly caused by the cells.

The differences between results are too small (and within measurement error rage) to draw any conclusions from them, neither qualitatively nor quantitatively as the data was almost identical at all four time points. Interaction of the NEEs with the cells cannot be resolved from the obtained data, because overall impedance of the NEEs is too large compared to the contribution of the current passing through the nanowires and cells incubated on them. Experiments similar to the one presented in Figure 4.46 were performed with nanowires of all diameters, but in no case additional information about the cells-substrate interaction could be derived from these measurements.

5 Summary

The idea behind this project was the development of a platform, which allows parallel electrical contacting of large cell numbers. For this purpose, the concept for manufacturing vertical nanowires on top of a common electrode was pursued. The concept included an insulating layer separating the common electrode at the bottom from the cells on top of the nanowires. Thereby short circuiting of the cells should be avoided. Cells incubated on top of these surfaces were expected to internalize the nanowires protruding from the surface and thereby establish electrical contact. While only miniscule amounts of currents are detected in conventional electrophysiological experiments, significantly larger currents were expected due to the concept of parallelisation. In the ideal case the system would provide enough current to function as a "bio-generator", allowing the harvesting of electrical power *in vivo*.

Progress towards the realization of this bio-generator was very slow in the initial stages of this work, mostly for two reasons:

(i) Very low yield of the preparation process for the nanoelectrode-ensembles:
  Samples would suffer from insufficient adhesion of the conductive film, inhomogeneous growth of nanowires and insufficient understanding of the spin-coating and etching processes.

(ii) Limited capacity for electrical measurements:
  The setup used early into this work only allowed for the simultaneous measurement of two samples. With experiments lasting 48 hours and longer, only little amounts of data could be obtained. The above mentioned deficits in sample quality and the resulting variations in the measurements made interpretation of the obtained results even more difficult.

For these reasons, both issues were addressed by the work presented in this thesis.

For the manufacturing of nanoelectrode-surfaces, a detailed revision of all process-steps was performed, because severe quality issues prevailed following the initially provided protocols. These circumstances rendered a systematic evaluation of the cell-nanoelectrode interface virtually impossible and required intensive study of each manufacturing step.

The hazardous cleaning procedure for glass coverslips involving caroic acid was found to be unnecessary and therefore replaced by sonication of the glasses supporting the nanowire surfaces. Investigation of the sputtering processes revealed, that the old protocol for sputtering of titanium came short of a sufficient removal of the passivating oxide layer formed on target. A sufficient removal of this passivation layer was only observed after sputtering at 120 mA for 15 minutes with the shutter closed and was therefore implemented as standard procedure in the manufacturing protocol. Issues with insufficient adhesion were resolved by this modification.

SEM and AFM studies of gold films revealed variations in surface morphology of sputtered gold, depending on the current used in the process. Samples prepared at lower currents showed a more inhomogeneous structure involving percolating islands of gold instead of a homogeneous film. Experiments of growing nanoelectrodes on gold surfaces prepared at different currents showed full coverage with nanoelectrodes on these inhomogeneous surfaces, while barely a few nanoelectrodes were observed on homogeneous samples prepared at higher currents. Gold sputtering current for nanoelectrode fabrication was therefore reduced to 30 mA. Only after these revisions of the sputtering process, surfaces with quantitative coverage of nanoelectrodes were obtained.

Nanoelectrodes were also manufactured successfully on larger glass substrates, after a sputtering process accounting for their larger dimensions was established. New protocols for electrodeposition and spin-coating of these larger substrates successfully implemented. The advantage of these efforts was the utilization of almost the entire membrane area, producing much larger surfaces of nanoelectrodes, which could be split into four of nine separate samples after removal of the template. Therefore process time and costs could be saved while providing several identical samples in just one step.

The spin-coating process was only studied empirically before; the actual thickness of the obtained polycarbonate film was unknown. The thickness of spin-coated polycarbonate films was determined for different spin speeds. It was found, that the film thickness at 1200 rpm was approximately 500 µm resembling the desired value. When smaller tiles obtained from large-scale deposition were used at later stages of the project, similar thicknesses were achieved on these surfaces. The injected volume of polycarbonate solution was adjusted proportionally to the reduction in surface area of the sample to be coated.

The review of the etching process with cyclic voltammetry revealed, that higher currents were detected from nanoelectrode ensembles after prolonged etching times. Accordingly, the etching time was extended from 20 minutes to 1h.

With all these measures combined, a completely revised protocol for the manufacturing of NEEs was compiled, allowing for more efficient manufacturing of samples. These significant improvements in sample preparation were also resembled by the results of voltage measurements with cells. Experiments as presented in Figure 4.39 were only possible with samples of homogeneous quality obtained from the revised manufacturing process.

The construction of new experimental chambers for the integration of NEEs into the measurement environment further improved the scope of possible experiments and the quality of the obtained results. Implementation of a three-electrode configuration in the chambers enabled electrochemical experiments like cyclic voltammetry and impedance spectroscopy under cell culture conditions, which were not possible before. A protocol for the manufacturing solid-state reference electrodes required for the three-electrode configuration was developed from scratch. The performance of these electrodes in comparison to regular Ag/AgCl electrodes was successfully demonstrated by comparative CV experiments.

Electrochemical impedance spectroscopy and cyclic voltammetry were used to gain insight into the manufacturing process and the electrochemical performance of the NEEs used in this work. Both methods were applied during all stages of the manufacturing process. The impedance data from samples before and after spin-coating of the insulating layer was successfully matched by equivalent circuit modelling. Unfortunately attempts of modelling the behaviour of nanoelectrodes after etching were not successful, due to the increasing complexity of the obtained spectra. Although changes of magnitude and phase were clearly detectable upon etching, the deviations were rather large for all three diameters of nanowires tested in this work. A similar picture was encountered in results from cyclic voltammetry. Although a clear trend towards higher currents after prolonged periods of etching was repeatedly observed for individual samples, the overall variation was high and within the same range, independently of electrode height or diameter. Therefore no conclusion towards the influence of these parameters could be drawn from those experiments. It may be concluded, that despite all efforts taken towards the improvement of the manufacturing processes, the choice of spin-coated polycarbonate as insulating film may be not ideal. Future work on this platform may explore the use of different materials and etching processes, e.g sputtered aluminium oxide as dielectric insulator and plasma etching. Automated processing is likely to provide superior and more reproducible results compared to manual spin-coating and etching.

Throughput in experiments with cells incubated on NEEs was increased by the construction of a new measurement environment. A matrix switch unit in combination with a cell culture incubator of appropriate dimension increased the number of simultaneous experiments up to ten. Specific programs were developed for variable control of acquisition parameters, also allowing simultaneous impedance spectroscopy on NEEs incubated with cells.

Voltage and current measurements with cells in this setup again demonstrated of the previous improvements in surface quality. Results obtained from samples of similar properties were at least to some extend reproducible, which was demonstrated by comparative experiments with nanowires of different diameter. The deviations measured for similar samples may result from variations of the insulating layer, but this hypothesis is currently not supported by any data. The continuous drift observed in voltage measurements was omnipresent in the work with setup and should be addressed in future studies.

If the present deficits of the platform can be resolved, it may provide an interesting alternative for certain aspects of electrophysiological research. Experiments with different cell types, like cardiac muscle cells or neurons, may provide interesting results, which allow better comparison to other studies. Given the many variables that were explored in the course of this work, the cell type was not changed to maintain coherence of the results within the project. Electrode arrays with individually addressable nanowires, fabricated with CMOS technology may be superior in many aspects. Yet this platform may be valuable for certain applications, like the originally intended bio-generator. Its manufacturing is rather cheap and does not require clean rooms and other expensive equipment.

6 Appendix

6.1 References

1. Destexhe, A.B., R., *Intracellular Recording*, in *Handbook of Neuronal Activity Measurement*, A.B. Destexhe, R., Editor. 2012, Cambridge University Press.

2. Verkhratsky, A. and V. Parpura, *History of electrophysiology and the patch clamp.* Methods Mol Biol, 2014. **1183**: p. 1-19.

3. Verkhratsky, A., O.A. Krishtal, and O.H. Petersen, *From Galvani to patch clamp: the development of electrophysiology.* Pflugers Arch, 2006. **453**(3): p. 233-47.

4. Hierlemann, A., et al., *Growing Cells atop Microelectronic Chips: Interfaceing Electrogenic Cells In Vitro With CMOS-Based MIcroelectronic Arrays.* Proceedings of the IEEE, 2010. **99**(2): p. 252-284.

5. Liu, Q., et al., *Cell-based biosensors and their application in biomedicine.* Chem Rev, 2014. **114**(12): p. 6423-61.

6. Zhou, W., X. Dai, and C.M. Lieber, *Advances in nanowire bioelectronics.* Rep Prog Phys, 2017. **80**(1): p. 016701.

7. Karimian, N., L.M. Moretto, and P. Ugo, *Nanobiosensing with Arrays and Ensembles of Nanoelectrodes.* Sensors (Basel), 2017. **17**(1).

8. Rettinger, J., S. Schwarz, and W. Schwarz, *Electrophysiology*. 2016, Springer.

9. Sonocchia, S., *Scribinii Largi Compositions*. 1983, Leipzig: Teubner.

10. Walsh, J. and S. Seignette, *Of the Electric Property of the Torpedo. In a Letter from John Walsh, Esq; F. R. S. to Benjamin Franklin, Esq; LL.D., F. R. S., Ac. R. Par. Soc. Ext., &c.* Philosophical Transactions of the Royal Society of London, 1773. **63**(0): p. 461-480.

11. Mauro, A., *The role of the Voltaic pile in the Galvani-Volta controversy concerning animal vs. metallic electricity.* J Hist Med Allied Sci, 1969. **24**(2): p. 140-50.

12. Volta, A., *On the Electricity Excited by the Mere Contact of Conducting Substances of Different Kinds.* Phil. Trans. R. Soc., 1800. **90**: p. 403-431.

13. Loeb, J., *The Recent Development of Biology.* Science, 1904. **20**(519): p. 777-86.

14. Loeb, J., *The Dynamics of Living Matter*, in *Columbia University Biological Series*, H.F. Osborn and F. Wilson, Editors. 1906, Columbia University Press.

15. Bernstein, J., *Ueber den zeitlichen Verlauf der negativen Schwankungen des Nervensystems.* Pfuegers Archiv Eur. J. of Physiol., 1868. **94**(4): p. 1133-1134.

16. Bernstein, J., *Elektrobiologie*. Die Wissenschaft. 1912, Braunschweig: Vieweg.

17. Cole, K.S. and H.J. Curtis, *ELECTRIC IMPEDANCE OF THE SQUID GIANT AXON DURING ACTIVITY.* The Journal of General Physiology, 1939. **22**(5): p. 649-670.

18. Cole, K.S., *Dynamic Electrical Characteristics of the Squid Axon Membrane.* Archives Des Sciences Physiologiques, 1949. **3**(2): p. 253-258.

19. Sakmann, B. and E. Neher, *Single-Channel Recording 2nd Edition*. 2nd ed. 1995, New York: Springer.

20. Sigworth, F.J. and E. Neher, *Single Na+ channel currents observed in cultured rat muscle cells.* Nature, 1980. **287**: p. 447.

21. Thomas, C.A., et al., *A miniature microelectrode array to monitor the bioelectric activity of cultured cells.* Experimental Cell Research, 1972. **74**(1): p. 61-66.

22. Fromherz, P., *Three levels of neuroelectronic interfacing: silicon chips with ion channels, nerve cells, and brain tissue.* Ann N Y Acad Sci, 2006. **1093**: p. 143-60.

23. Fromherz, P., et al., *A NEURON-SILICON JUNCTION - A RETZIUS CELL OF THE LEECH ON AN INSULATED-GATE FIELD-EFFECT TRANSISTOR.* Science, 1991. **252**(5010): p. 1290-1293.

24. Eversmann, B., et al., *A 128x128 CMOS biosensor array for extracellular recording of neural activity.* Ieee Journal of Solid-State Circuits, 2003. **38**(12): p. 2306-2317.

25. Giaever, I. and C.R. Keese, *Micromotion of mammalian cells measured electrically.* Proc Natl Acad Sci U S A, 1991. **88**(17): p. 7896-900.

26. Giaever, I. and C.R. Keese, *A morphological biosensor for mammalian cells.* Nature, 1993. **366**(6455): p. 591-2.

27. Giaever, I. and C.R. Keese, *Monitoring fibroblast behavior in tissue culture with an applied electric field.* Proc Natl Acad Sci U S A, 1984. **81**(12): p. 3761-4.

28. Wegener, J., C.R. Keese, and I. Giaever, *Electric cell-substrate impedance sensing (ECIS) as a noninvasive means to monitor the kinetics of cell spreading to artificial surfaces.* Experimental Cell Research, 2000. **259**(1): p. 158-166.

29. Kim, W., et al., *Interfacing silicon nanowires with mammalian cells.* Journal of the American Chemical Society, 2007. **129**(23): p. 7228-+.

30. Hai, A., et al., *Changing gears from chemical adhesion of cells to flat substrata toward engulfment of micro-protrusions by active mechanisms.* J Neural Eng, 2009. **6**(6): p. 066009.

31. Hai, A., J. Shappir, and M.E. Spira, *In-cell recordings by extracellular microelectrodes.* Nat Meth, 2010. **7**(3): p. 200-202.

32. Hai, A., J. Shappir, and M.E. Spira, *Long-term, multisite, parallel, in-cell recording and stimulation by an array of extracellular microelectrodes.* J Neurophysiol, 2010. **104**(1): p. 559-68.

33. Zhang, A. and C.M. Lieber, *Nano-Bioelectronics.* Chem Rev, 2016. **116**(1): p. 215-57.

34. Spira, M.E. and A. Hai, *Multi-electrode array technologies for neuroscience and cardiology.* Nat Nanotechnol, 2013. **8**(2): p. 83-94.

35. Chiappini, C., *Nanoneedle-Based Sensing in Biological Systems.* ACS Sens, 2017. **2**(8): p. 1086-1102.

36. Simon, D.T., et al., *Organic Bioelectronics: Bridging the Signaling Gap between Biology and Technology.* Chem Rev, 2016. **116**(21): p. 13009-13041.

37. Robinson, J.T., M. Jorgolli, and H. Park, *Nanowire electrodes for high-density stimulation and measurement of neural circuits.* Front Neural Circuits, 2013. **7**: p. 38.

38. Oja, S.M., M. Wood, and B. Zhang, *Nanoscale electrochemistry.* Anal Chem, 2013. **85**(2): p. 473-86.

39. Cox, J.T. and B. Zhang, *Nanoelectrodes: recent advances and new directions.* Annu Rev Anal Chem (Palo Alto Calif), 2012. **5**: p. 253-72.

40. Tian, B. and C.M. Lieber, *Synthetic nanoelectronic probes for biological cells and tissues.* Annu Rev Anal Chem (Palo Alto Calif), 2013. **6**: p. 31-51.

41. Dipalo, M., et al., *Intracellular and Extracellular Recording of Spontaneous Action Potentials in Mammalian Neurons and Cardiac Cells with 3D Plasmonic Nanoelectrodes.* Nano Letters, 2017. **17**(6): p. 3932-3939.

42. Messina, G.C., et al., *Spatially, Temporally, and Quantitatively Controlled Delivery of Broad Range of Molecules into Selected Cells through Plasmonic Nanotubes.* Advanced Materials, 2015. **27**(44): p. 7145-+.

43. Liu, R., et al., *High Density Individually Addressable Nanowire Arrays Record Intracellular Activity from Primary Rodent and Human Stem Cell Derived Neurons.* Nano Letters, 2017. **17**(5): p. 2757-2764.

44. Abbott, J., et al., *CMOS nanoelectrode array for all-electrical intracellular electrophysiological imaging.* Nat Nanotechnol, 2017.

45. Sapsford, K.E., et al., *Functionalizing nanoparticles with biological molecules: developing chemistries that facilitate nanotechnology.* Chem Rev, 2013. **113**(3): p. 1904-2074.

46. Yin, P.T., et al., *Design, synthesis, and characterization of graphene-nanoparticle hybrid materials for bioapplications.* Chem Rev, 2015. **115**(7): p. 2483-531.

47. Wang, J., *Electrochemical glucose biosensors.* Chem Rev, 2008. **108**(2): p. 814-25.

48. Nichols, S.P., et al., *Biocompatible materials for continuous glucose monitoring devices.* Chem Rev, 2013. **113**(4): p. 2528-49.

49. Mai, L., et al., *Nanowire electrodes for electrochemical energy storage devices.* Chem Rev, 2014. **114**(23): p. 11828-62.

50. Gamella, M., A. Koushanpour, and E. Katz, *Biofuel cells – Activation of micro- and macro-electronic devices.* Bioelectrochemistry, 2018. **119**: p. 33-42.

51. Katz, E. and K. MacVittie, *Implanted biofuel cells operating in vivo – methods, applications and perspectives – feature article.* Energy & Environmental Science, 2013. **6**(10): p. 2791.

52. Halamkova, L., et al., *Implanted biofuel cell operating in a living snail.* J Am Chem Soc, 2012. **134**(11): p. 5040-3.

53. Szczupak, A., et al., *Living battery - biofuel cells operating in vivo in clams.* Energy & Environmental Science, 2012. **5**(10): p. 8891-8895.

54. MacVittie, K., et al., *From "cyborg" lobsters to a pacemaker powered by implantable biofuel cells.* Energy & Environmental Science, 2013. **6**(1): p. 81-86.

55. Castorena-Gonzalez, J.A., et al., *Biofuel Cell Operating in Vivo in Rat.* Electroanalysis, 2013. **25**(7): p. 1579-1584.

56. Rasmussen, M., et al., *An implantable biofuel cell for a live insect.* J Am Chem Soc, 2012. **134**(3): p. 1458-60.

57. Shepard, K., T. Ito, and A.J. Griffith, *Extracting energy from the inner ear.* Nature Biotechnology, 2012. **30**: p. 1204.

58. Mercier, P.P., et al., *Energy extraction from the biologic battery in the inner ear.* Nature Biotechnology, 2012. **30**: p. 1240.

59. Hbf878, *Membrane Lipids*. 2017.

60. Singer, S.J. and G.L. Nicolson, *The Fluid Mosaic Model of the Structure of Cell Membranes.* Science, 1972. **175**(4023): p. 720-731.

61. Lingwood, D. and K. Simons, *Lipid Rafts As a Membrane-Organizing Principle.* Science, 2010. **327**(5961): p. 46-50.

62. Ruiz Villarreal, M., *Cell membrane detailed diagram*. 2007, Wikimedia Foundation.

63. Adams, S.V., et al., *The Axon Guide*. 3rd ed, ed. R. Sherman-Gold. 2012, Sunnyvale, California, U.S.A.: MOlecular Devices LLC.

64. Wang, G., et al., *An optogenetics- and imaging-assisted simultaneous multiple patch-clamp recording system for decoding complex neural circuits.* Nature Protocols, 2015. **10**: p. 397.

65. Guo, J.D. and E. Lindner, *Cyclic Voltammograms at Coplanar and Shallow Recessed Microdisk Electrode Arrays: Guidelines for Design and Experiment.* Analytical Chemistry, 2009. **81**(1): p. 130-138.

66. Moretto, L.M. and K. Kalcher, *Environmental Analysis by Electrochemical Sensors and Biosensors*. New York: Springer.

67. Xie, X., et al., *Mechanical model of vertical nanowire cell penetration.* Nano Lett, 2013. **13**(12): p. 6002-8.

68. Hanson, L., et al., *Characterization of the cell-nanopillar interface by transmission electron microscopy.* Nano Lett, 2012. **12**(11): p. 5815-20.

69. Rabieh, N., et al., *On-chip, multisite extracellular and intracellular recordings from primary cultured skeletal myotubes.* Sci Rep, 2016. **6**: p. 36498.

70. Xu, A.M., et al., *Quantification of nanowire penetration into living cells.* Nat Commun, 2014. **5**: p. 3613.

71. VanDersarl, J.J., A.M. Xu, and N.A. Melosh, *Nanostraws for direct fluidic intracellular access.* Nano Lett, 2012. **12**(8): p. 3881-6.

72. Buch-Manson, N., et al., *Mapping cell behavior across a wide range of vertical silicon nanocolumn densities.* Nanoscale, 2017. **9**(17): p. 5517-5527.

73. Hasselgruber, M., *Thermisches Verdampfen, Infografik*. 2008, Wikimedia Foundation.

74. Knauß, S., *Schematischer Aufbau des Magnetonsputterns:*. 2008, Wikimadia Foundation.

75. *Voltammetry Basics*. https://www.ceb.cam.ac.uk/research/groups/rg-eme/teaching-notes/linear-sweep-and-cyclic-voltametry-the-principles].

76. Sauter, A., *Entwicklung eines Elektroden-Arrays zur Nutzung der Membranspannung eukaryotischer Zellen als Grundlage für einen biologischen Stromgenerator*, in *Fakultät Chemie*. 2010, University of Heidelberg: Heidelberg.

77. Schneckenburger, M., *Entwicklung und Charakterisierung eines plasmonischen, nanodrahtbasierten Biosensors mit simultaner elektrochemischer Steuerung*, in *Fakultät Chemie*. 2013, University of Heidelberg: Heidelberg.

78. Seifert, K.P., *Nano-Elektroden-Arrays als Basis zur Nutzung des Membranpotentials eukaryotischer Zellen zur Stromgewinnung*, in *Fakultät Physik und Astronomie*. 2012, Universität Heidelberg: Heidelberg.

79. Weber, S., *Energy Harvesting from Eucaryotic Cells.* Universität Stuttgart, 2013.

80. Hoogvliet, J.C. and W.P. van Bennekom, *Gold thin-film electrodes: an EQCM study of the influence of chromium and titanium adhesion layers on the response.* Electrochimica Acta, 2001. **47**(4): p. 599-611.

81. Siegel, J., et al., *Properties of gold nanostructures sputtered on glass.* Nanoscale Research Letters, 2011. **6**: p. 96.

82. Dumpich, G., S. Friedrichowski, and P. Mikitisin, *Electron transport in percolating gold films.* Thin Solid Films, 1996. **281**: p. 368-371.

83. Siegel, J., et al., *Properties of gold nanostructures sputtered on glass.* Nanoscale Res Lett, 2011. **6**(1): p. 96.

84. Lansaker, P.C., et al., *Spectral Density Analysis of Thin Gold Films: Thickness and Structure Dependence of the Optical Properties*, in *Piers 2013 Stockholm: Progress in Electromagnetics Research Symposium*. 2013, Electromagnetics Acad: Cambridge. p. 443-447.

85. Brett, A.M.O., F.M. Matysik, and M.T. Vieira, *Thin-film gold electrodes produced by magnetron sputtering. Voltammetric characteristics and application in batch injection analysis with amperometric detection.* Electroanalysis, 1997. **9**(3): p. 209-212.

86. Norrman, K., A. Ghanbari-Siahkali, and N.B. Larsen, *6 Studies of spin-coated polymer films.* Annual Reports Section "C" (Physical Chemistry), 2005. **101**: p. 174.

87. Shinwari, M.W., et al., *Microfabricated reference electrodes and their biosensing applications.* Sensors (Basel), 2010. **10**(3): p. 1679-715.

88. Kim, T.Y., S.A. Hong, and S. Yang, *A solid-state thin-film Ag/AgCl reference electrode coated with graphene oxide and its use in a pH sensor.* Sensors (Basel), 2015. **15**(3): p. 6469-82.

89. Thompson, A.C., *X-Ray Data Booklet*, ed. A.C. Thompson. 2009, Berkeley: Lawrence Berkeley National Laboratory, University of California. 176.

6.2 Index of Figures

6.3 Index of Tables

6.4 Abbreviations

c	concentration	mol l^{-1}
CE	Counter Electrode	
CV	Cyclic Voltammetry	
D	Diffusion coefficient	cm s^{-1}
EIS	Electrochemical impedance Spectroscopy	
I	Current	A
MEA	Microelectrode Array	
NEA	Nanoelectrode Array	
NEE	Nanoelectrode Ensemble	
OCP	Open circuit potential	
PVD	Physical Vapor Deposition	
RE	Reference Electrode	
SEM	Scanning Electron Microcope	
SSRE	Solid State reference electrode	
U	Potential	V
WE	Working Electrode	
T	Absolute Temperature	K

7 Acknowledgements

The preparation of this thesis would have never been successful without the aid of many people, to all of whom I want to express my utmost gratitude for their support and patience with me during all stages of this work:

First and foremost I want to express my gratitude towards my supervisor Prof. Joachim P. Spatz, who has always supported me in the pursuit of my ideas, allowing me great freedom in my scientific work and offering advice whenever asked for it. I truly appreciate your patience and calmness throughout my work on this project.

Prof. apl. Rainer Dahint for accepting the duty of being the secondary accessor of this thesis and for his patience regarding the difficulties of setting the date for the final exam.

Priv. Doz. Dr. Günter Majer for accepting the duty of being on the examination board, for his scientific advice and the many interesting discussions on science, the VfB and many other things.

Dr. Amin Rustom, the initiator of this project, for initially inviting me to join the project and the department of Prof. Spatz.

M. Sc. Oskar Stauffer, my co-worker in this project for the many interesting discussions and the collaborative efforts on behalf of this project.

Dr. Diego Pallarola for his advice regarding the construction of the reference electrodes and in many aspects of the electrochemical experiments.

Sigrid Riese, for her assistance in cell culture and for providing excellent working conditions in the Heidelberg laboratories of this department until her retirement.

All the staff from the technical facilities, at the Institute of Physical Chemistry in Heidelberg and at the Max-Planck-Institutes in Stuttgart; especially the mechanical workshops. Without the countless custom-built parts, my work would not have been possible.

Very special thanks to all my office-mates, both in Heidelberg and Stuttgart (in order of appearance, hopefully): Dr. Dimitris Missirlis, M. Sc. Maria Halbig, Dr. Rebecca Medda, Dr. Tina

Wiegand, Dr. Jennifer Young, Dr. Andrew Holle, Dr. Christoph Stanglmaier and M.Sc. Florian Hunke. I assume was a bit or a burden at times, given my occasional moodiness. Your assistance, both scientific and social, supporting me in most difficult times is an invaluable contribution to the becoming of this work. I hope the memory of the fun times (there were a few, at least) will predominate.

They above said is equally valid for all the other co-workers in our group, who shared labs and seminars with me (again in no special order): M.Sc. Christoph Frey, M.Sc. Barbara Haller, Dr. Jan-Willi Janiesch, Dr. Marian Weiss, Dr. Sarah Jahn, M.Sc Dirk Olech, M.Sc. Chiara Lambada, M.Sc. Julia Riecken, Dr. Sabrina Rossberger, Dr. Jacopo DiRusso, Dr. Ilia Platzman, Dr. Elisabeth Schwab, Dr. Volker Martin, Dr. Franziska Dietrich and Dr. Kerstin Göpferich. I'm sure I missed out on some persons here, I beg your pardon if you feel omitted.

Occasionally, I had the opportunity of spending some time with people not on the payroll of the Max-Planck-Institute, which I cannot all name in person on this occasion. My dearest friends, you are irreplaceable to me. Thank you all for your support and patience during the last month and years. I'll try to make up as good as I can for the many missed occasions over the past couple of month. This goes especially towards Lise, Kathrin & Axel.

Pia, Katha und Bernhard, you are the greatest friends one could possibly have!

It goes without saying, that I must acknowledge my first and foremost supporters, my parents. Only your generous support of my academic studies and your patience during these times made it possible for me to reach this point. Thank you very much!

And, of course,

Marion

You carried by far the biggest burden during the preparation of this thesis. Your support wasand will be invaluable to me, without your patience this work would likely remain unfinished!

Thank you so very much!

Again, to everyone who shared at least parts of this journey with me:

Danke! Danke! Danke!

8 Statutory Declaration

Eidesstattliche Versicherung gemäß § 8 der Promotionsordnung der Naturwissenschaftlich-Mathematischen Gesamtfakultät der Universität Heidelberg:

1. Bei der eingereichten Dissertation zu dem Thema “ Manufacturing of gold nanoelectrode-ensembles for intracellular recording of living cells ” handelt es sich um meine eigenständig erbrachte Leistung.

2. Ich habe nur die angegebenen Quellen und Hilfsmittel benutzt und mich keiner unzulässigen Hilfe Dritter bedient. Insbesondere habe ich wörtlich oder sinngemäß aus anderen Werken übernommene Inhalte als solche kenntlich gemacht.

3. Die Arbeit oder Teile davon habe ich bislang nicht an einer Hochschule des In- oder Auslands als Bestandteil einer Prüfungs- oder Qualifikationsleistung vorgelegt.

4. Die Richtigkeit der vorstehenden Erklärungen bestätige ich.

5. Die Bedeutung der eidesstattlichen Versicherung und die strafrechtlichen Folgen einer unrichtigen der unvollständigen eidesstattlichen Versicherung sind mir bekannt.

Ich versichere an Eides statt, dass ich nach bestem Wissen die reine Wahrheit erklärt und nichts verschwiegen habe.

Heidelberg, den 13. Juni, 2018

Sebastian Weber